Observation of Metal Nucleation on Free-Standing Graphene by Means of Low-Energy Electron Holography

Dissertation

zur

Erlangung der naturwissenschaftlichen Doktorwürde

(Dr. sc. nat.)

vorgelegt der

Mathematisch-naturwissenschaftlichen Fakultät

der

Universität Zürich

von

Marianna Lorenzo

aus

Italien

Promotionskommission

Prof. Dr. Hans-Werner Fink (Vorsitz und Leitung der Dissertation)
Prof. Dr. Jürg Osterwalder
Prof. Dr. Peter Hommelhoff
Dr. Roger Morin
Dr. Conrad Escher
PD Dr. Tatiana Latychevskaia

Zürich, 2018

Abstract

Functionalizing graphene, the atomically thin carbon layer, has attracted considerable interest in view of possible technological applications in using graphene in electronic devices. The requirement of tuning the electronic properties of graphene in an efficient and controllable way has driven studies on graphene functionalization by metal deposition. Although the macroscopic effects of metal adsorption or intercalation in supported graphene can easily be accessed, the study of metal deposition on suspended graphene on an atomic scale, in real time and under well-defined deposition conditions remained a challenging task so far.

The low-energy electron point source (LEEPS) microscopy is an investigation technique based on Gabor's holography principle and represents a lens-less transmission setup whereby the divergent coherent electron beam is emitted by an ultra-sharp tungsten tip. The electron reference wave interferes with the object wave, elastically scattered off the sample, producing a hologram on a distant electron detector. The LEEPS microscope realized at the UZH operates with coherent electrons in the 50-250 eV energy range, corresponding to de Broglie wavelengths in the range of 0.17-0.08 nm. Graphene is highly transparent to low-energy electrons and has been successfully used as a substrate in several LEEPS investigations. Owing to the high sensitivity of low-energy electrons to electric and magnetic fields, the detection of even a fractional elementary charge has become possible. As alkali metals adsorbed on free-standing graphene are expected to transfer their outermost electron, which in turn gets delocalized in graphene, a positive ion remains, and single alkali atoms can thus be detected when adsorbed on free-standing graphene.

The work presented in this thesis represents the first in-situ experimental investigation of the deposition of alkali and transition metals on free-standing single and bilayer graphene by means of the LEEPS microscope. In particular, the investigation has focused on the adsorption and nucleation processes of Li, K and Cs alkali metals and of Pd as

one representative for a transition metal. LEEPS images of metal deposition on graphene under ultra-high vacuum conditions have been acquired in real time, respectively with 25 frames/second. A comparison between the acquired images for different alkali metals shows a very similar signature; namely a bright spot due to the positive charge for Cs and K and a much smaller one for Li. A further similarity between Cs and K has been observed once the deposition has been terminated; these two metals do not remain localised on the graphene, on the contrary to Li that forms localised charged entities. The analysis of alkali metal deposition on adjacent domains of single and bilayer graphene showed that they readily intercalate in between the bilayer domain. This finding allows to quantitatively analyse the particle density in the two graphene domains during the deposition and eventually also under equilibrium conditions. In particular, the particle density in the single layer domain has been found to be much lower than in the bilayer domain. Once an equilibrium distribution has been established, a quantitative estimate of the difference in the free energy of binding between the single and bilayer domains has been obtained for K. A control experiment performed with depositing Pd shows the formation of a similar distribution of clusters on both domains and no intercalation. The effect of the electron beam illumination on the Pd cluster growth has also been investigated. The graphene window imaged continuously during the deposition shows the formation of large islands; while the adjacent windows imaged only before and after the end of the deposition exhibit a high density of smaller clusters instead. Although the LEEPS technique does not provide any information on cluster thickness, from a comparison with TEM images it was inferred that such islands are thinner than 50 nm.

Zusammenfassung

Die Funktionalisierung von Graphen stößt aufgrund der möglichen technologischen Anwendungen zunehmend auf Interesse. So haben Die Forderungen nach effizientem, kontrolliertem Regulieren der elektronischen Eigenschaften von Graphen diverse Studien über Graphenfunktionalisierung motiviert. Dabei spielt das Verständnis betreffend die Einlagerungprozesse einzelner Metallatome ins Graphen eine zentrale Rolle. Wenngleich die makroskopischen Effekte von Adsorption und Interkalation von Metallatomen in Graphen auf einem Substrat leicht zugänglich sind, stellt die direkte Beobachtung des Depositionsprozesses auf freistehendem Graphen auf atomarer Skala und unter wohldefinierten Bedingungen hohe Anforderungen.

LEEPS Mikroskopie ist eine Untersuchungstechnik, die auf dem Gaborschen Prinzip der Holographie beruht. Es handelt sich um ein elektronenoptischen Aufbau ohne Linsen, bei dem ein divergenter, kohärenter Elektronenstrahl von einer ultra-scharfen Wolfram-Spitze emittiert wird. An der Probe wird ein Teil des Strahls elastisch gestreut und dem ungestreuten Anteil überlagert. Diese Überlagerung repräsentiert das Hologram der Probe und wird auf einem Detektor festgehalten. Das LEEPS Mikroskop der UZH arbeitet mit kohärenten Elektronen im Energiebereich von 50 bis 250 eV; das entspricht einer de Broglie Wellenlänge von 0.17 bis 0.08 nm. Graphen ist für niederenergetische Elektronen durchlässig, und ist bereits in mehreren LEEPS Untersuchungen als Substrat erfolgreich eingesetzt worden. Die hohe Empfindlichkeit von niederenergetischen Elektronen gegen elektrische und magnetische Felder ermöglicht sogar den Nachweis von Bruchteilen der Elementarladung. Das äußerte Elektron von Alkalimetallen, die auf freitragendem Graphen adsorbiert sind, wird transferiert und delokalisiert. Dadurch entsteht ein positives Ion, und einzelne Alkaliatome können nachgewiesen werden.

Die vorliegende Arbeit stellt die erste experimentelle in-situ Untersuchung zur Adsorption und Interkalation von Alkali- und Übergangsmetalle auf freitragendem ein- und dop-

pelschichtigem Graphen dar. Die Untersuchung fokussierte sich vor allem auf Adsorptions- und Nukleationsprozesse der Alkalimetalle Li, K und Cs und des Übergangsmetalls Pd. LEEPS Bilder von Metalldeposition auf Graphen unter UHV Bedingungen wurden in Echtzeit, genauer mit 25 Bildern/s, aufgenommen. Der Vergleich zwischen den aufgenommenen Bildern zeigte einen sehr ähnlichen hellen Spot für Cs und K, und einen viel kleineren Spot für Li. Nach dem Aufbringen wurde eine weitere Ähnlichkeit zwischen Cs und K festgestellt; die beiden Metalle bleiben nämlich nicht lokalisiert auf Graphen, während Li lokalisierte geladene Einheiten bildet. Der Vergleich des Depositionsprozesses von Alkalimetallen auf aneinander grenzenden Domänen von ein- und doppelschichtigem Graphen zeigte, dass in den doppellagigen Domänen Interkalation zwischen die beiden Graphenlagen stattfindet. Dieses Ergebnis wurde durch die Teilchendichteanalyse in den zwei Graphendomänen während des Aufbringens und im Gleichgewichtszustand gestützt. Insbesondere zeigte die einschichtige Domäne eine deutlich niedrigere Teilchendichte als die doppelschichtige Domäne. Aus den Daten im Gleichgewichtszustand wurde eine quantitative Abschätzung der Differenz zwischen den Bindungsenergien für K auf ein- und doppelschichtigen Domänen erhalten. In einem Kontrollexperiment mit Pd konnte die Entstehung der gleichen Clusterverteilungen in beiden Domänen, jedoch keine Interkalation nachgewiesen werden. Die Wirkung der Elektronenstrahlung auf Pd Clusters wurde untersucht. Das Graphenfenster, welches während des Deponierens kontinuierlich abgebildet wurde, zeigt grosse Inseln; die benachbarten Fenster, die nur vor und nach der Deposition abgebildet wurden, zeigten eine höhere Dichte von kleineren Inseln. Obwohl die gewonnenen Daten keine Information über die Clusterdicke enthalten, konnte aus dem Vergleich mit TEM-Bildern entnommen werden, dass diese Inseln dünner als 50 nm sind.

Abbreviations

AFM	Atomic force microscope
AMD	Alkali metal dispenser
APS	Ammonium persulfate
ARPES	Angle-resolved photoelectron spectroscopy
BLG	Bilayer graphene
CVD	Chemical vapour deposition
DFT	Density functional theory
DOS	Density of states
EPS	Electron point-source
ESCA	Electron spectroscopy for chemical analysis
FLG	Few-layer graphene
GGA	Generalised gradient approximation
GIC	Graphite intercalation compound
HOPG	Highly-oriented pyrolytic graphite
HRTEM	High-resolution transmission electron microscope
LDA	Local-density approximation
LDOS	Local density of states
LEED	Low-energy electron diffraction
LEEM	Low-energy electron microscope
LEEPS	Low-energy electron point source
MCP	Micro-channel plate
PEEM	Photoemission electron microscope
PES	Photoemission electron spectroscopy
PMMA	Poly(methyl methacrylate)
SEM	Scanning electron microscope
SLG	Single layer graphene
STM	Scanning tunnelling microscope
TEM	Transmission electron microscope
UHV	Ultra-high vacuum
UPS	Ultraviolet photoelectron spectroscopy
XPS	X-ray photoelectron spectroscopy
ZLG	Zero-layer graphene

Contents

1 Introduction **1**

1.1 A brief introduction to graphene 1

1.1.1 Graphene functionalisation 3

1.1.2 Graphene characterization 5

1.2 Aim of the thesis 8

1.3 Outline of the thesis 9

2 Metal deposition on graphene: results from the literature **11**

2.1 Alkali Metal adsorption 12

2.1.1 Adsorption on free-standing graphene: theoretical predictions 12

2.1.2 Adsorption on SiC-supported graphene 16

2.1.3 Adsorption on metal-supported graphene 18

2.1.4 Adsorption on graphite 20

2.2 Alkali Metal intercalation 22

2.2.1 Intercalation in graphite 22

2.2.2 Intercalation in metal-supported graphene 24

2.2.3 Intercalation in SiC-supported graphene 27

2.2.4 Intercalation in bilayer graphene 29

2.3 Transition Metal adsorption 33

2.3.1 Transition metals on graphene 34

2.3.2 Transition metals on few-layer graphene 40

2.3.3 Transition metals on graphite 41

2.4 Transition Metal intercalation 46

3 The LEEPS microscopy technique **51**

3.1 In-line holography with low-energy electrons 51

3.1.1 The holographic principle . . . 52
3.1.2 Holography with low-energy electrons . . . 53
3.1.3 Graphene as support slide . . . 56
3.1.4 Direct observation of charges . . . 59
3.2 The LEEPS microscope . . . 60
3.2.1 Design of the microscope . . . 60
3.2.2 The evaporator unit . . . 62
3.2.3 Sample preparation . . . 66
3.2.4 Distortion corrections . . . 69

4 Metal adsorption and nucleation on free-standing graphene 73
4.1 Adsorption of alkali metal atoms on free-standing single layer graphene . . 74
4.2 Alkali metal atoms on adjacent domains of free-standing single layer and bilayer graphene . . . 78
4.2.1 Potassium and Lithium deposition . . . 79
4.2.2 Cesium deposition . . . 87
4.2.3 Palladium deposition . . . 88
4.3 Palladium deposition on free-standing single layer graphene . . . 89
4.3.1 The electron beam effect . . . 90
4.3.2 Palladium clusters: LEEPS vs TEM . . . 94
4.4 Cesium nucleation on Palladium clusters . . . 95

5 Conclusions and Outlook 101

A Simulations of the probing electron trajectories deflected by an ion on graphene 105
A.1 Adsorbed ion . . . 106
A.2 Intercalated ion . . . 106

B Li cluster dynamics in the bilayer graphene domain 111

Bibliography 113

Chapter 1

Introduction

1.1 A brief introduction to graphene

In 2004, Novoselov and Geim reported the isolation of a single-layer of graphene on a silicon oxide substrate by micro-mechanical cleavage of graphite (known as "Scotch tape method") [1]. This milestone discovery has brought this allotrope of carbon to the attention of the scientific community, with the aim to characterise and understand its fascinating properties.

Prior failures to isolate a two-dimensional layer were ascribed to the theoretical results of Peierls [2], Landau [3] and Mermin [4, 5], predicting the instability of a truly two-dimensional crystal except at zero temperature[1]. However, in the case of graphene the presence of atomic-scale buckling [6] and intrinsic ripples [7, 8] accommodates the excess surface energy, making graphene a very stable material.

The formation of a Pt(100) supported graphene layer was hypothesised already in the late '60s to explain some low-energy electron diffraction (LEED) patterns of carbon overlayer formed by exposure and dissociation of hydrocarbons [9, 10]. These results represented the starting point for the development of the well-known chemical vapour deposition (CVD) protocol, nowadays widely used for the production of large graphene layers on transition metal substrates [11–17].

The outstanding electronic properties of graphene are due to its peculiar band struc-

[1] The work of Peierls [2] and Landau [3] predicted the instability of a 2D infinite film at finite temperature due to thermal fluctuations. For infinite 2D crystals characterised by short-range interactions in the ground state, the Mermin and Wagner theorem [4, 5] states that long-wavelength density fluctuations lead to atom displacements growing with distance, causing the breakdown of the crystal long-range order. In both cases, these findings are not contradicted by the existence of graphene. These results do not preclude the existence of an almost perfect 2D lattice, and thus of a 2D crystal with ripples.

ture. In a graphene layer, carbon atoms are arranged in a hexagonal lattice with two atoms per unit cell (Figure 1.1a). Carbon atoms form in-plane σ-bonds via sp^2 hybridization with the three neighbouring carbon atoms; the out-of-plane p_z orbitals contribute to the formation of delocalized π and π^* states, forming the highest occupied valence band below the Fermi energy level E_F and the lowest unoccupied conduction band above E_F. The electronic band structure of graphene, calculated in the tight-binding approximation, results in a linear dispersion relation at low energies:

$$E_{\pm} = \pm\hbar\nu_F|k|\,, \tag{1.1}$$

where $\hbar$ is the reduced Planck constant, ν_F the Fermi velocity, and k the wave vector. The positive solution refers to the conduction band (upper band in Figure 1.1c), while the negative solution corresponds to the valence band (lower band in Figure 1.1c). The π and π^* orbitals are degenerate at the K (and K') point of the Brillouin zone, making graphene a zero band-gap semiconductor. These contact points are known as "Dirac points"[2] and coincide with the Fermi level; the conical electron and hole bands are called "Dirac cones". This nomenclature comes from the equivalence of the dispersion relation (equation 1.1) to the massless Dirac equation. According to that, charge carriers in graphene can be thought as massless Dirac fermions with extraordinarily high velocity. Graphene, indeed, has shown to be the material with the highest carrier mobility, that has been experimentally found to be of $\sim 2 \times 10^5\,\mathrm{cm^2\,V^{-1}\,s^{-1}}$ at room temperature [18–21]. This band structure is responsible for the exceptional electronic properties of graphene [22] such as the room temperature quantum Hall effect [1, 23].

The peculiar properties of graphene make this material a promising candidate for a wide range of applications. Since its discovery, graphene has been considered as a possible substitute of silicon to improve the performances of microelectronic devices [1, 19, 24]. It finds applications also in the field of hydrogen storage [25] and chemical sensors [26] thanks to its large surface area. Moreover, graphene exhibits an exceptional mechanical strength [27] and a high thermal and electrical conductivity [22,28], features that allow for the use of graphene as transparent substrate for transmission scheme microscopy investigations [29–33].

[2] They are also called "neutrality points".

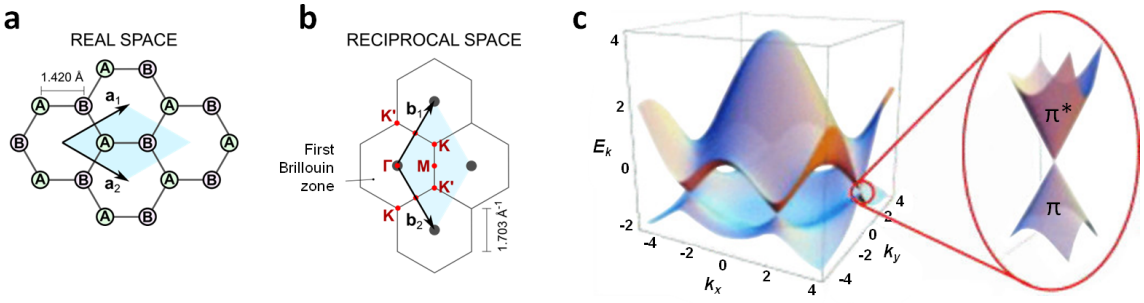

Figure 1.1: Graphene lattice and band structure. (a) Real space lattice. The labels A and B indicate the two triangular sublattices. $\mathbf{a}_1$ and $\mathbf{a}_2$ are the primitive vectors and subtend the primitive unit cell depicted in light blue colour. (b) Reciprocal space lattice. The corner of each Brillouin zone (gray hexagons) coincides with a Dirac point. $\mathbf{b}_1$ and $\mathbf{b}_2$ are the reciprocal lattice vectors. (c) Three dimensional band structure of graphene showing the zero-gap at the K and K' points in the reciprocal space. The zoom at one of the K points shows the Dirac cone structure. Adapted from Ref. [22].

1.1.1 Graphene functionalisation

Despite its outstanding properties, graphene needs to be functionalised in a controllable way for its practical use in electronic devices. It has been demonstrated that it is possible to tailor the graphene electronic properties by adsorbing atoms or molecules on its surface. The nature of the adsorbed specimen will determine the strength of the chemical bond and the charge transferred to the graphene layer, that in turn will determine the final electronic properties of the functionalised graphene [34]. Thus, depending on the adsorbed specimen, it is possible to tune a specific property. For example, it can be possible to open a band-gap [35–37], create localized magnetic moments [38,39], or increase the spin-orbit coupling strength, which can induce superconductivity [40–43].

Graphene can be doped with electrons by deposition of electron donor adsorbates; the Fermi level shifts upward the Dirac point indicating an n-type doping. The hole doping can be achieved by deposition of electron acceptor adsorbates; the outcome is p-doped graphene. The effect of the doping on the band structure of graphene at the K and K' points is depicted in Figure 1.2a. The Fermi level shift with respect to the Dirac point, $\Delta E_{\mathrm{F}} = E_{\mathrm{D}} - E_{\mathrm{F}}$, defines the amount of charge eN transferred between the adsorbed metal and the graphene [44]. In fact, in the low energy range, the density of states (DOS) can be described by a linear function: $D(E) = D_0|E|$, where $D_0 =$

$0.09\,\mathrm{eV}^{-2}\,(\mathrm{unit\,cell})^{-1}$; the value of N can be obtained integrating $D(E)$ between the Dirac point and the Fermi level, and the resulting equation depends only on the Fermi level shift: $N = \mathrm{sign}(\Delta E_\mathrm{F}) D_0 \Delta E_\mathrm{F}^2/2$. According to this equation, N is negative for n-doped graphene and positive for p-doped graphene.

The adsorption of alkali metals and of alkaline earth metals can result in efficient doping. At sub-monolayer coverage such metals transfer almost all their outermost electron to graphene, tuning the carrier concentration to give rise to n-type doping (see for example Ref. [34] and Ref. [45]). This class of metals has been predicted to enhance noticeably the electron-phonon coupling leading to a critical temperature for superconductivity of several Kelvin degrees [41,43]. While alkali metals are characterised by a quasi-ionic bonding with graphene, transition metals tend to form a strong covalent bond. The resulting strong electron-electron interaction can be used for spintronic applications [38, 46].

A further and pronounced influence on graphene properties arises from the interaction with a supporting substrate. The charge transfer and the breaking of the A and B sublattice symmetry cause a shift of the Dirac point and the opening of a band gap depending on the strength of the bond. As an example, a SiC substrate is widely used for its extremely weak bond with graphene; the doping is through electron transfers to the π^* band of graphene, causing a shift of the Dirac point to 0.4 eV below the Fermi level [47, 48] and a band gap of 0.26 eV [48]. In this case, as well as for metal substrates weakly interacting with graphene, the conical shape of the π and π^* bands is maintained. The situation is different for metal substrates strongly interacting with graphene: the strong hybridization of the graphene and metal orbitals causes a distortion of the Dirac cone, along with the downshift of the π band with respect to E_F and the band gap opening [49, 50]. Thus, the interaction with the substrate shows to be a limiting factor for potential graphene applications. An efficient way to decouple the substrate from the graphene is by intercalation of atoms in between them. However, the intercalants contribute to the functionalisation of graphene, although preserving most of its properties.

Compared to the single-layer graphene, the band structure of the bilayer graphene exhibits a quadratic spectrum and contains two additional π and π^* states (Figure 1.2b) since the unit cell contains four atoms. Any perturbation of the lattice symmetry, as like the presence of adsorbates or a supporting substrate, causes a band gap opening at the Dirac point [51]. Like single-layer graphene, bilayer graphene can be functionalised in order to control the carrier density, the occupation of electronic states near the Fermi

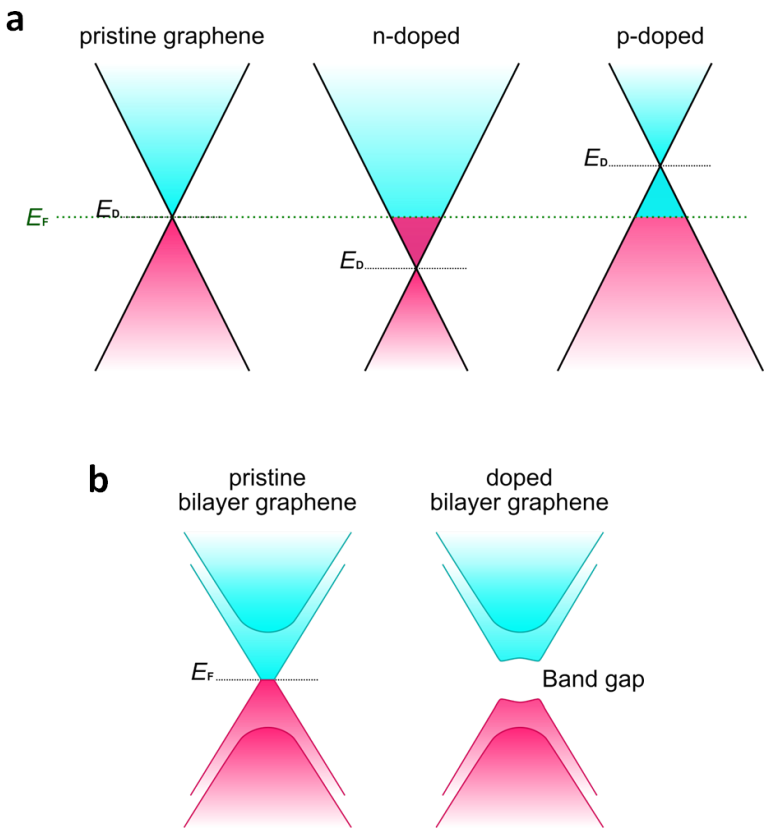

Figure 1.2: Sketch of the electronic band structure of pristine and doped graphene around the K and K' points. The cyan colour depicts the occupied states, while the magenta colour indicates the unoccupied states. (a) Electronic band structure of pristine, n-doped, and p-doped single layer graphene. The Fermi level is indicated by the green dotted line. In this scheme, the zero band-gap is preserved. (b) Electronic band structure of pristine and doped bilayer graphene.

level, and to enhance or reduce the band gap [52].

1.1.2 Graphene characterization

In this section, the most common experimental surface sensitive techniques for graphene investigations will be briefly introduced. It should be noted that there are not many techniques allowing for graphene characterization.

Spectroscopy techniques are employed to detect and quantify graphene doping. Among the spectroscopic techniques, Raman spectroscopy is a standard method to examine graphene quality. This technique investigates the inelastically scattered photons from a laser beam incident on the sample. When the incident radiation excites an electron from the ground

level, an unstable virtual state is created; it decays in a vibrational level re-irradiating as a scattered photon less energetic than the incident radiation (Stokes Raman scattering). By contrast, when an electron is excited from the vibrational level and decays in the ground level, the scattered photon is more energetic then the incident radiation (anti-Stokes Raman scattering). The shift in energy of the scattered photon with respect to the laser photons provides information on the vibrational modes of the sample. The analysis of the typical Raman peaks of graphene can provide information on graphene quality and doping[3] [53,54]. The spatial resolution of a Raman spectrometer can be in the sub-micron range.

Photoemission electron spectroscopy techniques, PES for short, are based on the photoelectric effect. Depending on the frequency of the radiation source, it is possible to investigate the core-level states or the valence band of a solid. In the first case, X-rays are used, and the technique is called X-ray Photoelectron Spectroscopy (XPS) or Electron Spectroscopy for Chemical Analysis (ESCA). In the second case, ultraviolet radiation is used in the Ultraviolet Photoelectron Spectroscopy (UPS), while soft X-rays are typically employed in the Angle-Resolved Photoelectron Spectroscopy (ARPES). ARPES allows to investigate the band structure as a function of energy and momentum, and it is widely used to study the Dirac cone of graphene systems [55]. All these techniques require to operate in the ultra-high vacuum (UHV) regime.

The photoelectric effect is also the working principle of the Photoemission Electron Microscope (PEEM). In this microscopy technique, the photoelectrons emitted from the sample are accelerated towards a system of magnifying electron lenses. The local different work functions give rise to different electron emission that results in the image contrast recorded at a 2D detector. The spread in the energies of the emitted electrons, ranging from the energy of the ionizing radiation to the work function of the sample, is the primary source of aberrations in this kind of microscopy. As for PES spectroscopies, UHV conditions are required.

The graphene surface, as well as the distribution of adsorbates and of defects on it, can be characterized by means of microscopy techniques. In the Low-Energy Electron Microscope (LEEM), the image is formed from the back-scattered electrons created by probing

[3]The information provided by a Raman spectrum of graphene are typically the presence of defects (existence of the peak at $1350\,\mathrm{cm}^{-1}$, called D mode), the occurrence of strains, impurities or charges on the graphene surface (peak at $1583\,\mathrm{cm}^{-1}$, called G mode), and the number of graphene layers (peak at $2700\,\mathrm{cm}^{-1}$, called 2D mode) [53].

electrons decelerated to energies below 100 eV. Low-energy electrons are characterised by a short inelastic mean free path, making them very sensitive to the surface of the sample. The reflected electron intensity as a function of the probing electron energy, called IV-curve, provides spectroscopic information: in fact, it shows a minimum at energies for which the probing electron energy coincides with the energy of an unoccupied state in the sample. LEEM allows for imaging dynamical processes on a surface with nm resolution.

A low-energy electron beam (20-200 eV) is used also in Low-Energy Electron Diffraction (LEED), a method widely used to study the surface structure of crystals. The elastically backscattered fraction of a collimated electron beam forms a diffraction pattern on the detector. In LEED acquisitions, a large area of the sample is illuminated by the electron beam; this technique probes the long-range periodicity of the sample, but does not allow for detecting local defects.

Transmission Electron Microscope (TEM) and Scanning Electron Microscope (SEM) employ an electron beam with higher energies with respect to LEEM to image the sample. A typical TEM microscope is equipped with a 60-300 keV electron beam; nevertheless, for graphene investigations a beam with an energy at or below 80 keV is used to minimize knock-on damages [56]. The electrons transmitted across the sample allow for imaging free-standing graphene, even at atomic resolution in the case of the High-Resolution TEM (HRTEM) [57]. Due to its high transparency to electrons in the keV range, suspended graphene finds applications as substrate for TEM studies (see e.g. Ref. [58]). In the SEM microscope, the sample is scanned by a focused electron beam operating typically at energies in the range 0.5-40 keV, achieving a resolution in the nm range scale. The image of a graphene sample is usually obtained detecting the secondary electrons, being emitted very close to the surface. In both TEM and SEM, the sample is subjected to electron beam induced contaminations.

The Scanning Tunnelling Microscope (STM) and Atomic Force Microscopy (AFM) are imaging techniques based on the interaction of a sharp tip with the surface of the sample. In STM, the tip scans the surface at a distance such that electron tunnelling can occurs between the sample and the tip, to which a bias voltage is applied. During the scan, a constant tunnelling current flow is ensured while adjusting the tip-sample distance. The STM image, given by the plot of the height as a function of position, provides an atomic resolution topographic map of the sample. The tunnelling current depends also on the the local density of states (LDOS) of the sample, which can be probed operating the STM in

a Scanning Tunnelling Spectroscopy mode: the tunnelling current is measured versus the bias potential between the tip and the sample keeping a fixed height [59]. The tunnelling conductance dI/dV relates to the LDOS at the tip position.

Differently from STM, AFM can also investigate the surface topography of insulators and measure the physical height of features on the surface. The variations of the force between the atoms of the surface and the apical atoms of the scanning tip is measured through the deflection of a cantilever attached to the tip, giving rise to a 3D mapping of the surface. The typical height resolution is of the order of 0.03 nm and forces in the pN regime can be resolved.

Combining microscopy techniques with spectroscopic techniques, a complete characterization of doping adsorbates on graphene can be achieved. Nevertheless, the direct visualization of individual adsorbates and their charge transferred to graphene is still a challenging measure.

1.2 Aim of the thesis

The aim of the present thesis work is to perform a direct visualization of the adsorption and the nucleation of metals on free-standing graphene. To achieve this goal, a dedicated low-energy electron point source (LEEPS) microscope has been employed, a lens-less transmission setup designed for in-line electron holography [60]. The microscope operates under UHV conditions and allows for in situ deposition during the acquisition of the images. The low energy of the probing electrons, typically in the range of 30-250 eV, allows to image charged impurities with a sensitivity of a fraction of an elementary charge [61]. Thus, the LEEPS microscope is ideally suited to investigate the alkali metal deposition on free-standing graphene. In fact, alkali metal atoms get positively charged upon adsorption on free-standing graphene, associated with a charge transfer close $1e$ [34]. LEEPS investigations allow for the direct imaging of a single alkali metal adsorption event, giving information on the position and on the charge transfer of individual adsorbates at the same time.

The transparency of graphene to electrons in the range of energies of the LEEPS electron beam amounts to $\sim$70% per layer, allowing consequently to image bilayer graphene [62,63]. The second goal of this thesis work is the observation of alkali metals intercalated in between the free-standing bilayer graphene. It is well known that alkali metals readily

intercalate in graphite through the step edges of its carbon layers [64]. It is therefore conceivable to also expect intercalation in free-standing graphene samples exhibiting a step edge between the single-layer and the bilayer domain.

Together with these primary motivations, the deposition of Pd has been studied for a comparison between the adsorption and nucleation properties of alkali metals and transition metals on free-standing single-layer and bilayer graphene.

Free-standing graphene provides true two-dimensional graphene, without effects induced by a substrate, and thus the study of metal deposition on it could provide further insight on the metal-graphene interaction.

1.3 Outline of the thesis

This thesis is organised as follows:

Chapter 2 is dedicated to the state of the art of metal adsorption on graphene. First, experimental as well as theoretical predictions on alkali metal adsorption on graphene will be presented. The second part will review the literature results on the adsorption and nucleation of transition metals on graphene.

In chapter 3 the focus will be on the low-energy electron point source holography, which has been used to investigate metal adsorption and nucleation on free-standing graphene. A brief introduction to in-line holography and the last achievement obtained with this technique are presented in the first part of the chapter, followed by the description of the LEEPS microscope built at the University of Zurich and used for the investigations reported in chapter 4.

In chapter 4 the experimental results on metal adsorption on graphene will be presented and discussed. The chapter starts with alkali metal deposition on free-standing single-layer graphene, followed by their deposition onto bilayer graphene, where intercalation in between the graphene layers has been observed. The deposition of Pd, as representative of transition metals, has been investigated on single-layer and bilayer graphene. Moreover, the effect of the electron beam illumination on Pd nucleation has been studied. To conclude, the nucleation of Cs on pre-existing Pd clusters will be reported.

Finally, chapter 5 will summarise the conclusions and provide an outlook for possible future investigations.

Chapter 2

Metal deposition on graphene: results from the literature

Graphene functionalisation has been widely studied as a necessary step to tune the graphene electronic properties, such as changing the carrier concentration or opening a band gap at the Dirac point. Adsorption of metal atoms on graphene is one of the possible functionalisation methods. The resulting electronic properties are strongly related to the nature of the bond between the adsorbate and the carbon atoms [46]. Alkali metals adsorb on graphene forming an ionic bond, thus acting as electron donors; the increase in the number of charge carriers can contribute to the superconductivity of alkali metal coated graphene [40]. Transition metals, on the contrary, adsorb forming a covalent bond, and can be used as a tool to tune the magnetic properties of transition metal coated graphene [46]. In addition, different metals exhibit different growth morphologies [65].

Metal deposition can give rise not only to metal adsorbates on the surface, but also to intercalated structures in graphite and supported graphene. Graphite intercalation compounds (GICs) have been investigated since the 1970's as a way of tuning the graphite electronic transport and optical properties [64]. Intercalation in supported graphene, instead, has been widely studied mainly as a way to decouple the graphene layer from its substrate [66, 67].

In this chapter, the state of the art concerning metal deposition on graphene and graphite is reviewed. The focus is on alkali and transition metal adsorption, nucleation and intercalation properties, highlighting results for Cs, K, Li and Pd deposited by physical vapour deposition on graphene or graphite at room temperature and under UHV

conditions. These are, in fact, the same conditions of the experiments performed for this thesis work, and they may allow for a direct comparison with the results presented in chapter 4.

2.1 Alkali Metal adsorption

The following section reports on the literature concerning alkali metal adsorbate arrangements and the charge transferred to graphene, as well as on the energetics related to adsorption and diffusion. Experimental results are reported for supported graphene. Concerning free-standing graphene, to the best of my knowledge, only theoretical predictions can be found in the literature.

Doping graphene with alkali metals allows to modify the carrier density in graphene without affecting the Dirac cone shape. Both experiments [68–76] and theoretical studies [45,77–81] have shown that alkali metals adsorbed on graphene easily donate their valence electrons; such electrons become delocalised over the graphene sheet, giving rise to a polar bond and an n-doping of graphene. Below, theoretical predictions on free-standing graphene, and experimental results on alkali metals on supported graphene, are reported.

2.1.1 Adsorption on free-standing graphene: theoretical predictions

Adsorption of metals on graphene is the topic of several studies, based on density functional theory (DFT) calculations. These simulations are absolute zero temperature models, with results strongly dependent on the choice of the model and the method, as pointed out by Dimakis *et al.* [81]. As an example, the DFT calculations performed by Lugo-Solis and Vasiliev [77] on K adsorbed on graphene show values depending on the exchange-correlation functional employed: the binding energies calculated by generalised gradient approximation (GGA) functional are ∼20% lower than those obtained by local-density approximation (LDA), reflecting the tendency of the LDA functional to overestimate the binding energies; the equilibrium distances calculated by GGA, instead, are larger than their corresponding LDA values since LDA underestimate the interatomic bond lengths. Nevertheless, these studies can provide trends for predicting the properties of alkali metal atoms adsorbed on graphene, as a function of the chemical specificity and the coverage.

For a single alkali metal on graphene, the hollow site (H) has been found to be the more favourable adsorption site, followed by the carbon bridge (B) and the top of a carbon

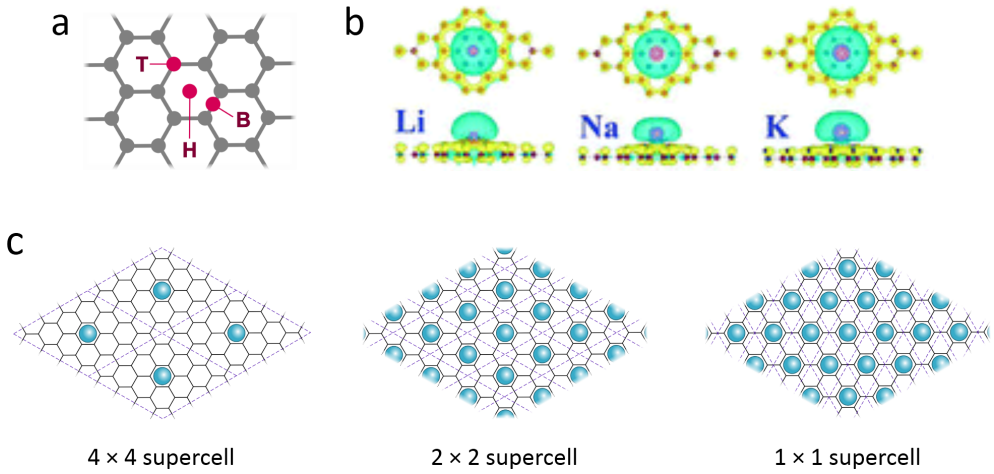

Figure 2.1: Adsorption on free-standing graphene. (a) An adatom on graphene can adsorb on the hollow site (H) in the center of the carbon hexagon, on the top of a carbon atom (T), or on the bridge site (B) between two bonded carbon atoms. (b) Bonding electron distributions (BED) induced by Li, Na, and K adsorption on graphene. The orange color (+0.004 e/Å^3) indicates an electron density increase, while the cyan color (-0.004 e/Å^3) indicates an electron density loss after bonding. Image adapted from Ref. [65]. (c) Sketch of the 4 × 4, the 2 × 2, and the 1 × 1 supercell.

atom site (T) [45,79,80]. The position of such adsorption sites is depicted in Figure 2.1a. The H site remains the most stable adsorption site, even when the adatom concentration is varied [78,80]. In order to gain higher coordination in the H site, the adatom is also closer to the graphene sheet, reducing the electrostatic energy [45]. In addition, the adsorption of an alkali metal on graphene causes a negligible distortion of the graphene lattice [34,79].

The distance between the adsorbate and the graphene layer, h, shows a strong coverage dependence. An increase in the coverage corresponds to stronger dipole–dipole repulsions that cause a less negative adsorption energy and an increase in h [78,80,81]. Jin *et al.* [78] reported a minimal value for h (2.12 Å for Na, 2.54 Å for K, 2.69 Å for Rb, and 2.79 Å for Cs) at a coverage of about 0.03 adatom/C, corresponding to a (4×4) supercell for all alkali metals, with the exception of Li, for which the minimum value $h = 1.51$ Å occurs at a coverage of about 0.07 adatom/C, corresponding to a $(\sqrt{7} \times \sqrt{7})$ supercell. The authors explained this behaviour in terms of Coulomb attraction between the adsorbate and the graphene, which is enhanced by increasing coverage up to 0.04 adatom/C. Above this coverage, the charge transferred by the adatom to the graphene decreases, reducing the Coulomb attraction and, as a consequence, h increases. A minimum for h has also been reported by Dimakis *et al.* [81] for Li and K, with the minimum found at the same density of about 0.03 adatom/C for both metals, while no minimum has been reported for Na.

One of the most used methods to calculate the charge transferred by alkali metals to graphene, Δq, is from DOS calculations, which analyse the Fermi level shift with respect to the Dirac point [44]. The Fermi level, and thus Δq, depends on the coverage that is given by the supercell size in the simulations [79]. Δq decreases with the coverage, and this result has been obtained independently on the method used to calculate the charge transfer [77, 78, 80, 81]. At low coverage, the s electron of the alkali metal is completely transferred to the graphene[1] [34,65,77,78]. In the work of Jin *et al.* [78], Δq decreases as the inverse of the coverage for a coverage above 0.04 adatom/C for all alkali metals except Li, for which it begins at above 0.08 adatom/C. Furthermore, Li transfers more charge to the graphene than Na or K [78]. This difference has been attributed to the smaller ionic radius of Li, which affects the onset of the dipole moment depolarisation fields at the adatom-graphene interface. The simulated bonding charge density distribution, reported

[1] In Ref. [65], a charge $\Delta q \sim 0.5e$ was reported for Na and K at low coverage. It should be noted that in that work Δq was calculated using the Mulliken population analysis instead of the DOS analysis.

in Figure 2.1b from Ref. [65], indicates that the charge transferred from the alkali metal is delocalised.

The adsorption energy, E_{ads}, is calculated as the difference between the energy of the system made up by the adatom on the graphene and that of the isolated graphene and the isolated adatom [34, 45, 79]. For highly polar-bonded adatoms as like alkali metals, E_{ads} and the charge transfer result from a balance of the electronic energy of the electrons transferred to the graphene, the Coulomb interaction between the charged adatom and the surface, and the short-range adatom dipole–dipole repulsion [71]. The studies performed by Lugo-Solis and Vasiliev [77] on K adsorbed on graphene highlighting the dependence of E_{ads} on the size of the supercell. This dependence indicates the existence of long-range interactions between the graphene surface and the K adatoms, which the authors introduced in their model as classical electrostatic interactions. In the DFT calculations performed by Jin *et al.* [78], E_{ads} exhibits a weak parabolic-like behaviour with respect to the coverage, with a minimum of E_{ads} absolute value for a coverage of about 0.07 adatom/C for all alkali metals. This effect is more pronounced for Na, while it is negligible for Cs and Li. At high coverage, adatoms become more closely packed and start to form metallic bonds with each other, leading to a weaker adatom–graphene interaction and a less negative resultant adsorption energy [81]. The relatively high ratios of adsorption energy to bulk cohesive energy, ranging from 0.60 for Na to 1.80 for Cs, suggest that alkali metals are able to form 2D layers on the surface of graphene (in agreement with experiments observing 2D alkali metal layer formation on graphite [71]) [65]. An exception was provided by the simulations of Liu *et al.* [82] on Li nucleation on graphene. These authors found that the concentration of Li affected the nucleation barrier, leading to the formation of Li clusters at high coverage. Clusters containing less than 7 Li atoms have been predicted to prefer three-dimensional shapes.

The nature of the interactions between alkali metal adsorbates on graphene is still subject for discussion. For example, a repulsive dipole–dipole interaction has been reported for K adatoms on graphite [83]. A study on Cs adsorption on graphene instead identified a repulsive Coulomb interaction extending over larger distances[2] as the typical kind of interaction between adatoms [70]. A further work on K adsorbed on graphene reported a screened Coulomb interaction, originating from graphene electron density oscillations

[2]Song *et al.* [70] found an electrostatic potential between Cs ions on graphene decaying as $1/r$, that is much slower than the $1/r^3$ decay reported for Cs ions on graphite.

induced by the positively charged adatoms [84].

The binding energy calculated for the H, B and T sites has led to the identification of H as the energetically most favoured adsorption site. Nevertheless, the differences in the binding energy for these three sites is small (see, e.g., Ref. [45] and Ref. [79]), leading to a small activation barrier for diffusion. The diffusion barrier of alkali metals on graphene have been found to be in the range of 0.03–0.16 eV, with the exception of Li, for which the diffusion barrier is higher (0.3 eV) [45, 65]. Thus, at room temperature, alkali metals are highly mobile. Among the two possible diffusion paths, H–T–H and H–B–H, the diffusion through the bridge site has been reported to be the minimum energy path [80,85]. The diffusion barrier, moreover, decreases with an increase in coverage [80]. The smaller diffusion barriers and larger adsorption energies for Cs and K promote the continuous growth of 2D layers on graphene, while the larger diffusion barriers for Li and Na lead to the formation of small islands [79].

2.1.2 Adsorption on SiC-supported graphene

This subsection is devoted to alkali metals deposited on the surface of SiC-supported graphene. Together with adsorption on the surface, intercalation between the graphene and the buffer layer, and between the buffer layer and the Si substrate may also occur. The intercalation of alkali metals in SiC supported graphene is detailed in section 2.2.3.

Graphene epitaxially grown on SiC(0001) exhibits a very weak interaction with the substrate, and an extremely low number of defects. The first carbon layer, called the 'buffer layer', is bonded covalently to the substrate and does not exhibit graphene-like features. Its presence allows the second carbon sheet, the graphene layer, to exhibit electronic properties very similar to those of free-standing graphene [86]. The interaction between the substrate and the graphene gives rise to a downshift of the Dirac point of about 0.4 eV with respect to the Fermi level [47]. Moreover, the difference between the lattice constant of SiC (3.07 Å) and of graphene (∼2.46 Å) gives rise to a $(6\sqrt{3} \times 6\sqrt{3})$ graphene commensurate superstructure rotated 30° with respect to the substrate [87], with valleys related to regions of lattice matching and rims made up by regions of lattice mismatch (Figure 2.2a).

The growth morphology of Li at room temperature has been investigated by Virojanadara *et al.* [68] using the LEEM. After Li deposition, the formation of islands about 70 nm wide was observed (Figure 2.2b). Coalescence of these islands has been reported,

both with time and with annealing.

In contrast to Li, small amounts of Na deposited on SiC supported graphene form linear chain structures, aligned along the threefold symmetric directions of the substrate (Figure 2.2c) [69]. With higher coverage, such chains coalesce into islands characterised by the same 6×6 corrugation of SiC supported graphene.

The formation of an ordered structure has also been reported for Cs by Song *et al.* [70]. Differently from the works cited above, Cs has been deposited on a cooled graphene sample (150 K), and imaged in an STM at 4.8 K in the Song *et al.* experiments. No Cs superlattice has been observed, but rather hexagonal structures with short-range ordering and with an average distance between the adatoms of 1.85 nm for a coverage of 1 adatom per (6×6) superstructure unit cell (Figure 2.2d). Such distance is equal to the periodicity of the graphene (6×6) superstructure imaged by STM for SiC-supported graphene (Figure 2.2a). The rim region of the graphene layer, indicated in Figure 2.2a, exhibits a large surface curvature and, thus, is an energetically favoured adsorption site for adatoms [35], as confirmed by the observation of 95% of the deposited Cs on the rim regions and from the difference in the binding energy for Cs $\Delta E_\mathrm{b} \sim 50\,\mathrm{meV}$ between the rim and in the valley region, as calculated by DFT [70]. In the same work, Song *et al.* [70] analysed the distance r between nearest-neighbour Cs adatoms, finding an interadatom potential $E(r)$ decaying as $1/r$ for small distances. This behaviour differs from the $1/r^2$ decay observed for Cs adsorbed on graphite [71], suggesting a weaker electron screening in graphene. From these results, the authors concluded that the interaction between Cs adatoms is a long-range electrostatic repulsion originating from a charge of 0.33 e transferred from each Cs adatom to the graphene. ARPES studies performed by Watcharinyanon *et al.* [72] have confirmed the charge transfer from Cs to graphene; the n-doping of graphene is indicated by a shift of the Dirac point below the Fermi level by about 1.0 eV. The same result has been found for Rb as well. Moreover, the single π-cone in the reported ARPES spectra indicates no intercalation for those two alkali metals. From the linear dispersion near the Dirac point, an electron doping concentration of $n \sim 1.5 \times 10^{14}\ \mathrm{cm}^{-2}$ has been estimated for both Cs and Rb. In the case of Cs, the π-cone at the Dirac energy is slightly curved.

A more pronounced distortion of the π-band has been reported for high K coverage in Bostwick *et al.* [73]. In this case, a diamond-like shape has been observed around the Dirac point, which has been interpreted as a signature of the electron–plasmon bound states, the so-called plasmarons. In this study, an electron doping concentration of $n =$

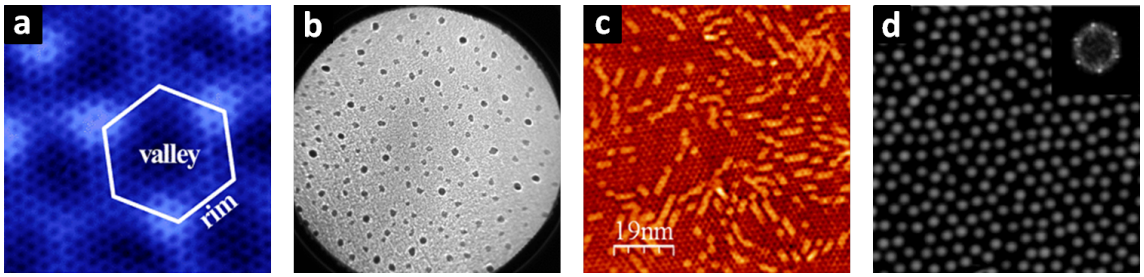

Figure 2.2: Alkali metals adsorbed on SiC supported graphene. (a) STM image of graphene on SiC substrate; imaging conditions: $V = 30\,\mathrm{mV}$, $I = 0.1\,\mathrm{nA}$. The field of view is 5 nm. The graphene honeycomb lattice is superimposed onto the 6×6 corrugation background, which is indicated by the white hexagon. The region in the middle of the hexagon exhibits graphene and SiC lattice matching, the so called valley region. On the contrary, the hexagon line is on the rim region, a region of lattice mismatch. Image adapted from Ref. [70]. (b) Li islands acquired by LEEM with an electron energy of -0.5 eV. The field of view is $50\,\mu\mathrm{m}$. Image adapted from Ref. [68]. (c) STM image of Na chains observed at low coverage; imaging conditions: $V = -2.18\,\mathrm{V}$, $I = 62\,\mathrm{pA}$. Image adapted from Ref. [69]. (d) STM images of 1 ML Cs adsorbed on graphene. The field of view is 30 nm and the imaging conditions are $V = 1.5\,\mathrm{V}$ and $I = 0.1\,\mathrm{nA}$. Image adapted from Ref. [70].

$0.5 \times 10^{13} - 5.2 \times 10^{13}\,\mathrm{cm}^{-2}$, one order of magnitude smaller than the value reported for Cs and Rb in Watcharinyanon *et al.* [72], was found.

2.1.3 Adsorption on metal-supported graphene

Transition metals have been widely used as substrates for graphene. According to Wintterlin and Bocquet [49], they can be classified into two categories: substrates on which graphene is chemisorbed, such as Co, Ru, Ni and Pd, and substrates on which graphene is physisorbed, such as Ir, Cu, Au and Pt. The first case is characterised by a substantial overlap between the π-band of graphene and the d-band of the metal substrate, distorting the Dirac cone, and causing a gap to open at the K point. In the second case, the interaction between the substrate and the graphene layer is weaker, and the Dirac cone is preserved; nevertheless, a gap opening is still present, due to charge-transfer effects at the interface. Alkali metal adsorbates can be used to reduce this band gap providing a route to decouple graphene from the metal substrate [74].

The lattice mismatch between graphene and the transition metal substrate gives rise

to the graphene ondulation and to the so-called Moiré pattern, i.e., a hexagonal graphene superstructure with periodicity of 20–35 Å resulting from overlaying the graphene hexagonal lattice with the metal substrate lattice. The graphene corrugation is more pronounced on substrates strongly interacting with graphene, while it is flatter on substrates weakly interacting with graphene [88]. Moreover, inequivalent regions can be identified within one Moiré supercell, due to the variation of the chemical bond strength across the supercell [88, 89].

Among the transition metals, Ni with the crystallographic orientation (111) has been reported to be the substrate with the lowest lattice mismatch with graphene (only ∼1.2%), allowing for epitaxial growth of graphene without Moiré patterns [90]. It has been reported, moreover, that in Ni-supported graphene (graphene/Ni) the coupling between the graphene layer and the substrate is strong, and the band structure exhibits an intact Dirac cone with the Dirac point placed 2.8 eV below the Fermi level [74, 91].

Matyba *et al.* [74] demonstrated the possibility of reducing the graphene/Ni band gap by mean of Na adsorption onto the graphene layer [74]. ARPES spectra show an energy gap reduced to 1.3 eV after Na adsorption on the graphene surface. This moderate decoupling is attributed to the n-doping of graphene from Na, which reduces the overlap of the atomic orbitals of graphene with those of the substrate. An almost complete decoupling is achieved upon Na intercalation.

Ir(111) is a substrate exhibiting a weak interaction between the substrate and the graphene layer and by a large interlayer distance, ranging from a minimum of 3.77 Å to a maximum of 4.04 Å, between the Ir(111) substrate and the corrugated graphene [92]. In addition, the theoretical work of Feibelman on this system has suggested that the graphene carbon atoms in the valley regions are characterised by an enhanced reactivity to adatoms binding on top of the graphene surface [93]. Epitaxial graphene grown on Ir is characterised by a sharp Dirac cone and a small gap at the K point, with the Dirac point located at 0.10 eV above the Fermi level [94]; thus, graphene is slightly p-doped.

Petrović *et al.* [75] reported ARPES data acquired around the graphene K point for Cs coverage from 0 to 0.1 ML[3]; these spectra show the Dirac cone shifting to higher binding energies with Cs coverage. The shift of the Dirac point to 0.2 eV below the Fermi level indicates slightly n-doped graphene with a maximum electron doping of $n \approx 4\times10^{12}$ cm^{-2}. This value corresponds to 0.11 e transferred from each Cs adatom to graphene. Low-

[3]Here, 1 ML is defined as the coverage of the $(\sqrt{3} \times \sqrt{3})$R30° structure relative to Ir(111).

temperature STM data show a hexagonal ordering, which is originated by the Coulomb repulsion between the Cs adatoms.

K deposited on graphene/Ir has been investigated at a coverage for which a (2 × 2) superstructure can be identified by LEED, corresponding to the KC_8 phase in alkali metal GICs [76] (see section 2.2.1). The Dirac point was found to shift to 1.29 eV and the electron doping was $n \approx 1 \times 10^{14}$ cm^{-2}, and thus each graphene unit cell has a doping level of 0.054 extra electrons. The authors reported, moreover, the formation of K islands with a (2 × 2) periodicity.

2.1.4 Adsorption on graphite

Experimental studies on alkali metals adsorbates on graphite surface are challenging since all alkali metals, except for Na, readily intercalate into graphite [64]. A successful deposition of an alkali metal overlay requires the graphite substrate to be cooled to a temperature of about 100 K; this condition ensures an intercalation process slow enough to consider the system under stable conditions, allowing diffraction and spectroscopic studies of alkali metal adsorbates on graphite to be performed [71]. A detailed description of alkali metal adsorption on graphite can be found in Caragiu and Finberg's review paper [71]; the main findings of their review are reported below.

The alkali metals with a larger atomic radius, namely K, Rb and Cs, show very similar phase diagrams [71, 95–97]. A dispersed phase is observed below a critical value for the coverage. Adatoms do not show long-range order but assume a definite nearest-neighbour distance. The reason for a dispersed phase at low coverage has been found in the Coulomb repulsion between the alkali metal atoms ionised upon adsorption and the polarisation of the graphite substrate [71]. At coverages between this critical value and almost 1 ML, these three metals show the coexistence of two phases: one phase is characterised by atoms dispersed on the graphite surface, while the second one is a condensed phase exhibiting close-packed islands[4]. An increase in coverage implies a decrease in the distance between adsorbates. The close-packed configuration is, in this case, energetically more favourable than the dispersed one, and the adatoms tend to form islands with a (2 × 2) structure. In the case of Cs, an additional phase has been reported between the critical coverage and an intermediate phase exhibiting a $(\sqrt{7} \times \sqrt{7})$R19° superstructure. With a further

[4] A closed-packed configuration at submonolayer coverage for K, Rb and Cs adsorbates on graphite and graphene corresponds to a (2 × 2) overlay structure.

increase in coverage, the dispersed phase reduces, and islands grow to form a (2 × 2) monolayer [71, 97]. It has been observed that such a condensed phase is more stable than the dispersed phase against alkali metal intercalation, being the energy necessary to detach an atom from a (2×2) island (0.86 eV for K) above the diffusion energy barrier for a single adsorbate (0.22 eV for K) [71]. In the phase diagram of Na, the existence of a critical coverage($\rho_C \simeq 1.5 \times 10^{14}$ Na atoms cm^{-2}) below which the Na adatoms are in a dispersed phase, has again been observed. Unlike K, Rb and Cs, the dispersed phase coexists with bcc(110) microcrystals between the critical coverage and almost 1 ML. At 1 ML, the graphite surface is covered by bcc(110) close-packed Na atoms. Concerning Li, no ordered phases have been observed down to 80 K [98], suggesting the need to keep the substrate at even lower temperatures in order to reduce the intercalation rate [71, 95].

As mentioned previously, alkali metals easily transfer their outermost electron to graphite. Most of the results cited by Caragiu and Finberg suggest an ionic bond between K and graphite, with a charge transfer in the range of 0.15–0.7 e per K atom in the dispersed phase [71]. With increased coverage, and so with an increase in (2 × 2) islands size, the charge transferred to graphite is reduced. Concerning Cs and Rb, there is a lack of studies on the charge transfer from these alkali metal overlays to graphite. In the case of Cs, a few disagreeing values have been reported; for example, Johnson *et al.* reported an almost complete charge transfer of 0.9 ± 0.1 e/Cs atom at high coverage [95], while Gleeson *et al.* reported a complete charge transfer with low coverage that evolved into an incomplete alkali ionisation of 0.6–0.8 e/Cs atom at high coverage [99]. To the best of my knowledge, the charge transfer of Rb adatoms on graphite has not been investigated at all. The charge transferred from Na to graphene has been found to be very small (below 0.2 e per Na adatom) independently of the coverage [95, 99]. This extremely weak interaction with the graphite surface has been considered to be the reason for which Na is unlikely to intercalate into graphite [95]. The charge transferred from Li to graphene amounts to 0.9-1 e/Li atom for 1 Li adatom on a (4 × 4) graphene supercell, as calculated by Valencia *et al.* [100]. Li exhibits the highest charge transfer compared to those reported for K (0.84 - 0.81 e/K atom) and Na (0.79 - 0.73 e/Na atom). The amount of charge transferred by K, Na and Li follows the same order as their ionization potentials (K > Na > Li).

2.2 Alkali Metal intercalation

This section reports the literature findings on alkali metals intercalated in graphite and supported graphene.

The insertion of alkali metal atoms in between the carbon layers of graphite give rise to the so called GICs; their highly ordered structure, depicted in Figure 2.3, allows for a controlled tuning of the graphite free carrier concentration. The charge transfer from the intercalated alkali metal layer to the graphite layers, where carriers have higher mobility, results in an increase of the GIC conductivity. This leads to in-plane superconductivity, as reported for Cs, Rb and K stage 1 GICs [64].

Although it is well known that a perfect layer of graphene is impermeable to gases (even for hydrogen atoms) [101–103], alkali metals have been observed to intercalate in supported graphene at room temperature [68, 75, 76, 104–109]. The potentialities of the intercalation, as a route to decouple the graphene layer in order to obtain a quasi-free-standing graphene, have been widely explored [66,67]. However, a few experimental works have been dedicated to understanding the intercalation mechanism of alkali metals between the graphene layer and its substrate.

2.2.1 Intercalation in graphite

Alkali metal-intercalated graphite has widely been studied for the property of alkali metal atoms to act as electron donors. The charge is transferred from the intercalated layer, having a low carrier mobility, to the graphite layers, where the carrier mobility is high, resulting in an increased conductivity of the GIC [64].

GICs are characterised by the so-called staging phenomenon, i.e., the regular succession of a completely or partially filled interlayer and a number, n – called the staging index – of graphite layers[5], as illustrated in Figure 2.3. The intercalation of foreign specimens in between the graphite layers proceeds in a regular way; the regular distribution of intercalants between graphite layers has been shown to be a configuration minimizing the energy necessary to delaminate the graphene sheets. The properties of GICs are strongly influenced by the concentration of the intercalants, which can easily be estimated from the staging index [64].

[5] As an example, a GIC in which all graphene interlayers are filled by an intercalant gives rise to a stage 1 compound, there being one graphite layer between two subsequent intercalant layers.

Although GICs are typically prepared through the two-zone vapour transport method[6], it is also possible to obtain them by in situ evaporation on the graphite surface, as first reported by Lagues *et al.* [110]. The intercalation phenomenon for alkali metals on graphite has represented a limiting factor for the study of alkali metal overlays [71]. Experiments have shown that alkali metals readily intercalate into graphite at temperatures above 190 K for K [95, 111], and above 100 K for Li [95]. It has been found that all alkali metals form stage 1 intercalation compounds, except Na, which has been observed only as stage 8 compound [64, 71].

Despite the intercalation process being different, depending on the guest specimen, the main pathway is the same: the intercalation is initiated at the edges of the graphite crystals, and proceeds by an intricate diffusion process along and between the host carbon sheets [64]. The size and the kind of graphite sample also play a role in the diffusion process. Intercalation is faster and more uniform in a thin, small sample than in a thick, large one, and faster in single-crystal graphite than in highly-oriented pyrolytic graphite (HOPG).

Cs, Rb and K share a common intercalation mechanism. These metals are characterised by a first ionisation potential (4.34 eV for K, 4.18 eV for Rb and 3.89 eV for Cs [112]) lower than the graphite electron affinity, which has been reported to be 4.6 eV [112, 113]. Cs, Rb and K interact with graphite through a complete charge transfer[7] (for a staging index $n \geq 2$) [114, 115], that provides the host enough energy to overcome the van der Waals interaction between the graphite layers, and the carbon sheet's strain energy, thus allowing the alkali metal to readily intercalate.

The first ionisation potential of Li (5.39 eV) is higher than the graphite electron affinity, making intercalation a less favourable process. Nevertheless, the small size of the Li atom (1.52 Å of atomic radius) with respect to the graphite interlayer distance (3.35 Å), together with its high mobility (characterised by an activation energy for diffusion of 0.2 to 0.4 eV for low coverage), favours Li intercalation into graphite [116]. Similar to Li, the first ionisation potential of Na (5.14 eV) is above the graphite electron affinity. In contrast

[6]The intercalant is heated at a temperature T_{I} high enough to produce the vapour phase; the graphite is placed at some distance from the intercalant and is heated to a temperature $T_{\mathrm{Gr}} > T_{\mathrm{I}}$. The graphite sample is surrounded by the intercalant vapour; and the intercalation process starts when the vapour pressure is above a critical value [64].

[7]For Cs GIC prepared by Cs evaporation onto single-crystal graphite and HOPG under UHV conditions, a slightly lower charge transfer has been reported by Lagues *et al.*: 0.95 e/Cs atom for the stage 2 (CsC_{24}) and 0.7 e/Cs atom for the stage 1 (CsC_8) GIC [110].

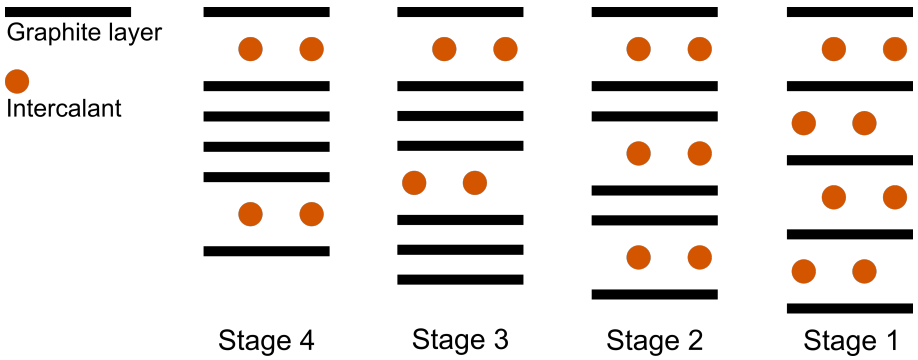

Figure 2.3: Sketch of stage 4, stage 3, stage 2, and stage 1 graphite intercalation compound. The staging index n is the number of graphite layers between two consecutive intercalant layers.

to Li, Na intercalation requires a higher strain energy to expand the graphite interlayer distance. This high energy required to intercalate could contribute to explain the absence of a Na stage 1 graphite compound, but it does not describe the intercalation observed with the larger alkali metals, i.e. Cs, Rb and K. A description of the Na intercalation was completed by the theoretical work of Liu *et al.*, in which it was outlined that the Na chemical binding to a specific substrate is generally the weakest, compared to all the other alkali metals. This behaviour originates from competition between the ionisation energy and the coupling between the ion and the substrate [117]. Nevertheless, the possibility to enhance Na intercalation, using a graphite with increased interlayer distance by means of other species intercalation, has been demonstrated [118]; the optimum graphite interlayer distance for that is 4.3 Å [117].

2.2.2 Intercalation in metal-supported graphene

The problem of the Cs intercalation mechanism in Ir(111)-supported epitaxial graphene has been addressed by Petrović *et al.* [75]. Their experiment demonstrates that the intercalation dynamic is promoted by vacancy defects, present at the intersection of wrinkles, which act as entrance points. The intercalation has been found to start after a critical coverage of about 0.06 ML. At lower coverage, Cs adsorbs on graphene with a partial delocalisation of the s-electron. With increasing coverage, the Coulomb repulsion becomes significant, causing a decrease in the binding energy, and an adatom–adatom repulsion that acts as a 2D pressure; the intercalation takes place in order to reduce such pressure.

At a coverage lower than 0.06 ML, intercalation is prevented by the high energy cost (of about 50 meV per C atom [119]) to delaminate graphene from the substrate. The presence of a dense phase of Cs adatoms allows sharing of such an energy cost among more adatoms, and intercalation can then take place. For higher coverage, the intercalation is regulated by the interplay between the intercalated phase and the adsorbed phase. LEED data have not shown any superstructure of the intercalated phase for coverages below 0.9 ML. At 0.92 ML, a (2×2) superstructure, relative to graphene, has been observed, which, for higher coverage, mixes with a $(\sqrt{3} \times \sqrt{3})$R30° structure relative to Ir. At a coverage of 1 ML, only this last superstructure with respect to Ir has been observed for the intercalated phase. These findings have been confirmed by high-resolution STM data, which showed, in addition, a height of the intercalated region apparently 0.4 nm higher than the non-intercalated one. The ARPES spectra for the adsorbed phase, i.e., at coverage below 0.06 ML, have shown an increase in the binding energy with Cs coverage, and a shift of the Dirac point below the Fermi level by 0.2 eV. For this phase, the maximum charge transferred is $0.11e$ per Cs adatom, which corresponds to an electron concentration of $\sim 4 \times 10^{12}$ cm^{-2}. At an intermediate coverage of 0.06–0.9 ML, the coexistence of two phases—the adsorbed and the intercalated phase—is demonstrated by the presence of a further Dirac cone at higher binding energies. Further Cs evaporation leads to the coverage of 1 ML, characterised by a charge transfer of 0.20 e for each Cs atom corresponding to an electron concentration of $\sim 1 \times 10^{14}$ cm^{-2}. Cs intercalation at room temperature has been reported also for Ni(111) supported graphene. As for Ir supported graphene, a (2×2) superstructure relative to the intercalated phase has been observed [104].

K intercalated in Ir(111)-supported graphene has been investigated by Bianchi *et al.* [76] and Struzzi *et al.* [105] through ARPES and LEED investigations. In the Bianchi *et al.* experiment only the KC_8 phase, corresponding to a (2×2) superstructure in K GICs, was considered. At this K concentration, the authors observed a shift of the Dirac point below E_F to a binding energy of 1.29 eV, with a doping level of 0.054 e per unit cell of graphene (equivalent to an electron concentration of $\sim 1 \times 10^{14}$ cm^{-2}, similar to what has been reported for Cs at the same coverage [75]). Moreover, they reported that, in Ir-supported graphene, it is not possible to continuously vary the doping level since K readily forms islands with a (2×2) supercell. At lower K concentrations, the ARPES spectra show two bands, one corresponding to the clean Ir-supported graphene, the other to the KC_8 phase. This observation has not been reported for SiC-supported graphene,

which can be doped continuously with K [76]. The experiments performed by Struzzi *et al.* [105] are characterised by a stepwise deposition with ARPES and LEED data acquired between each step. The ARPES data showed a Dirac point downshifted with respect to E_F by 1.30 eV and a charge transfer of 0.041 e per C atom. Similar to what has been reported for Cs [75], the coexistence of an adsorbed phase and an intercalated phase with a $(\sqrt{3} \times \sqrt{3})$R30° periodical structure at low K coverage has been observed [105]. The $(\sqrt{3} \times \sqrt{3})$R30° superstructure has been reported also by Nagashima *et al.* for K intercalated in Ni(111) supported graphene [104].

Although Na is the only alkali metal not intercalating in graphite [64, 95], Na intercalation in metal supported graphene is still disputed. Na intercalation in Ir(111) supported graphene has been reported by Pervan *et al.* [120]. The authors have proposed the same intercalation mechanism as reported for Cs [75]: namely that Na is preferentially adsorbed on graphene up to a coverage of 0.4 ML; above this value, the "2D pressure" caused by the adatom–adatom repulsion favors the Na intercalation, and the coexistence of an adsorbed and an intercalated phase is observed. In the end, only the intercalated phase has been detected and no extra Na adsorption can be observed. Fully intercalation for Na deposited at room temperature has been reported also by Gall *et al.* [121] and by Langer *et al.* [122]; on the contrary, no Na intercalation has been reported by Papagno *et al.* [123], but rather the formation of single layer islands. Concerning Na intercalation on Ni supported graphene, Na intercalation reported by Park *et al.* [124] is contradicted by Matyba *et al.* [74], who found intercalation to occur only at high temperatures.

Petrović *et al.* [75] investigated also Li intercalation in Ir supported graphene. In contrast to Cs, they found that Li intercalates at any coverage. The presence of just one Dirac cone in the ARPES spectra at any doping level confirmed that only the intercalated phase was present. Li can easily intercalate because of its small dimension, needing less energy to delaminate graphene from Ir(111)[8]. In general, the better screening of Li ions close to the Ir substrate makes the intercalated phase a favoured configuration. DFT calculations for Li on graphene/Ir(111) also support the intercalation being energetically favoured over the adsorption at all coverages, with a difference the binding energies for the adsorbed and the intercalated phase varying from 1.55 eV to 0.99 eV per Li unit cell for a dilute and dense Li structure, respectively. The intercalation dynamics, as in the

[8] In fact, considering the difference between the graphene-Ir distances in the case of adatoms and of intercalated phase, such distance vary from 1 Å in the diluted (4×4) Li superstructure to 1.23 Å in the dense (1×1) Li superstructure.

case of Cs, is promoted by the presence of vacancies.

2.2.3 Intercalation in SiC-supported graphene

As mentioned in section 2.1.2, graphene epitaxially grown onto 6H-SiC(0001) is composed of a buffer layer and a top graphene layer. The presence of a buffer layer, covalently bonded to the Si substrate, has been seen as an impediment to the development of electronic applications, and the need to decouple it from the substrate has motivated studies on intercalation.

Virojanadara *et al.* have widely studied Li intercalation in SiC-supported high-quality graphene [68, 106]. LEEM images have shown that, immediately after Li deposition, the graphene surface is less smooth, having a granular appearance and showing severe defects, such as wrinkles and cracks. Such defects were not disappearing even upon high-temperature annealing. Furthermore, small islands were formed on the graphene, coalescing with time [68, 106]. The electron reflectivity curves acquired after Li deposition showed two minima (at energies of -0.4 eV and 5 eV), indicating the presence of two graphene sheets. Such spectra suggested that Li was intercalated between the substrate and the buffer layer, decoupling them and, thus, transforming the buffer layer into a second graphene layer. A shift to lower electron energy of the reflectivity threshold has been reported, indicating a sample work function decrease caused by Li intercalation. The decoupling of the buffer layer by Li intercalation has also been confirmed by photoelectron spectroscopy, in which the patterns exhibited two π-cones after Li deposition [68]. The μ-LEED pattern has shown the diffraction pattern of the $(\sqrt{3} \times \sqrt{3})$R30° structure together with the diffraction spots of the graphene (1×1) lattice, that corresponds to the pattern of a C_6Li compound. These results have also been confirmed by X-ray photoelectron emission microscopy (XPEEM) data [68, 106]. The presence of three π-bands at the K point in the ARPES spectra, representing a mixture of monolayered and bilayered graphene with different doping, indicates that the distribution of intercalated Li atoms is irregular. The graphene-doping by Li lowers the Dirac point that has been reported to be 0.25–0.5 eV [68].

An analogous experiment on a sample made only of the Si substrate and the C buffer layer has been performed by Virojanadara *et al.* [106]. Also in this case, LEEM images showed a morphology change of the surface after Li deposition with several dark spots and a rough surface. Differently from the SiC-supported graphene case, after Li deposition,

the surface exhibited a smaller amount of wrinkles and cracks and, moreover, the acquired μ-LEED patterns did not contain indications for the $(\sqrt{3} \times \sqrt{3})$R30° superstructure observed in the case of Li atoms deposited on the surface of SiC supported graphene. The appearance of the diffraction pattern relative to the (1×1) graphene structure in the μ-LEED pattern, together with the appearance of a π-cone at the K-points in the first Brillouin zone in the photoelectron angular distribution patterns, are an indication that Li is intercalated between the buffer layer and the substrate. The effect of the intercalation is the transformation of the buffer layer into a doped graphene layer having the Dirac point shifted downwards with respect to the Fermi level by 1 eV.

Li intercalation between both the substrate-buffer layer and the buffer layer–top graphene layer has also been confirmed by other experimental studies [107, 108]. ARPES data reported by Bisti *et al.* [107] have shown a strongly n-doped graphene. Although the substrate is decoupled by Li intercalation, some substrate influence on the graphene band structure still remains. From a comparison of ARPES spectra with band structure calculations, Caffrey *et al.* [108] found that the top graphene layer has been shifted from an AB to an AA stacking upon Li intercalation.

A further study on Li intercalated between graphene and SiC substrate, and between the carbon buffer layer and the Si substrate have been reported by Fiori *et al.* using STM and LEED [109]. Their observed diffraction patterns are in agreement with those reported in the above mentioned works [68, 106, 108]. Of interest in the Fiori *et al.* study is the analysis of the intercalation evolution for increasing coverage. Li intercalation has been reported to start at the interface at the SiC step edges, forming homogeneous intercalated stripes that grow inward with increasing Li deposition, until the whole graphene layer above the SiC terrace has been populated. After the deposition of 0.28 ML of Li, dark spots in the STM images were observed. These indicate Si atoms not bound to Li, and an incomplete Li intercalation between the buffer layer and the Si substrate has been thus evolved. Once the intercalation has been completed there, Li intercalation continued between the decoupled buffer layer and the top graphene layer. At a coverage of 0.56 ML, the $(\sqrt{3} \times \sqrt{3})$R30° superstructure, which corresponds to the intercalation between two graphene sheets, has been reported. Moreover, and differently from what was reported by Virojanadara *et al.* [68, 106], Li clusters were not observed on the graphene surface. Li atoms, evaporated onto the buffer layer at room temperature, intercalated between the carbon layer and the substrate, forming islands that grew in diameter with increased

coverage. The buffer layer was almost entirely decoupled from the substrate at coverages above 0.28 ML. The height for all the islands formed was identical and found to amount to 2.6 Å. The growth conditions used to prepare these samples[9] lead to the formation of large islands of carbon layers in the middle of the substrate terraces. Thus, the substrate step edges are covered less by the buffer carbon layer, making an intercalation mechanism starting from the substrate step edge unlikely. Fiori *et al.* explained the presence of stripes and islands in the intercalated phase with the limited diffusivity of Li in the SiC supported graphene at room temperature [109]. This observation is in contrast with the measured Li diffusion coefficient in bilayer graphene, up to $7 \times 10^{-5}\,\mathrm{cm^2\,s^{-1}}$ at room temperature, reported by Kühne *et al.* [125]. However, it should be pointed out that the Kühne *et al.* experiment is based on a completely different setup, i.e. an electrochemical cell made up by a stripe of bilayer graphene on a SiO_2 substrate where Li intercalation is controlled through a gate voltage, and the Li presence is probed by Hall measurements along the graphene stripe. The authors found that no intercalated Li is present between the lower layer and the substrate in this setup, but Li diffuses only in between the bilayer graphene.

In contrast to Li, the deposition of Rb and Cs on SiC supported monolayer graphene did not result in intercalation [72]. It has been reported that Cs, Rb and K intercalate only in the case of SiC supported bilayer or few-layer graphene, in which alkali metals form an intercalated compound similar to the stage 1 GIC, but no intercalation between the substrate and the buffer layer has been reported [126, 127].

2.2.4 Intercalation in bilayer graphene

The interest in bilayer and FLG alkali metal intercalated systems has been driven by the requirement for stable n-doped graphene for potential electronic applications[10]. As in the case of single-layer graphene, there are much more theoretical works than experimental ones in the literature. All reported experiments have been performed on SiC(0001)-supported bilayer graphene, in which interaction with the substrate produces a band gap in the band structure at the K-point of $\sim 0.12\,\mathrm{eV}$ [52, 130].

The intercalation of Li into SiC(0001)-supported bilayer graphene has experimentally been investigated by Sugawara *et al.* [130]. Their reported ARPES data showed a Dirac

[9] The epitaxial monolayer graphene on SiC was fabricated by high temperature annealing of 6H-SiC(0001) under Ar at atmospheric pressure.

[10] In fact, alkali metal adatoms are unstable, since they can migrate and desorb under the application of an electric field or thermal stress, as observed in alkali metals on SiO_2 [128, 129], for example.

point down-shifted by 1.4 eV with respect to pristine bilayer graphene. A charge transfer of 1.07 ± 0.05 e to the two graphene layers has been measured, indicating fully ionised intercalated Li atoms. The intensity of the LEED spots, corresponding to the $(6\sqrt{3} \times 6\sqrt{3})$R30° structure of the pristine sample, were weakened with Li deposition indicating an expansion between the two graphene layers due to the intercalation, and new spots relative to the $(\sqrt{3} \times \sqrt{3})$R30° superlattice were produced. This periodicity is identical to that observed in stage 1 Li GICs. These results indicate that the deposited Li atoms was intercalated into the bilayer graphene in the same well-ordered manner as in a bulk Li GIC. For this system, the reported critical temperature for superconductivity is very low (0.17 K); however, theoretical calculations have predicted a much higher T_C ($\sim$ 14 K) for Li intercalated bilayer graphene with a Li overlayer because of the enhanced electron-phonon coupling due to the equal number of graphene and Li layers [131]. A comparison of the DFT calculated electronic structures of the stage-1 Li GIC, Li intercalated bilayer graphene and SiC-supported Li intercalated bilayer and trilayer graphene has outlined that all these systems are n-doped, and their charge carrier density is increased by a factor of $\sim$ 100 by Li-intercalation with respect to pristine bilayer graphene. Moreover, among these systems, free-standing Li-intercalated bilayer graphene exhibits the largest charge carrier densities [132]. For free-standing FLG, the simulations show a stronger tendency to intercalation for Li into the bilayer graphene [133]. The role of point defects[11] in Li intercalation in between bilayer graphene has been investigated in the theoretical work of O'Hara *et al.* [134]. They reported that the intercalation is energetically favoured with respect to the adsorption on both perfect and defective bilayer graphene, where point defects are present in only one of the two layers. Moreover, they found that the presence of the second graphene layer has an influence on the intercalation and deintercalation energy: the energy barrier for an intercalated Li atom to be overcome in order to exit through a point defect is higher than the energy barrier to intercalate through the same point defect.

The behaviour of Na on bilayer graphene has been analysed by Xia *et al.* [135] using LEEM, μ-LEED, μ-PES and XPEEM. The sample used was a furnace grown graphene on a SiC(0001) substrate, exhibiting areas of single-layer and bilayer graphene. After deposition, most of the Na remained on the surface, forming droplet-shaped clusters on the bilayer graphene areas, while a small amount of Na intercalated in the bilayer graphene

[11] Stone-Wales, monovacancy, divacancy, and trivacancy defects have been considered in the O'Hara *et al.* work [134].

and at the interface between graphene and the substrate. The intercalation increased with time and exposure to the electron and photon beams, and could be promoted by thermal annealing at 400 K. The intercalants were distributed homogeneously in both the single layer and bilayer areas, with the intercalation beginning at the domain boundaries between these areas. As in the case of Li, theoretical studies on Na intercalation in bilayer graphene, performed by Yang *et al.* [136,137], showed that intercalation of Na into bilayer graphene is energetically favoured with respect to the adsorption on the bilayer graphene surface and, moreover, that the intercalation in the AA-stacking is favoured over the intercalation in the AB-stacking, with the AB-stacking being the more stable lattice configuration. The interlayer distance increases with the number of Na atoms intercalated. The electron density calculations predicted a charge transfer from the intercalated Na in bilayer graphene to the 10 (A/Na/B) and 12 (A/Na/A) nearest carbon atoms. The charge distribution for Na adsorbed on bilayer graphene is delocalised similarly to what has been predicted for adsorption on single-layer graphene. The effect of defects was also investigated by Yang *et al.* [136, 137] who found a fast migration from pristine regions, characterised by a low migration energy barrier (0.15 eV on the surface and 0.32 eV between the bilayer graphene), to defective regions where the migration energy barrier is larger (0.59 eV on the surface and 0.56 eV between the bilayer graphene).

As reported in the ARPES studies performed by Ohta *et al.* on SiC(0001)-supported bilayer graphene [52], the presence of the substrate causes a slight n-doping of the bilayer graphene due to carrier depletion from the substrate. The authors showed that the n-doping can be enhanced by K deposition on the side facing the vacuum, which leads to a closing and reopening of the band gap with increasing coverage. It should be noted that the Ohta *et al.* experiments have been performed at low temperatures, and no evidence of K intercalation has been found. On the contrary, K deposited on SiC supported thin graphite overlays[12] at room temperature led to the formation of a stage-1 GIC [126]. The influence of the SiC(0001) substrate on the intercalation properties of bilayer graphene has theoretically been investigated by Kaloni *et al.* [138], who compared the first-principle calculations for K intercalated into free-standing bilayer graphene with those for supported graphene. For K intercalated bilayer graphene, Kaloni *et al.* found an interlayer distance of 5.60 Å. The observed Dirac cone was made up of twofold degenerate π and π^* bands

[12]The work of Algadal *et al.* [126] did not report the number of graphene layers. Nevertheless, the overlayer was thin enough to observe the substrate contribution in photoemission spectra.

shifted 1.0 eV below E_F and, differently from what was found for Li [132], did not exhibit distortions. The calculated charge transferred from K to the graphene layers amounted to 0.57 e, giving rise to a prominent n-doping and a carrier density 100 times larger than in pristine graphene on SiO_2. In the case of K intercalated SiC(0001)-supported bilayer graphene, the simulations have shown a buckling of the lower layer due to the bond to the Si and an interlayer distance of 5.99 Å. A perfect Dirac cone exhibits the π and the π^* bands crossing at 0.92 eV below E_F and a charge transfer from K to the graphene layers of 0.40 e was obtained. In this case the carrier density was larger than in the case of K intercalated in free-standing bilayer graphene. According to the authors, this was due to the charge transfer induced by bonding between the substrate and the lower graphene layer. Between the two systems, the free-standing one exhibits an electron-phonon coupling and a DOS(E_F) that resembles those of K-intercalated AA-stacked graphite and, thus, it could exhibit superconductivity under the same conditions [138].

The addition of a Cs overlayer on Cs intercalated bilayer graphene results in an enhanced electron–phonon coupling, as reported by Kleeman *et al.* [127]. LEED diffraction pattern showed the presence of a (2×2) structure similar to that of stage-1 GICs. The reported ARPES measurements exhibited a Dirac point at 1.38 eV, from which a total amount of charge transferred by the Cs to the graphene of 1.52 e per unit cell was calculated. This large coupling is caused by the Cs overlayer, which transfers additional electrons to the graphene and makes the bilayer structure more similar to the stage-1 GICs [127].

Kaneko and Saito performed systematic DFT calculations for alkali metal intercalated bilayer graphene for different amounts of intercalated atoms [139]. Their model revealed an interlayer distance proportional to the distance between the alkali ion and the free-standing graphene, that in turn grows with the ion size. The interlayer distance was growing slightly with the number of intercalated atoms. Formation energy calculations showed that systems with intercalated alkali metal atoms are more stable than those with alkali metals adsorbed onto the surface of the bilayer graphene. The formation of intercalated compounds has been found to be exothermic (negative formation energy), decreasing with coverage because of the strong lateral interactions. Na represents an exception among the alkali metals, with the formation of C_8NaC_8 being slightly exothermic and of C_6NaC_6 being slightly endothermic. The charge transferred from the alkali metal intercalated atom to the graphene layer also reduces with coverage but, even for a $(\sqrt{3} \times \sqrt{3})$ supercell, its

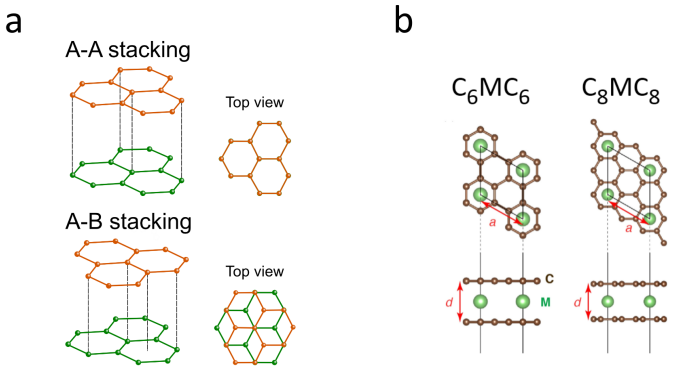

Figure 2.4: (a) Sketch of the AA-stacked and the AB-stacked bilayer graphene. (b) Scheme of the C_8MC_8 and of the C_6MC_6 intercalated AA-stacked bilayer graphene, where M is the intercalated metal. Adapted from [139].

value is quite large (e.g., the minimum value among alkali metals is 0.63 e for Cs).

2.3 Transition Metal adsorption

The interest in investigating transition metal adsorption on graphene is motivated by novel properties that can be used for a wide range of applications. As an example, nanoparticles of transition metals, especially palladium (Pd) and platinum (Pt), on carbon materials have been shown to be efficient composite systems for hydrogen storage [140, 141]. In fact, transition metal nanoclusters promote the H_2 dissociation into atomic H, which can be incorporated into the nanocluster lattice[13] [142]. This property, together with the localization of the nanoclusters, makes carbon supported transition metal nanoparticles an efficient system for catalysis applications [140,141,143–146]. Moreover, transition metal functionalised graphene is widely applied as a sensitive gas sensor with a very low detection limit [147–150].

In the following section, I will provide an overview of the nucleation properties of transition metals on graphene and graphite, focusing on experimental results involving Pd deposition.

[13] An example is the incorporation of H into Pd lattice through the following reversible reaction: $2\,Pd + xH_2 \longleftrightarrow 2\,PdH_x$, where $x \leq 1$ [142].

2.3.1 Transition metals on graphene

In this section, theoretical calculations on transition metals on free-standing graphene as well as experimental findings on transition metals evaporated on supported graphene will be reviewed. Metal nucleation on supported graphene is often studied using STM, allowing for the measurement of cluster size and density. Since theoretical prediction values depend strongly on the employed functional, they will be reported only for general trends predicted by simulations.

Adsorption on graphene: theoretical simulations

Theoretical studies report that metals with half-filled or filled *d*-shells interact weakly with graphene and are characterised by adsorption energies below 0.25 eV [151]; in this scenario, Pd is an exception as it is a filled *d*-shell metal but its adsorption energy on graphene amounts to 1.076 eV [86]. Pd adsorbs on graphite forming a covalent bond, transferring a charge of $q = 0.64\,e$ to the graphene; in contrast to the case of alkali metals, the charge is localized on the closest carbon atoms [34, 65, 151].

Liu *et al.* [34, 65, 86] performed systematic *ab initio* DFT studies on metal adsorption on free-standing graphene to find a correlation between the adsorption properties and the growth morphology. They reported that the growth morphology depends on two principal factors: the ratio between the metal adsorption energy E_{ads} and its bulk cohesive energy E_{c}, and the activation energy for adatom diffusion on graphene E_{diff}. The authors report that a small $E_{\mathrm{ads}}/E_{\mathrm{c}}$ ratio favours a 3D growth mode. From the classical nucleation theory, the condition for 3D growth is that $E_{\mathrm{c}} > E_{\mathrm{ads}}$, and in Liu's work it has been reported that $E_{\mathrm{ads}}/E_{\mathrm{c}} < 1$ for all transition metals considered. A high E_{diff}, since it determines the hopping probability, indicates an elevated rate of adsorbates joining each other to form new clusters, and therefore, a higher cluster density per unit area. Although these statements hold in general, they were not fully supported by experimental findings, which showed different growth morphologies depending on the metal deposited. It is necessary to point out that the experiments mentioned in the work of Liu *et al.* were performed on supported graphene, while their simulations were performed for free-standing graphene. As will be described in section 2.3.2, the presence of just one additional graphene layer is enough to substantially change the energetics of adsorbed metals. Examples of metals contradicting the previous hypothesis were provided by Pt and Co. At the same coverage, Pt exhibits a much higher cluster density than Co, in spite of the fact that the diffusion barrier for Co

is higher than that for Pt (see Table 2.1). These findings led the authors to include the interaction between adatoms as a further factor in the description of growth morphology. This assumption was justified by comparing the growth of Eu and of Dy, two metals characterised by similar $E_{\mathrm{ads}}/E_{\mathrm{c}}$ ratio and E_{diff} (Table 2.1). Dy adsorption on graphene induces a larger electric dipole moment and lattice distortion than Eu. The stronger repulsive interaction and the higher diffusion barrier for Dy promote the formation of small islands with a high island density. In contrast, Eu nucleates as big islands with a flat top. The authors' calculations also predicted thermal stability for transition metal nanoclusters on graphene. This finding was in agreement with experimental results showing cluster coarsening only upon thermal annealing.

The growth of Pd nanoclusters on graphene was also the topic of molecular dynamics simulations performed by Brault *et al.* [152]. Although this work was intended for Pd on graphite, it considered only interactions between the metal adatom and the graphite surface, neglecting the influence of the underlying layers. Therefore, this study can be considered as representative for the graphene case. The study was performed on three kinds of graphene surfaces: a perfect flat surface, a disordered rough surface, and a surface with an ordered localized defect[14]. For all these surfaces, the formation of 3d clusters was found whose evolution in mean size $\overline{d}$ can be described by the power law: $\overline{d} \propto N^{z}$ for isolated clusters formation and $\overline{d} \propto N^{\alpha z}$ after clusters coalesce, whereby N is the incoming atom number, and z and αz are the growth exponent. A value in the range 0.75-0.87 has been reported for αz [152]. The perfect flat surface exhibited clusters with a rough surface, while the rough surface showed clusters with a flat surface. Moreover, the cluster density was increased, and the clusters size was reduced on the rough surface. The effects induced by the roughness has been found to be minimised by increasing the kinetic energies of the impinging Pd atoms. Such smoothing was not predicted for the surface with a localised defect [152].

Theoretical studies concerning transition metal deposition on metal supported graphene, specifically on Ru(0001), have been reported by Zhang *et al.* [153]. They found that, in general, cluster growth on metal supported graphene was regulated by two factors: the strength of the local sp^3 hybridization of graphene and the occupation of the outermost orbital. This means that on the fcc region of graphene/Ru(0001), characterised by strong

[14]The localised defect is made by a group of 60 C atoms displaced vertically by 0.2 nm above the flat graphene surface.

Table 2.1: DFT calculated values of the adsorption energy (E_{ads}), the ratio between the metal adsorption energy and its bulk cohesive energy ($E_{\mathrm{ads}}/E_{\mathrm{c}}$), the diffusion barrier (E_{diff}), and the charge transfer (q) for some transition metal. Values quoted from Ref. [86].

Adatom	Ads. site	E_{ads}(eV)	$E_{\mathrm{ads}}/E_{\mathrm{c}}$	E_{diff}(eV)	$q(e)$
Mn	H	0.1590	0.0545	0.0683	0.57
Fe	H	0.8980	0.2098	0.5841	1.49
Co	H	1.2257	0.2793	0.4151	0.97
Ni	H	1.5346	0.3456	0.2167	1.23
Pd	B	1.0756	0.2765	0.0417	0.64
Pt	B	1.5516	0.2657	0.1878	0.52
Eu	H	0.9975	0.5363	0.1285	0.81
Dy	H	1.5259	0.5019	0.1773	0.73

sp^3 hybridization, dispersed clusters of transition metals will grow if the adatoms have a partially filled d band, otherwise, large islands will be formed. Pd has been reported to have a binding energy to the fcc region of graphene/Ru(0001) of about 2 eV, and this value could be the limit between the growth of dispersed nanoclusters and islands.

Adsorption on free-standing graphene: experimental studies

Transition metal clusters (Ti, Cr, Pd, Ni, and Au) on free-standing graphene were studied by Zan *et al.* by means of atomic resolution high angle dark field imaging (HAADF) and a scanning mode TEM (STEM) operating at 60 kV acceleration voltage in UHV [30, 154]. For all deposited metals, the authors reported that the preferred nucleation sites are on hydrocarbon contaminations and that metals form clusters or nanocrystals. Although the acceleration voltage used for the STEM was 60 kV, which is well below 80 kV where knock-on damages on graphene are expected, damage was observed in the presence of some metals. In particular, Cr and Ti were found to etch graphene much more than Pd and Ni, while no damage was observed in the case of Au [30]. These experimental observations were supported by DFT calculations performed by Boukhvalov and Katsnelson [155] predicting that among Ni, Co, Fe and Au, only the first three metals reduce the energy necessary for vacancy defect formation on graphene. Thus, an electron beam energy below 80 keV would be sufficient to create vacancy defects in proximity to the transition metal clusters

mentioned above. Images of Au deposited on free-standing graphene showed clusters of 2-3 nm in diameter and their number increased with the coverage. At a nominal thickness greater than 1 nm the clusters began to coalesce keeping the density of clusters rather constant [154]. Au clusters coalescence was also observed after 50 s of exposure to a 60 keV electron beam [30]. The growth of Pd clusters was more similar to Au clusters than to Ti and Cr clusters, but unlike Au, it damaged the graphene. The beam-induced graphene etching due to transition metal clusters, along with the sample contamination, made it difficult to compare these TEM experiments with analogous STM and AFM studies on supported graphene.

Adsorption on SiC supported graphene

It is assumed that the interaction between graphene and the SiC substrate is weak, and therefore the substrate does not significantly influence the metal growth morphology [34]. Liu *et al.* [34, 65, 86] reported findings on several metals deposited on SiC supported graphene, highlighting different growth morphologies depending on the metal adatom–graphene and adatom–adatom interaction strengths. It was found that the cluster density dependence on the coverage followed classical nucleation theory for almost all metals evaporated on graphene/SiC [86,156] and that the island density attained a steady state at a coverage of about 5% [156]. The growth of Fe [156] and Co [157] clusters was an exception to this rule, showing an island density weakly dependent on the temperature and increasing continuously with the coverage. The explanation for this different behaviour lies in the lateral long-range repulsive interaction between Fe adsorbates, making the Fe adatom aggregation to a pre-existing cluster energetically less favourable as the coverage increases. At the same coverage, a similar cluster size was reported for Fe and Co, while sizes were smaller for Ni and larger for Mn. Mn was also the only metal not exhibiting a narrow distribution of island sizes. These different cluster features for different transition metals can be related to the values of the adsorption energies E_{ads} and the activation energy for diffusion E_{diff}. DFT calculations reported in Table 2.1 show that Mn has the lower E_{ads} among the above-mentioned metals and an extremely low E_{diff}. In contrast, Ni has a higher E_{ads} and a much higher E_{diff} than Mn (although E_{diff} is lower than for Fe and Co). Thus, compared to Ni, impinging Mn atoms are more likely to adsorb and to diffuse on graphene joining existing clusters.

Adsorption on metal-supported graphene

As previously mentioned in section 2.1.3, the lattice mismatch between graphene and a close-packed metal substrate can lead to the formation of a template (Moiré pattern) of energetically favoured adsorption sites. This property of metal supported graphene has been used to grow a regular array of well-defined size transition metal-nanoparticles on graphene/Ir(111) [92, 158, 159], graphene/Rh(111) [160, 161] and graphene/Ru(0001) [153, 162].

Graphene/Ir(111) It has been found that the Moiré pattern formed by graphene on Ir(111) allows for long-range ordered arrays of Pt, W, Re and Ir nanoclusters, with preferred nucleation sites at the Moiré-hcp areas[15] [92, 158, 159]. Ir clusters exhibited 2D growth at low coverages and transformed to 3D structures at high coverages [92,159]. The deposition of Pt, W, and Re gave rise to a superlattice of epitaxial clusters [158]. Fe and Au, because of their weak binding energy to the graphene across the Moiré cell, nucleated in unstructured large islands [158].

Graphene/Ru(0001) In contrast to transition metals deposited on graphene/Ir(111), most transition metals evaporated onto Ru(0001) supported graphene (Ru, Pt, Rh, and Pd) nucleate in the fcc regions [153, 162, 163], with the exception of Co which nucleates in both fcc and hcp regions [164]. For both graphene/Ru(0001) and graphene/Ir(111), the formation of highly dispersed transition metal clusters without preferential step edge decoration has been reported, although such clusters exhibited a different nucleation morphology, due to the different strength of the chemical bond between graphene and Ru and Ir metal substrates. The weak interaction between graphene and the Ir(111) system produces a strong interaction between the metal adatom and the graphene layer, while the stronger interaction between graphene and Ru(0001) results in a weaker interaction between the metal adatom and the graphene and thus, in higher adatom diffusivity [162]. The strong interaction between the Ru(0001) substrate and the graphene layer leads to a less ordered nanocluster array and to a transition from 2D seeds to 3D clusters growth at coverages lower than those on Ir supported graphene [162, 163]. The 3D growth at room temperature has been justified by the huge difference between the surface free energy of the graphene, equal to $46.7\,\mathrm{mJ/m^2}$, with respect to the surface free energy of transition

[15] The Moiré-hcp region corresponds to a region characterised by carbon hexagons located on the hcp sites of the Ir(111) substrate.

metals like Pt, Rh, Pd and Co, that is in the range of a few J/m^2 [162]. The low interaction energy between adatom metals and graphene with respect to the adatom-adatom interaction energy promotes the 3D growth. The growth morphology at the initial stage is strongly influenced by the competition between the strength of the carbon-metal bond and the metal cohesive energy. At a similar amount of deposited metal, Zhou *et al.* [162] found that Pt and Rh, which are characterised by a large metal-carbon dissociation energy, nucleate in small dispersed clusters; Pd and Co are characterised by small metal-carbon dissociation energies and the metal cohesive energy promotes nucleation in large 3D islands at an early growth stage[16]. In particular, Pd has exhibited clusters having an average diameter of $\sim$ 8 nm respectively $\sim$ 14 nm at coverages of 0.1 and 0.4 ML (in Figure 2.5a, the STM image acquired at 0.1 ML coverage has been reported) [162]. An exception is Au, which forms a film. Zhou *et al.* found an explanation to this observation in the weak interaction between Au and carbon atoms, and so the tendency to form 3D clusters, that is overcome by the tendency of Au to grow epitaxially on surfaces having a higher cohesive energy. Additional factors were identified in the strong interaction between Ru(0001) and graphene and in the nearest-neighbour Au distance amounting to 0.288 nm. This value is too large for Au to fit the graphene lattice (0.245 nm) but is small enough to fit the lattice of the Ru substrate (0.265 nm) [162]. The previous justifications for the observed cluster morphologies have been confirmed by *ab-initio* DFT studies reported by Zhang *et al.* [153] described in section 2.3.1.

Graphene/Rh(111) In the literature, only a few studies are dedicated to transition metal deposition on graphene/Rh(111). The interaction strength between the carbon layer and Rh(111) is between the weak graphene/Ir(111) and the strong graphene/Ru(0001) interaction. Sicot *et al.* studied Ni and Fe deposited on Rh(111) supported graphene. They found that Ni deposited on graphene/Rh(111) at room temperature forms flat triangular-shaped islands, whose edges align almost along the $\langle 1\bar{1}0\rangle$ directions of the Rh(111) substrate. Such islands have been found to be oriented in two different possible directions depending on the site (fcc or hcp) of the initial nucleation [160]. Fe nanoclusters, in contrast, have been found to be three-dimensional hemispherical-shaped and to nucleate preferentially at step edges [166]. The experimental work of Gotterbarm *et al.* [161] was devoted to the growth of Pd nanoclusters; unlike most of the previously mentioned exper-

[16]The metal-carbon dissociation energy for the mentioned metals are: 6.32 eV for Pt-C, 6.01 eV for Rh-C, 4.52 eV for Pd-C, and 3.60 eV for Co-C [165].

iments, the deposition occurred at 150 K. A regular array of flat islands was formed, with a cluster diameter similar to the dimensions of the Moiré unit cell (Figure 2.5b). In such islands, the morphology was modified to a more three-dimensional shape upon thermal annealing to 550 K.

Graphene/Cu(111) Pd cluster growth on Cu(111) supported graphene has been investigated by Soy *et al.* [167], depositing Pd in a continuous and stepwise mode. These authors found that the continuous mode gave rise to smaller three-dimensional clusters with respect to the stepwise mode. Moreover, the clusters grown in continuous mode were located on graphene terraces, and about the 80% of these clusters were characterised by a well-defined triangular shape with two main orientations (Figure 2.5c), similar to Sicot *et al.* findings about Ni deposited on graphene/Rh(111) [160]. The size of Pd clusters (7.8 nm at a coverage of 0.9 ML) was found to be larger than that of the Moiré unit cell, 2.0 nm in this work. These results have been explained in terms of a weak Pd–C interaction, which implies a high mobility of Pd atoms on the graphene surface at room temperature. Similar to the reports of Zhou *et al.* [162] for Pd on graphene/Ru(0001), no long-range order has been observed for Pd clusters on graphene/Cu(111). The authors also explained the absence of Pd in many of the Moiré unit cells with the high mobility of these adsorbates on graphene/Cu(111). The characteristic triangular shape of most of the clusters has been attributed to the anisotropy in diffusion around their corners and along their edges. The stepwise deposition showed round-shaped islands whose shapes began to transform into triangular-like shapes only at high coverages [167].

2.3.2 Transition metals on few-layer graphene

In this section, transition metals evaporated on few-layer graphene will be considered. Few-layer graphene is composed of n layers of graphene and is typically supported by an SiO_2/Si substrate. Both experimental and theoretical studies report a strong dependence of the formed cluster properties on the number of layers n [86, 168–172, 172, 173].

Zhou *et al.* [168] investigated the dependence of the Pd cluster morphology and charge transfer on the number of graphene layers. AFM measures performed at fixed Pd coverage showed that clusters became larger and the coarsening more pronounced for an increasing numbers of graphene layers (Figure 2.5d), up to 4 layers. The same trend was observed at different coverages, ranging from an equivalent thickness of 0.5 nm to 1.6 nm of Pd

deposited film. Further differences were not observed in Pd cluster morphology for few-layer graphene once thicker than 4 layers. The formation of Pd nanowires on the graphene layer edges was also reported. In this same work [168], the surface diffusion barrier E_n depending on the number of layers n was evaluated from the cluster density N applying the equation: $N \propto \exp(E_n/3k_BT)$, where k_B is the Boltzmann constant and T the absolute temperature. The observed larger density of Pd clusters on single layer graphene indicates that E_n is larger on single layer than on n-layer graphene. Raman spectroscopy studies revealed that Pd dopes graphene, with electrons transferred from Pd to graphene; moreover, the charge transfer decreases with the number of layers. The dependence of the cluster morphology and of the charge transfer on n indicates that different numbers of layers in the few-layer graphene lead to different interactions with Pd atoms.

The dependence of the nanocluster morphology on the number of layers was also reported for other transition metals [86, 169–172]; Au [169, 170, 172] in particular, has been widely studied.

For comparing these experimental results with theoretical calculations, simulations taking into account the interactions between graphene layers should be considered. As an example, Hardcastle *et al.* [173] performed DFT simulations including a GGA-type van der Waals correction[17] on multilayer graphene. A noticeable increase of the adsorption energy of Au, Cr, and Al adatoms with the number of graphene layers has been reported [173].

2.3.3 Transition metals on graphite

Transition metals on graphite typically nucleate and grow as compact 3D clusters [151, 174–176]. The reason for such growth is the low adsorption energy between the metals and graphite. The size, shape and distribution of the 3D clusters are strongly related to the deposition conditions. Thermal annealing induces cluster coarsening, which are characterised by a regular shape and a narrow size distribution of the formed islands. This section will focus on works reporting deposition performed at room temperature.

Morphology of transition-metal clusters grown on graphite

The features of 3D metal clusters grown on graphite depend strongly on the temperature of the substrate and on the coverage [174, 177]. Typically, at low coverages, small clusters have been observed to grow preferentially on graphite defects, while high coverages are

[17] The non-corrected GGA functionals do not correctly simulated interactions between graphene layers.

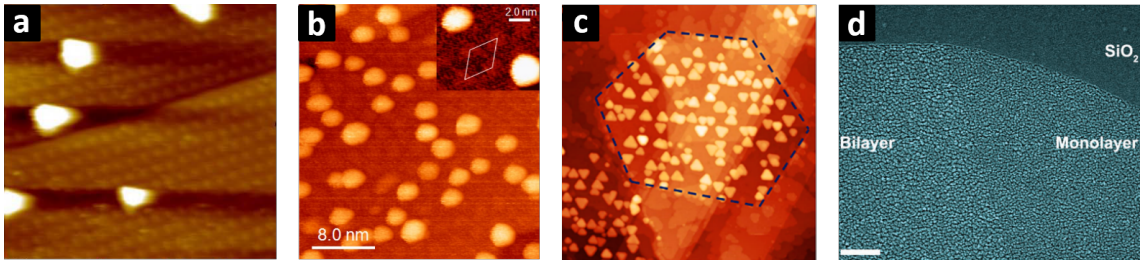

Figure 2.5: Transition metals adsorbed on supported graphene and FLG. (a) STM image (tunneling parameters: $V = 1.0\,\mathrm{V}$, $I = 0.1\,\mathrm{nA}$) of Pd clusters on graphene/Ru(0001) from the deposition of 0.1 ML of Pd. The field of view is 50 nm. Image adapted from Ref. [162]. (b) STM measurement (tunneling parameters: $V = 5\,\mathrm{mV}$, $I = 9\,\mathrm{pA}$) of Pd clusters on graphene/Rh(111) from the deposition of 0.3 ML of Pd. The white rhombus in the inset indicates the supercell of the Moiré pattern. Image adapted from Ref. [161]. (c) STM image of Pd clusters formed after the deposition of 0.9 ML of Pd on graphene/Cu(111). The blue dashed line outlines a hexagonal graphene island. The field of view is 355 nm. Image adapted from Ref. [167]. (d) AFM image of Pd on SiO_2 supported single layer and bilayer graphene. The amount of Pd deposited is equivalent to a 1.6 nm thick film. The scale bar corresponds to 200 nm. Image adapted from Ref. [168].

characterised by larger islands formed by aggregated clusters [151, 174–176]. The most commonly used experimental techniques for investigating cluster morphology are STM and AFM; the topographic images are often completed with spectroscopic and diffraction technique measurements. Because of the weak binding of metals on graphite, STM measurements are often influenced by the interaction between the tip and the clusters [151].

At a coverage below 3 ML of Pd evaporated onto graphite, the formation of small clusters with sizes ranging from 1 nm to 6 nm has been reported [174–176]. These clusters are located mainly at graphite surface defects, such as atomic steps and cleavages, resulting in a disordered surface morphology. The role of surface defects in metal nucleation on graphite will be addressed in the last part of this section. Coverages of $4 - 8$ ML exhibit clusters both at the surface defect sites and on the pristine graphite surface regions.

Whelan *et al.* [176] reported the formation of islands made up by the aggregation of a large number of 4.2 nm mean diameter clusters. The authors found that this diameter size is independent on the coverage. Similar islands made up of linked neighbour Pd clusters were also observed by Murakami *et al.* [175], but at the lower coverage of 1.7 ML. Murakami *et al.* performed AFM experiments in the tapping mode[18] and measured an aggregate diameter of 30 nm and a height of 6.5 nm. In experiments performed by Whelan *et al.* [176], high coverages of more than 50 ML appeared as a continuous granular metal film. The film was made up by randomly packed spherical clusters with a mean diameter of 4.2 nm and a diameter distribution ranging between 3 nm and 6.4 nm. Whelan *et al.* [176] observed a rather constant cluster size distribution from low to high coverages, but the degree of aggregation increased with the coverage. In general, the as-grown clusters were mainly round-shaped with a rather broad size distribution. After thermal annealing, clusters formed triangular and hexagonal shaped structures exhibiting a narrow size distribution [174, 177].

Adsorption energy and diffusion barrier

The calculated adsorption energies of Cr, Pt, Cu, Ag and Au on graphite are lower than the cohesive energies of these transition metals and higher than the calculated adsorption energies on graphene [86]. Following this observation, the adsorption energy of Pd on graphite corresponds to a value between the Pd adsorption energy on graphene $E_{\text{ads Pd/Gr}} = 1.06$

[18] The tapping mode helps to prevent surface modifications induced by the interaction of a scanning tip with clusters.

eV [34, 65, 86] and the Pd self-adsorption energy $E_{\mathrm{ads\,Pd/Pd}} = 2.87$ eV [151]. According to Hardcastle *et al.* [173] the van der Waals forces between the carbon layers are the reason for stronger metal adatom-graphite bond in comparison to the bond of a metal adatom to graphene. Typically, a metal adsorption energy on graphite smaller than the metal self-adsorption energy is an indication for 3D cluster growth, although some work reported dendritic growth of 2D clusters preceding 3D cluster growth [151].

The interaction between adsorbed metal atoms and the graphite surface may not be strong enough for the system not to get perturbed by a probing STM tip, causing changes in subsequent STM acquisitions. In fact, the tip may interact with the clusters, causing a displacement in their position during the scan (see, for example, Ref. [178]). Therefore, in STM experiments, distinguishing intrinsic dynamics from tip-induced dynamics on a graphite surface may be difficult.

As introduced above, the mechanism for metal cluster growth is driven by diffusion on the graphite surface and aggregation to clusters of adsorbed metal atoms. According to Appy *et al.* [151], the values of the activation energy for diffusion derived from experiments are rather different. Nevertheless, a trend can be identified: the activation energy for diffusion of a transition metal on graphite is typically higher for chemisorbed atoms (e.g. Pd, Pt, Ni and Fe) and lower for physisorbed metals (e.g. Au, Ag, Cu and Cr). Such energy is lower than the corresponding metal-on-metal activation energy for diffusion, but it can be higher or lower than the corresponding activation energy for diffusion on graphene [151]. The weak bond between metals and graphite also makes it possible to observe the diffusion of metal clusters on graphite surfaces, as observed experimentally by Bardotti *et al.* [179] for Au and Pt clusters.

The sticking coefficient

In some experimental studies on transition metals evaporated on graphite at 300 K, a sticking coefficient value of $S < 1$ [178, 180–182] has surprisingly been found instead of an S value close to unity, which is typical for other solid surfaces. As an example, Howells *et al.* [182] reported $S < 0.1$ for Pt on graphite. From a comparison between the reported results for S and the calculated residence time for Pt on graphite[19], Appy *et al.* [151]

[19] Appy *et al.* [151] calculated the Pt residence time on graphite at room temperature (300 K) with 10^{13} s^{-1} as the value for the pre-exponential factor for desorption, finding a residence time of 10^{24} s ($E_{\mathrm{ads\,Pt/Gr}} = 2.16$ eV). The experimental work of Howells *et al.* [182] reported a sticking coefficient $S < 0.1$. Adsorbates desorption, therefore, is not the only mechanism for $S < 1$, and the reflection of

suggested the reflection of impinging atoms on graphene as a possible mechanism for explaining the for $S < 1$ value. Arthur *et al.* [180] and Anton *et al.* [181] found instead an increase of the sticking coefficient for Cu and Au from below 0.05 at the beginning of the evaporation to about unity after 500 s of deposition at a flux of $\simeq 10^{12}$ atoms/cm^2 s. The increase of S with the deposition time has been interpreted as an enhanced probability for an adatom diffusing on the surface to be captured by the clusters already grown on graphite. The discrepancies for S among various experimental results were explained by Appy *et al.* [151] considering the incident energy of the impinging atoms that might not be properly dissipated by the graphene surface, with the number of coupled carbon layers playing a role in energy dissipation. This conclusion was supported by studies on metal adsorption on graphene, in which $S < 1$ has never been reported. To the best of my knowledge, there have been no reported experimental studies on S for Pd atoms evaporated on graphite; however, molecular dynamics simulations [152] can be found in the literature. In such a simulation technique, the equation of motion is solved for a set of atoms impinging on a potential energy surface. A Lennard-Jones potential has been used to describe the interaction between Pd and C atoms of graphene, while a tight binding potential has been used for the Pd-Pd interaction [152]. The value of S is given by the ratio between the number of Pd atoms getting stuck at the impact point and the total number of simulated atoms. For pristine graphite and graphite with localized defects, $S = 1$ has been reported, while S first slightly decreases and then increases to unity for graphite with atomically sized roughness [152].

Graphite surface defects and metal nucleation

Several groups have investigated the influence of carbon atom vacancies in graphite surfaces on transition metal cluster growth [182–184]. Since the density of natural defects on the HOPG surface is quite low, typically $1 - 5\,\mu\text{m}^{-2}$ [185], in these studies vacancy defects were created artificially by bombarding the HOPG surface with Ar^+ ions. This causes the number of clusters formed to increase and to be uniformly distributed on the defective surface with respect to the clusters formed on untreated HOPG. The surface vacancy defects act as a preferential nucleation sites, on which clusters are characterised by a rounder shape, narrow size distribution and higher stability to the STM tip interactions. At the same amount of evaporated metal, a higher amount of adsorbed metal atoms was

metal atoms should be considered.

reported for defective graphite than for pristine graphite, indicating a higher sticking coefficient. Yuan *et al.* [185] reported Pd nucleation only at defect sites for coverages below 0.25 ML. Above this value, Pd also nucleated on terraces. The clusters grown at defect sites increased in size with the coverage, with values ranging from 3.6 nm at 0.15–0.2 ML to 6.4 nm at 1 ML; simultaneously, the clusters shape changed from spherical to slightly elliptical or trapezoidal shape. No noticable change in the cluster density was observed. From the analysis of the photoemission spectra of Pd clusters grown on defects, Egelhoff *et al.* [183] found that for low coverages the adatom binding energy was higher than in the bulk metal, and it approached the value for bulk metal at coverages of several ML. In contrast, clusters grown on a defect-free graphite surface nucleate to large clusters and the binding energy among metal atoms in the cluster was comparable to that of the bulk metals.

In many experimental studies, transition metals have been found to decorate the step edges of graphite surfaces [176, 178, 185, 186]. In the specific case of Pd evaporated onto HOPG, Whelan *et al.* [176] reported the formation of 1 to 5 nm-wide clusters at low coverages (below 8 ML) at step edges and other defect sites. Similar results were found by Yuan *et al.* [185], who observed (for a coverage of 0.5 ML) step edges decorated by Pd nanoclusters. Such clusters were shown to be stable upon subsequent STM imaging. These results are consistent with the previously mentioned DFT studies performed by Hardcastle [173], who reported that the step edge binding energy was higher than binding on the terrace.

2.4 Transition Metal intercalation

Palladium deposited on graphene or on graphite does not exhibit intercalation at room temperature [151,177,188,189]. In the case of graphite, Pd GICs can be obtained only by reduction of the corresponding metal chloride ($PdCl_2$- GICs) as described, for example, in Ref. [190] and Ref. [191]. The literature contains work on Pd intercalation in supported graphene achieved upon thermal annealing at temperatures of several hundreds degrees Celsius [188,189]. The intercalation mechanism of Pd in Ru(0001) supported graphene was investigated by Huang *et al.* [188]. To promote the intercalation, the sample was annealed to 800 °C. STM images showed the formation of triangular-shaped intercalated islands exhibiting the same periodicity of the graphene/Ru(0001) Moiré pattern and an apparent

Table 2.2: Pd clusters morphology on graphene for several graphene substrates. θ is the coverage expressed in monolayers, T_{dep} is the substrate temperature during Pd deposition, d is the mean diameter of Pd clusters and h their thickness.

Substrate	θ(ML)	T_{dep}(K)	d(nm)	h(nm)	Shape	Ref.
Gr/Ru(0001)	0.1		~ 8			[162]
	0.4		~ 14			[162]
Gr/Rh(111)	0.3	150	3.0 ± 0.3	0.66 ± 0.10	Spherical.	[161]
Gr/Cu(111)	0.9	300	7.8 ± 1.1	1.2 - 1.6	Mainly well-defined triangular shape.	[167]
graphite (0001)		620	~ 4	> 1.5	Regular tetrahedron.	[187]
HOPG	4		~ 4		Spherical clusters irregularly packed in islands of 60 nm in diameter.	[176]
	8		~ 4		Spherical clusters arranged in flat islands of 100 to 200 nm in diameter.	[176]
	50		4 - 4.4		Densely packed spherical clusters.	[176]

height of 2.70 Å. Moreover, the graphene on the top of these islands showed a perfect lattice, without strains or defect due to the intercalation, suggesting quasi-free-standing graphene. This observation has demonstrated that Pd intercalation can be a route to overcome the strong interaction between graphene and the substrate. The distribution of the intercalated clusters was not related to the presence of defects [188]. This observation led to the hypothesis of the following intercalation mechanism, illustrated in Figure 2.6: the high temperature promotes the adatom-aided formation of an atomic defect, through which Pd can intercalate, followed by the self-healing of the C-C bonds. The annealing temperature is high enough to weaken the C-C bonds, which can break and bind with a Pd adatom, yielding an atomic scale defect and allowing the Pd atom to move on to the Ru(0001) substrate where it experiences a lower adsorption energy[20]. Since the Pd-Ru binding energy is higher than the Pd-C binding energy, the carbon atoms can re-establish their bond upon cooling down of the sample and the pristine graphene lattice is resumed.

Yagyu *et al.* [189] investigated Pd intercalation in a buffer layer, called by the authors "zero-layer graphene"[21] (ZLG), grown by thermal annealing on an SiC(0001) substrate. Pd evaporated at room temperature on the ZLG resulted in round-shaped clusters. For an evaporated amount corresponding to 0.8 ML, such clusters showed a diameter of 4-6 nm and a thickness of 0.5-0.8 nm. The intercalation was performed by means of thermal annealing at temperatures between 700 °C and 1100 °C. Evidence for intercalation was provided by the disappearance of the clusters and in the formation of several islands with a top surface 0.3 nm high, a value very close to the Pd interatomic distance in the bulk (0.28 nm). Therefore, just one Pd layer was intercalated. Moreover, the charge transfer after Pd intercalation occurred only between the intercalated Pd layer and the SiC substrate; no charge transfer with the graphene layer was detected by XPS measurements [189].

That intercalation proceeds only at high temperatures can be explained by the high energy barrier that a Pd atom must overcome for moving through the graphene layer: $E_{\text{barrier}} = 8.66$ eV for pristine graphene and $E_{\text{barrier}} = 3.83$ eV for defective graphene, as calculated by Huang *et al.* for free-standing graphene [188]. One of the possible routes to overcome E_{barrier} is through thermal annealing at high temperatures.

[20] The DFT calculated adsorption energy of a Pd atom amounts to -1.90 eV on graphene and to -4.52 eV on Ru(0001).

[21] In the thermal annealing technique, about 30% of the carbon atoms in the first grown graphene layer bond covalently with the SiC substrate. As this is not an ideal graphene layer, it is called 'zero-layer graphene' or 'buffer layer'. It can be decoupled completely from the substrate through intercalation, becoming an ideal graphene layer (see Ref. [189] and references therein).

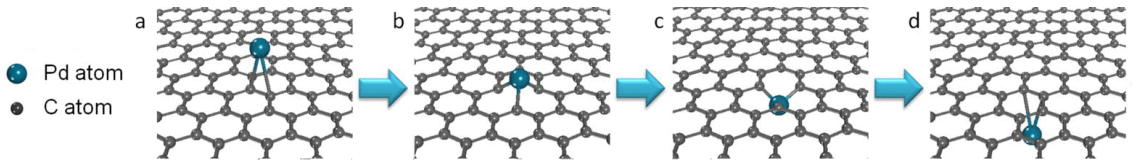

Figure 2.6: Scheme of the intercalation process of a Pd atom through a perfect graphene layer. (a) The Pd atom adsorbed on graphene. (b) At high temperature, the Pd atom bonds with carbon atoms, inducing a defect in graphene. (c) The defect allows the Pd atom to pass through and to bond with the substrate (not drawn). (d) The carbon atoms of graphene after re-binding. Adapted from Ref. [188].

Chapter 3

The LEEPS microscopy technique

This chapter is dedicated to the low-energy electron point source (LEEPS) microscopy. In the first part a short overview on in-line holography with low-energy electrons and its recent applications is presented. In the second part, the dedicated LEEPS microscope, developed at the University of Zurich for the studies of the alkali metal nucleation on free-standing graphene, will be introduced and described in detail.

3.1 In-line holography with low-energy electrons

In 1931, M. Knoll and E. Ruska [192] introduced the TEM concept, which has continuously been improved over the following decades. However, the resolution of such electron microscope was severely limited by the aberrations induced by the electron lenses available during the early times. In order to overcome these limitation, in 1948 D. Gabor formulated the famous "A new microscopic principle", proposing a lens-less microscope based on in-line electron holography [193, 194]. In this scheme no electrostatic lenses between the sample and the electron detector are necessary, resulting in a setup very similar to that of the shadow projection microscope, where a divergent electron beam projects the magnified image of a conductive sample onto the far detector. In addition, in the Gabor' scheme the holography patterns formed by the electrons on the detector provide access to the phase of the object wave, which is typically not available in other electron microscopy techniques. As in a projection microscope, the magnification is given by the ratio::

$$M = \frac{D}{d}\,, \tag{3.1}$$

where D is the distance between the point focus of the divergent electron beam and the detector, and d is the distance between the point focus and the sample.

3.1.1 The holographic principle

The fundamental requirement in the Gabor's proposal is the coherence of the emitted electron beam. The sample is placed at a short distance in front of the point focus, and it is smaller than the area in the object plane illuminated by the electron beam. Part of the electrons emitted from the source elastically scatter off the sample giving rise to the object wave Ψ_{o}. The unscattered fraction of the emitted electron beam, the reference wave Ψ_{r}, will interfere with Ψ_{o} at the detector plane where the interference pattern is produced, as shown in Figure 3.1. The intensity at the detector is given by the squared module of the superposition of Ψ_{r} and Ψ_{o}:

$$\begin{aligned} H(X,Y) &= |\Psi_{\mathrm{r}}(X,Y) + \Psi_{\mathrm{o}}(X,Y)|^2 = \\ &= |\Psi_{\mathrm{r}}(X,Y)|^2 + |\Psi_{\mathrm{o}}(X,Y)|^2 + \Psi_{\mathrm{r}}(X,Y)\Psi_{\mathrm{o}}^*(X,Y) + \Psi_{\mathrm{r}}^*(X,Y)\Psi_{\mathrm{o}}(X,Y)\,, \end{aligned} \tag{3.2}$$

where (X,Y) denotes the coordinates in the detector plane. The first term is the coherent background due to the reference wave, that is known and can be subtracted, while the second term is assumed to be small and can be neglected. The last two terms represent the interference pattern and contain the information on the amplitude and phase of the scattered object wave.

The hologram can numerically be reconstructed. First, the hologram H(X,Y) is multiplied by a simulated reference wave; then, using the Huygens principle and the Fresnel formalism, the object wave is calculated in planes back-propagating from the detector position towards the source [195]. The reconstruction will appear in focus at a position equal to the experimental source-to-sample distance. The hologram reconstructions presented in chapter 4 have been performed using the algorithm published in Ref. [196].

In the last two terms of Equation 3.2 both the object wave and its complex conjugate contribute equally to the interference pattern, giving rise to the so called twin image effect, which is an intrinsic side effect exhibited by any in-line holographic scheme. Because of

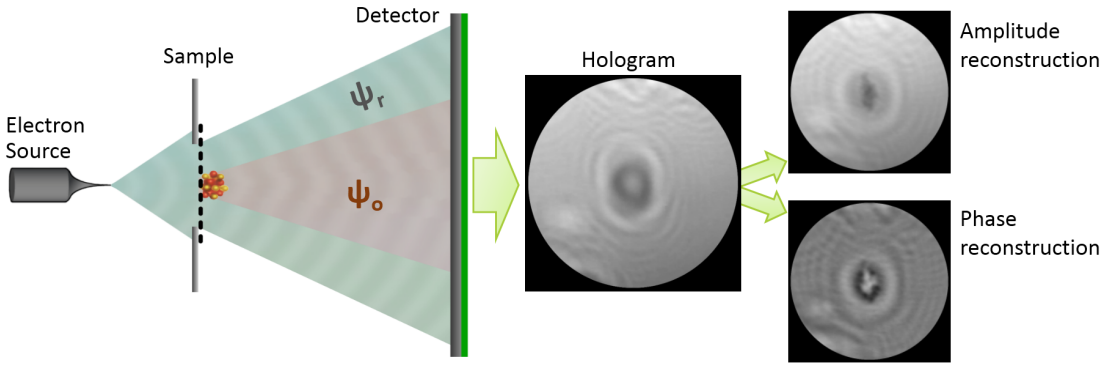

Figure 3.1: The principle of in-line holography with low-energy electrons. A divergent beam of coherent electrons impinges on the suspended sample. A fraction of the incident beam elastically scatted off the sample (object wave Ψ_o) interferes with the fraction of the beam not scattered by the object (reference wave Ψ_r), producing an interference pattern (hologram) on the detector. Amplitude and the phase of the object wave can be retrieved through the hologram reconstruction process.

the presence of the twin image, the resulting reconstruction would be a sum of the focused image with the out-of-focus twin image [193].

3.1.2 Holography with low-energy electrons

The holographic technique, together with the use of a beam of low-energy electrons, offers several advantages with respect to conventional electron microscopes. Low-atomic-number materials have higher scattering amplitude for low-energy electrons and as a consequence, the resulting images will exhibit a high contrast. Moreover, the energies involved are low enough not to damage organic and biological materials, as for example DNA [197–199]. Electrons with energies in the range of 30-250 eV exhibit a velocity of the order of 10^6 m/s; thus, low-energy electrons are slow enough for their trajectories to be perturbed by very small electric and magnetic fields. As an example, holography with low-energy electrons has been used to detect fractions of elementary charges [61].

A divergent coherent electron beam can be efficiently produced by using ultra-sharp nanotips, exhibiting one or few atoms on the apex, called electron point-sources (EPSs) [200–202]. The introduction of EPSs has represented a significant contribution to the development of low-energy electron holography, as they provide a directly coherent divergent beam avoiding using lenses to shape the beam.

The electron source

An EPS is usually produced by shaping the tip of a thin tungsten wire with crystallographic orientation (111), as detailed in section 3.2.1. Field emission from W(111), characterized by a work function of 4.47 eV [203], occurs for fields above 0.3 V/Å. In proximity of the apex of a negatively biased ultra-sharp nanotip, the electric field is sufficiently high to reduce and narrow the barrier at the metal-vacuum interface for electrons to have a high probability to tunnel into the vacuum as described by the Fowler-Nordheim equation [204]: $J = (1.5 \times 10^{-6}/\phi)F^2 \exp(-6.44 \times 10^9 \phi^{3/2}/F)$, that relates the emission current density J to the local electric field F on the cathode tip and to the work function ϕ [205]. This feature allows for electron field emission at low bias voltages, typically ranging from -20 V to -250 V with an emitted current of 0.5-100 nA. Since the sample serves as the anode for the field-emission EPS, the emission properties depend also on the distance d between the tip and the sample through the term F: $F = \beta V/d$, with V being the applied voltage and β being the field enhancement factor that accounts for the geometry of the tip (see e.g. Ref. [206]). Electrons are mainly emitted one at a time by the EPS and, thus, effects arising from the Coulomb repulsion among emitted electrons are avoided. The emission is not isotropic, but it occurs in forward direction within a narrow cone, resulting in a divergent electron beam. This limited divergence angle of the electron trajectories is due to the rapid decrease of the electric field at the apex already at a polar angle of few degrees from the tip axis [207, 208]. Because of the strong dependence of J on F, the electron emission is concentrated at the apex of the EPS. In addition, the radial intensity distribution of the emitted electrons approximately follows a Gaussian distribution [209–211]. Although in routine LEEPS measurements not always a tip ending with one apical atom is used, the radius of curvature of the tip is typically small enough to emit electrons with trajectories (at a large distance from the tip surface) that, with a high degree of accuracy, can be considered as originating from the surface of a smaller virtual sphere. This effect is due to the spherically distributed potential next to the tip apex and the radius of the virtual sphere defines the virtual source size. The shape of the tip, together with the applied voltage and its distance from the sample, influences the electron current emitted and thus the brightness of the beam, while the spatial coherence of the electron beam is mostly influenced by the size of the virtual source.

The coherence of an electron beam is defined both in terms of temporal and spatial coherence. The temporal coherence refers to the longitudinal coherence length L_t on the

propagation direction of the beam, and is limited by the energy spread of the emitted electrons:

$$L_{\mathrm{t}} = \frac{\lambda^2}{\Delta\lambda} = \frac{2U}{\Delta U}\lambda\,, \tag{3.3}$$

where λ is the electron wavelength and U is the electron energy. For a field emission source, the decaying tunnelling probability below the Fermi level ensures the low energy spread of the emitted electron ensemble, with typical values of $\Delta U \sim 250\,\mathrm{meV}$ for a W(111) source [204, 212]. The spatial coherence, instead, denotes the coherence in the plane perpendicular to the propagation direction of the beam and is limited by the finite spatial extent of the virtual source. The spatial coherence length L_{s} depends on the source size through the Van Cittert-Zernike theorem [213]:

$$L_{\mathrm{s}} = \frac{\lambda d}{\pi r_{\mathrm{eff}}}\,, \tag{3.4}$$

where r_{eff} is the effective source size and d is the distance between the electron source and the sample. An upper limit to the virtual source size can experimentally be estimated from the coherence area at the image plane $A_{\mathrm{s}} = \pi(M\,L_{\mathrm{s}})^2$, where M is the magnification defined in equation 3.1, through the equation 3.4:

$$r_{\mathrm{eff}} = \frac{\lambda d M}{\sqrt{\pi A_{\mathrm{s}}}}\,. \tag{3.5}$$

Typical experimental values of r_{eff} for electrons in the range $60 - 300\,\mathrm{eV}$ are of a few Angstroms; since the electrons are emitted from a volume of atomic dimensions, these tips can effectively be considered as point-sources [202, 213–215]. Some values reported in the literature are $r_{\mathrm{eff}} = 1.7$ Å in Ref. [62] and $r_{\mathrm{eff}} = 1.6$ Å in Ref. [214].

The mean experimental brightness of an electron source B is defined as the current density J per unit solid angle Ω. According to the derivation reported in Ref. [216], B can be determined from the coherence area A_{s}, the current density J, and the wavelength λ through:

$$B = \frac{2JA_{\mathrm{s}}}{\lambda^2}\,. \tag{3.6}$$

As an example, the average brightness reported in Ref. [217] for a single-atom terminated nanotip is $B = 3.3 \times 10^8\,\mathrm{A/(cm^2 \cdot sr)}$ at an emission voltage of 470 V.

Resolution

In in-line holography, the fundamental resolution limit is related to the radiation wavelength and the numerical aperture of the microscope through the Abbe diffraction limit: $R_{\mathrm{Abbe}} = \lambda/(2N.A.)$. However, it should be noted that in a real low-energy electron point source setup the resolution can be limited by several external factors, such as the occurrence of mechanical vibrations and the coherence of the emitted electron beam [216, 218]. Mechanical vibrations lead to a relative displacement of the electron source Δs with respect to the sample that induces a shift of the hologram by $\Delta S = M\Delta s$. Hence, the acquired hologram will be the superposition of all these shifted holograms generated during the integration time of the image readout system, resulting thus in a blurred image with degraded interference fringes. From equation 3.5, the effective source size r_{eff} is inversely proportional to the coherence area at the image plane A_{s}; being the width of the interference fringes band affected by the above mentioned factors, A_{s} gives an underestimate of the spatial coherence and from equation 3.5 an upper value of the virtual source size is calculated. The resolution is proportional to r_{eff}, that in turn can be considered the instrumental resolution [216]. For an acquired hologram, the resolution is estimated from the highest frequency in the Fourier spectrum of the hologram [219]. Defining k_{max} as the maximum frequency in the hologram spectrum, the resolution is given by [219]:

$$R = \frac{2\pi}{k_{\mathrm{max}}}\,. \tag{3.7}$$

The value of k_{max} is given by the product of the pixel value (from the centre of the spectrum) at which the highest frequency is observed, A, and the pixel size in the Fourier domain, Δ_{F}. Being $\Delta_{\mathrm{F}} = S_{\mathrm{obj}}^{-1}$, where $S_{\mathrm{obj}} \times S_{\mathrm{obj}}$ is the object area size, and being $S_{\mathrm{obj}} = S_{\mathrm{det}}/M$, where $S_{\mathrm{det}} \times S_{\mathrm{det}}$ is the detector area, k_{max} can be written as: $k_{\mathrm{max}} = \dfrac{A\,M}{S_{\mathrm{det}}}$.

3.1.3 Graphene as support slide

One of the requirements for in-line holography is that an appreciable fraction of the impinging electron beam should be transmitted unscattered toward the detector. The object,

thus, should be small enough to block only a minor fraction of the beam[1]. Typically, in low-energy electron holography, the sample is stretched on a holey or lacey carbon membrane (see, e.g., Ref. [197] for DNA samples and Ref. [220] for carbon nanotube samples) or protrudes from an edge (see, e.g., Ref. [221]). The drawback for these kinds of samples is the presence of the so-called "biprism effect"[2] in the hologram, that can make the interpretation of the reconstructed distributions extremely difficult [223].

Graphene has shown to be a very suitable substrate for LEEPS investigations. It is an atomically thin membrane[3] exhibiting a high conductivity and transparency even to low-energy electrons. Moreover, it acts as a grounded plate avoiding, thus, the biprism effect [62]. Graphene transparency to low-energy electrons can find applications not only in LEEPS microscopy [62, 63] but also in electronics, for example as gate material in a vacuum triode setup [224].

The transparency is defined as $T = I_\mathrm{t}/I_0$, where I_t is the intensity of the transmitted beam and I_0 is the intensity of the incident beam. In table 3.1 the transparency values of single layer and bilayer graphene to low-energy electrons reported in the literature are summarised. The attenuation of the incident beam intensity can be described in terms of the effective attenuation length l_EAL:

$$I_\mathrm{t}(h) = I_0 \exp(-h/l_\mathrm{EAL})\,, \tag{3.8}$$

where h is the thickness of the material. Using a value of $l_\mathrm{EAL} \approx 5\,\text{Å}$ for an electron beam energy of 100 eV [225], from the equation 3.8 Mutus *et al.* calculated a value of $h = 1.46\,\text{Å}$ for graphene [62]. The authors pointed out that this result is different from the expected graphite interlayer distance (3.35 Å) and, instead, corresponds to twice the sp^2-bonded carbon covalent radius [62].

[1] This requirement is necessary to neglect the term $|\Psi_\mathrm{o}(X,Y)|^2$ in equation 3.2.

[2] This name is related to the electron biprism, i.e. a thin positively charged wire, splitting the electron beam and leading to equidistant interference fringes [222]. The resulting interference pattern can be described as that of two overlapping wavefronts originating from two coherent virtual point sources shifted sideways at $+d$ and $-d$ from the real source. In LEEPS microscopy, the voltage difference between the tip and the sample results in a potential gradient around the elongated sample. The emitted electron trajectories are distorted by such potential gradient on both sides of the elongated object, which behaves like a positively charged wire.

[3] Low-energy electrons are characterised by a short penetration depth in materials. Therefore, a substrate thin enough to be transparent to low-energy electrons is necessary, allowing for imaging the sample deposited on it.

Table 3.1: Transparency values of single layer T(SLG) and bilayer graphene T(BLG) with respect to the electron beam energy E as found in the literature. Both measurements and simulations show that graphene is transparent to low-energy electrons and the transparency increases with the energy of the incident electron beam.

E[eV]	T(SLG)	Method	Reference
2 - 40	$\sim$ 0.6	Vacuum triode setup	[224]
20 - 200	0.05 - 0.95	Simulations in a time-dependent framework	[226]
66	0.73	LEEPS	[63]
100	0.74	LEEPS	[62]
300	0.6	PES	[227]
2 - 300	0.02 - 1.05[a]	Ultralow-energy STEM	[228]
60 - 300	0.68 - 1.2[a]	Time-dependent DFT	[229]
250	0.88 ± 0.01	LEEPS	This thesis work
E[eV]	T(BLG)	Method	Reference
66	0.46	LEEPS	[63]
2 - 300	0.03 - 1.05[a]	Ultralow energy STEM	[228]
60 - 300	0.50 - 1.5[a] AB stacking 0.67 - 1.5[a] AA stacking	Time-dependent DFT	[229]

[a] According to the authors of Ref. [228] and Ref. [229], the values T(SLG) > 1 and T(BLG) > 1 are due to the contribution of secondary electrons caused by high energy impinging electrons. In the experimental study reported in Ref. [228], secondary electrons are emitted from the sample and accelerated towards the detector together with the transmitted electrons. In the time-dependent DFT study (Ref. [229]), the formation of secondary electrons is accounted for by the computational framework used for the simulations.

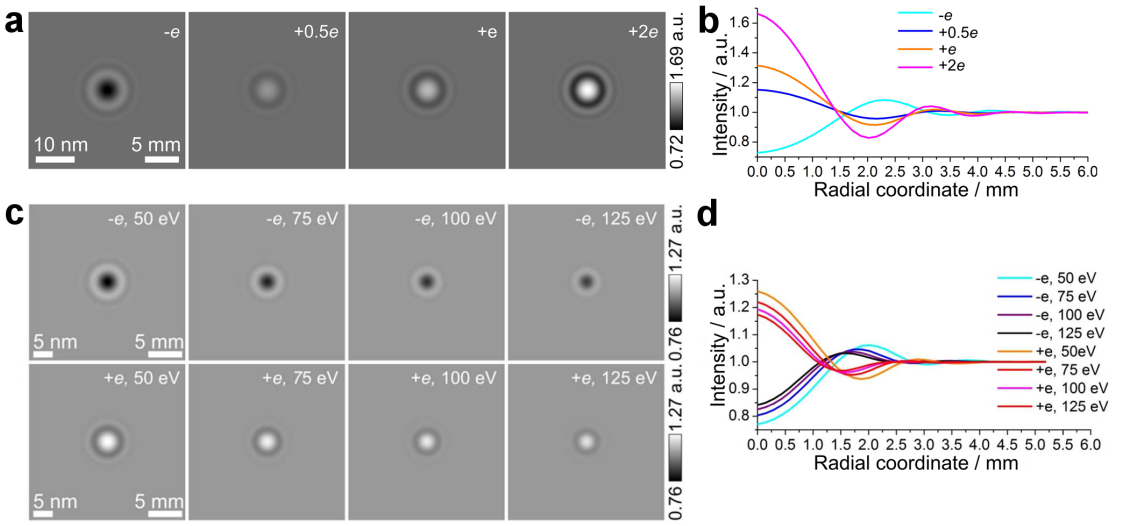

Figure 3.2: (a) Simulated holograms for a point-like charge at $-e$, $+0.5e$, $+e$, and $+2e$ charge value and (b) the corresponding radial intensity profiles published in [61]. The energy of the electron beam used for simulations is 30 eV with a distance between the electron source and the sample $d_{\mathrm{tip-sample}} = 82\,\mathrm{nm}$ and a distance between the electron source and the detector $d_{\mathrm{tip-detector}} = 47\,\mathrm{mm}$. (c) Simulated holograms for $-e$ charge (upper row) and $+e$ charge (lower row) for energies in the range $50 - 125\,\mathrm{eV}$ and (d) the corresponding radial intensity profiles. The scale bar on the left and the right side of simulated holograms refers to the size in the object plane and the detector plane, respectively. Image adapted from Ref. [61].

3.1.4 Direct observation of charges

Recently, it has been demonstrated that it is possible to observe charged adsorbates on free-standing graphene and their dynamics with LEEPS microscopy [61]. These adsorbates, if neutral, would have a too weak contrast to be distinguished from the noise.

The simulations of point charges show that a negative charge produces a dark spot on the detector, while a positive charge produces a bright spot with an intensity proportional to the amount of charge (Figure 3.2a and 3.2b) [61]. As the energy of the probing electrons increases, the intensity of the bright spots and the radial coordinate of the first minimum decrease (Figure 3.2c and 3.2d) [61].

For a localised charged object the ordinary reconstruction routine does not converge to meaningful result. The reference wave is altered by the potential of the object, making it impossible to distinguish a term related to the reference wave and a term associated

with the object wave, as required for an ordinary reconstruction routine. However, it has been demonstrated that it is possible to recover the projected potential of a charged adsorbate through an iterative phase retrieval reconstruction algorithm [218]. The phase shift distribution obtained from the reconstruction is linearly related to the projected potential V_{proj}:

$$\Delta\varphi = \varphi_{obj} - \varphi_{vac} \approx 2\pi \frac{e}{hv} V_{\mathrm{proj}} \,,$$

where φ_{obj} and φ_{vac} are the phases of the exit wave in presence and absence of the object, respectively, calculated through the eikonal equation; e is the elementary charge, h is the Plank constant and v is the speed of the probing electrons. The projected potential is given by the electrostatic potential of the object V causing the phase shift integrated over the paths of the probing electrons $V_{\mathrm{proj}} = \int_{path} V \,\mathrm{d}s$. The retrieved phase shows a constant value within the area of the adsorbate and decays outside. If compared with a Coulomb potential ($\sim 1/r$), the projected potential reconstructed from experimental data shows a slower decay. The reason for this discrepancy might be the free point-like charge model used in the simulations, that do not consider the charge redistribution in graphene upon adsorption [218].

The exact knowledge of the chemical origin of an adsorbate, together with the information on the potential distribution provided by LEEPS microscopy, can provide further insight into the adsorption properties on free-standing graphene, so far investigated mainly by DFT calculations.

3.2 The LEEPS microscope

A Low-Energy Electron Point Source microscope is a lens-less setup composed mainly of an electron point source, emitting a divergent coherent beam of low-energy electrons, the sample and the detector (Figure 3.3a). On the experience of the previous microscopes, we have designed and built a new LEEPS microscope dedicated to the in situ investigation of metal nucleation on free-standing graphene. The new microscope has been operational since July 2015.

3.2.1 Design of the microscope

The optical bench of this microscope, where tip and sample are positioned, is suspended from a fixed frame attached to the vacuum flange. The frame hosts tools such as the

evaporation unit, the heater and the sample storage (Figure 3.3b). The relative position of the electron source with respect to the the sample is controlled by four piezo-electric inertial nanopositioners. The tip tower and the sample tower are depicted and described in Figure 3.4.

One additional feature in this new LEEPS microcope is the possibility for a fast exchange of the tip from the load-lock (Figure 3.3c) without a need to vent the main chamber. Further improvements are related to the vacuum conditions and to the mechanical stability. A mechanical wobble-stick permits to move the sample inside the chamber and to operate on the evaporator unit for selecting one out of the four available evaporators.

The resolution of the LEEPS microscope, as described in section 3.1.2 can be estimated from the number of visible interference fringes. As mechanical vibrations are one of the primary sources of fringe degradation, special care was taken to damp the microscope properly. The optical bench is suspended by mean of O-rings made up of Viton (see inset of Figure 3.4), a material that is well known for its high internal damping [230]. All wires coming from the optical bench are clamped in Viton cylinders and fixed into slots, both on the optical bench and on the frame, attenuating mechanical vibrations transmitted through cables (Figure 3.4). The whole microscope is further damped through an active damping pneumatic system placed on a concrete platform.

The field emitter is shaped from a $\sim 4\,\mathrm{mm}$ long and 0.1 mm thick single-crystal tungsten wire with (111) crystallographic orientation spot welded on a molybdenum hairpin for resistive heating in vacuum. The tip is prepared by electrochemical etching in a 20% sodium hydroxide (NaOH) solution. During the procedure, the tungsten is removed at the meniscus of the solution with an etching rate faster at the bottom of the meniscus than at the top, resulting in a cusp-shaped tip with an apex radius of $20 - 50\,\mathrm{nm}$. Then, the tip is transferred inside the main chamber of the microscope where is cleaned by ohmic heating and further sharpened by neon ion sputtering following the procedure proposed by Janssen and Jones [231]. High-purity neon is inserted into the main chamber to a pressure of about $5 \times 10^{-4}\,\mathrm{mbar}$. The tip is negatively biased to a high enough voltage (typically of $\sim 2\,\mathrm{kV}$) so that a constant field emission current of $20\,\mu\mathrm{A}$ is reached. Neon ions are formed by collision with the field-emitted electrons and are accelerated towards the tip, sputtering the shanks of the apex and decreasing the tip radius. A more detailed description of the tip preparation procedure can be found in Ref. [232].

As described in section 3.1, the magnification of the image is related to the source-to-

sample distance, which can not be measured directly in this LEEPS microscope. However, it can be estimated from the calibration of the lateral shift of the positioner labeled with T in Figure 3.4. The shift Δx of the tip causes a lateral displacement ΔX of the image on the screen, therefore from geometry $d_{\mathrm{tip-sample}} = d_{\mathrm{tip-detector}}\,\Delta x/\Delta X$. A more accurate determination of such distance is obtained from the subsequent reconstruction of the hologram.

The detector is made up by a 75 mm diameter high-resolution single stage micro-channel plate (MCP) followed by a phosphor screen. The distance source-to-detector is 158 mm, allowing a magnification of 3×10^5 for a source-to-sample distance of 500 nm. The numerical aperture of the microscope is N.A. = 0.23 with an intrinsic resolution of $R_{\mathrm{Abbe}} = 2.7$ Å for electrons with an energy of 100 eV.

The hologram on the phosphor screen is acquired by a digital camera not mechanically connected to the microscope. We use the on-the-shelf camera Canon 5D mark II equipped with a macro lens. The linearity of the CMOS sensor, as well as the noise level, have been tested in an optical setup with a neutral density filter and results have been compared to the output of a Hamamatsu Orca II C4742-95 camera. The camera response showed to be linear for ISOs integer multiples of 160, the native ISO for this camera. The Canon sensor can acquire images with 14-bit dynamic range and 5616 × 3744 pixels of resolution. In the movie mode, a frame rate of 25 fps in jpeg compression at a resolution of 1920 × 1088 pixels is reached. The conversion from the Canon proprietary RAW format (.CR2) to TIFF format has been performed with the software *dcraw* [233].

3.2.2 The evaporator unit

The presence of evaporators inside the microscope allows for in situ investigations of clusters growth. They are mounted inside a dedicated evaporator unit, composed mainly of an inner body and a helmet, as shown in Figure 3.5. The inner body is a rotating support designed to host up to 4 evaporators and allows for a well controlled positioning and provides the electrical connections. The evaporators are separated by stainless steel lateral shields to avoid contaminations from the surrounding dispensers. The rotating helmet provides reduction of the vapour beam section[4] and the shielding of the evaporator in use during the activation and the cleaning phase. Moreover, the opening on the back

[4]The cylinder confines the metal vapour only to the sample area. This is important to avoid depositing metals on Macor parts, that would compromise their electrical insulation.

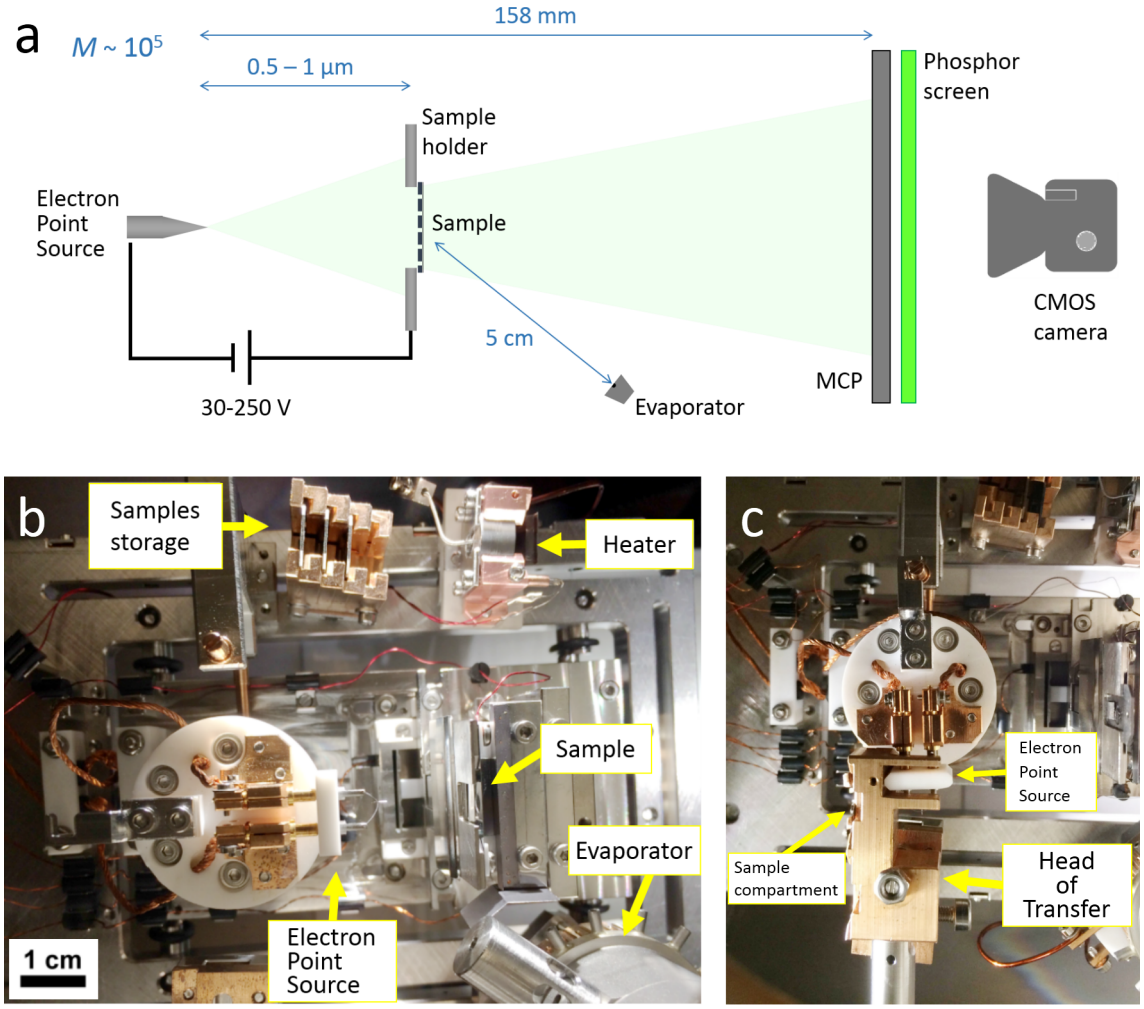

Figure 3.3: (a) Scheme of the LEEPS microscope. The electron source is a ultrasharp W ⟨111⟩ tip. The sample, graphene suspended on a perforated SiN membrane, is at distances in the range of $0.5-1\,\mu$m from the tip. The detector (Photek VID175) is placed at 158 mm from the tip and is made up of a single-stage micro-channel plate (MCP), with a channel diameter of $10\,\mu$m, and a phosphor screen. The image formed on the phosphor screen is acquired by a Canon 5D Mark II camera. (b) Top view of the LEEPS frame and optical bench. (c) Tip exchange. The newly designed transfer head allows for transferring both, samples and tips.

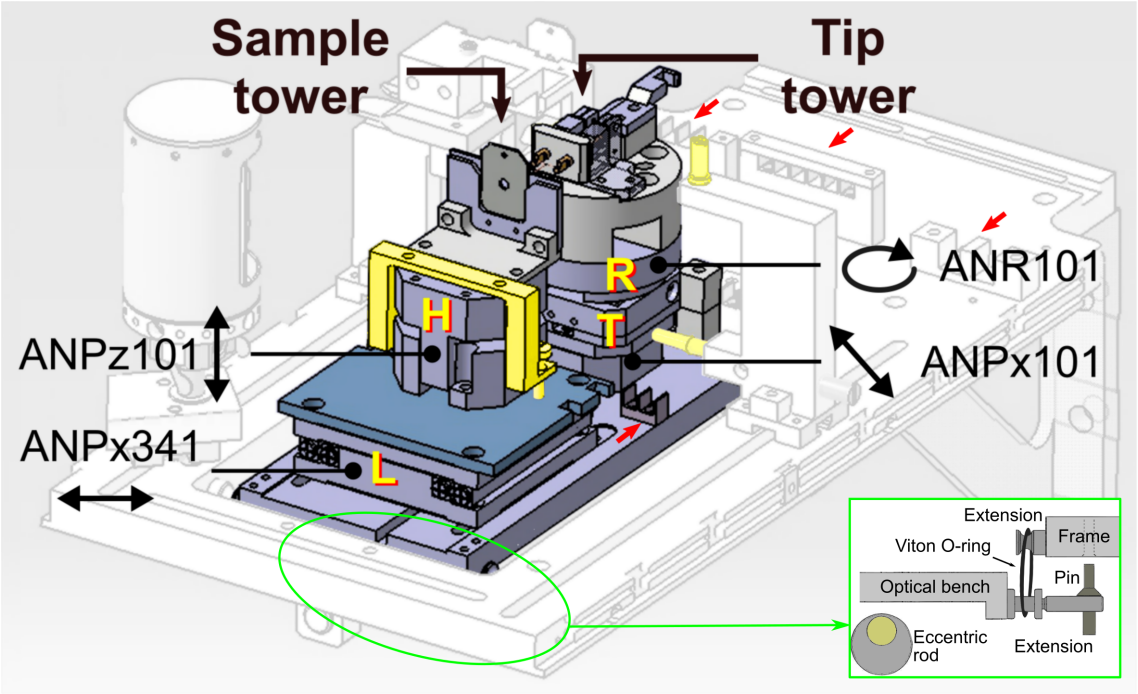

Figure 3.4: Technical drawing of the optical bench. The tip tower consists of a translational nanopositioner and a rotational nanopositioner, which allows rotating the upper part to exchange the tip. Moreover, it allows to partially adjust the beam direction along the optical axes. The sample tower consists of a lower nanopositioner, regulating the distance tip-to-sample, and a vertical upper nanopositioner. The motion is depicted by the arrows close to their notations. All nanopositioners used are open-loop piezoelectric made by non-magnetic and UHV compatible components manufactured by Attocube. These are based on a "stick-slip" motion technology for the stepping mode movements. The red arrows indicate the slots in which cables are clamped in Viton cylinders, damping mechanical vibrations transmitted through wires. The optical bench is suspended from the surrounding frame by Viton O-rings through extensions, sketched in the inset. The optical bench extensions have an additional pin to keep the stage locked to the frame when the stage is lifted up by mean of an eccentric rod; this is necessary to insert or remove the sample and the tip. A system of stoppers, marked in yellow in the drawing, helps to prevent force applied to nanopositioners during these operations.

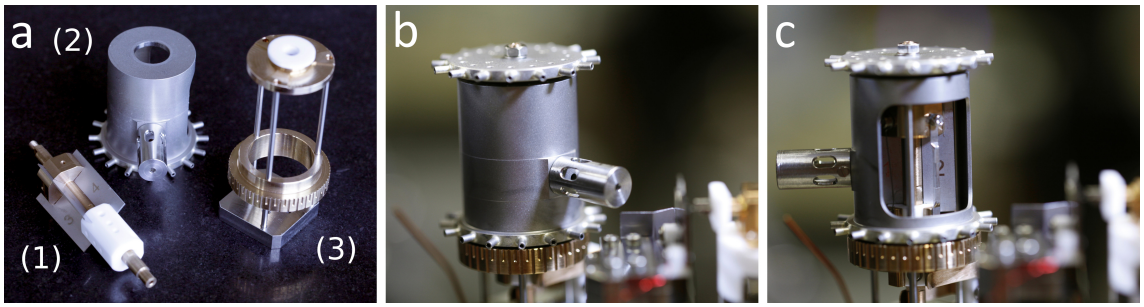

Figure 3.5: The evaporator unit. (a) Elements composing the evaporator unit: (1) the inner body, on which the AMDs are mounted, (2) the helmet, and (3) the supporting frame. (b, c) The evaporator unit inside the LEEPS microscope. In picture (b) the helmet is in the firing position. In picture (c) the helmet is rotated showing the evaporator in use. The number on the helmet top and the lateral shields allows for identifying the evaporator in use. Evaporators are placed at 5 cm from the sample. The inner body as well as the helmet can be rotated by means of the wobble-stick through the upper and the lower gear respectively. The helmet has a diameter of 3 cm and a height of 4 cm. The metal vapour leaks out of a 2 mm diameter nozzle.

side is wide enough for the visual inspection of the evaporator.

The alkali metal sources used are the commercially available Alkali Metal Dispensers (AMD) manufactured by SAES Getters [234]. These dispensers consist of a mixture of alkali-metal chromate salt ($MeCrO_4$, where Me is the alkali metal) and a reducing agent (the Zr-Al alloy St 101) contained in a nichrome boat with defined geometry (Figure 3.6). The purpose of the reducing agent is twofold: it acts as reducing agent for the salt, and it acts as getter irreversibly sorbing chemically active gases formed during the reduction reaction. The reduction reaction between the salt and the reducing agent is activated by ohmic heating the dispenser and can be written as:

$$\mathrm{Me_2{}^{+1}Cr^{+6}O_4} + \tfrac{5}{4}\,\mathrm{Zr^0} \longrightarrow 2\,\mathrm{Me^0} + \tfrac{5}{4}\,\mathrm{Zr^{+4}O_2} + \tfrac{1}{2}\,\mathrm{Cr_2{}^{+3}O_3}$$
$$\mathrm{Me_2{}^{+1}Cr^{+6}O_4} + \tfrac{5}{3}\,\mathrm{Al^0} \longrightarrow 2\,\mathrm{Me^0} + \tfrac{5}{6}\,\mathrm{Al_2{}^{+3}O_3} + \tfrac{1}{2}\,\mathrm{Cr_2{}^{+3}O_3}$$

The released reaction gases are mainly CO, CO_2 and H_2 [235], but but a small amount of released H_2O and O_2 has also been observed [236]. The partial pressures of such gases reach a maximum at a dispenser current of about 4 A. For currents higher than 5 A, corresponding to temperatures above 650 °C, the St 101 alloy regenerates continuously, efficiently pumping the reaction gases. Under those conditions, the getter reduces drastically

the partial pressures of CO and CO_2, but not that of H_2 [235].

A proper outgassing of the dispenser is crucial for the release of a clean alkali vapour. After the first degassing, the evaporator in use is continuously powered with 3 A current as suggested in Ref. [237]. In this state the dispenser will not readsorb gases from the chamber. Before each use, evaporators are powered at 5 A for a few minutes. This procedure is necessary to regenerate the getter St 101 alloy that could otherwise be saturated [238].

The overall design of the evaporator provides a rather uniform and well-defined temperature for a given current, allowing for a controllable and reproducible evaporation [239]. The typical currents used in my experiments are in the range $5 - 8$ A, corresponding to a temperature of $650 - 850$ °C. Specifically, a current of $5 - 6$ A has been used for Cs evaporator, $5.5 - 6.5$ A for K evaporator and $7.5 - 8$ A for Li evaporator. For these current values, not reported in the AMD datasheet, it is possible to have a relatively small evaporation rate. Typical calibration curves for these AMDs, obtained by means of a quartz microbalance, are reported in Figure 3.7a-c. The behaviour of such evaporators for very low currents can vary noticeably depending on the evaporator, even for evaporators within the same production batch. The amount of evaporated alkali metal is nonlinearly dependent on the evaporation time, as shown in Figure 3.7d. Nevertheless, the operating time for my experiments is about 5 min and the dependence of the amount of alkali metal evaporated with respect to time can be considered linear. The evaporator source is operated maintaining a chamber pressure in the low 10^{-8} mbar regime.

3.2.3 Sample preparation

In my experiments, single layer graphene grown by CVD on polycrystalline copper foil provided by the University of Basel and by ASC Material Ltd has been used. Islands of a second graphene layer grown on the top of the monolayer graphene can be found in the CVD grown graphene, allowing to investigate the metal deposition on single layer and bilayer graphene on the same region of interest. The sample frame for LEEPS measurements is a 100 nm thick SiN membrane with 500 nm $\times$ 500 nm holes milled using a Focused Ion Beam.

We use a standard technique to transfer graphene, using Poly(methyl methacrylate) (PMMA) as a sacrificial layer. The graphene is spin coated with an about 100 nm thick PMMA layer. The underlying copper foil is removed by chemical wet-etching in a solution of 0.2 M of Ammonium Persulfate (APS). The PMMA covered graphene flakes are then

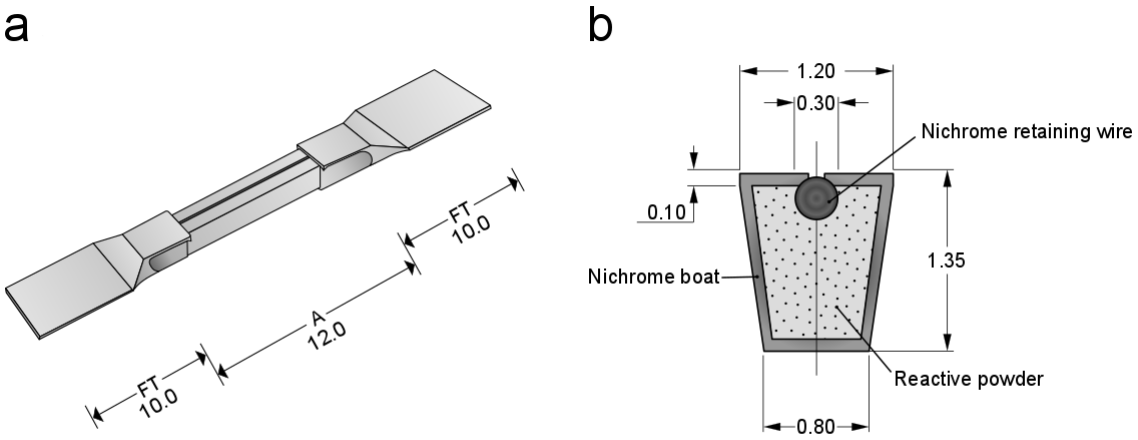

Figure 3.6: The Alkali Metal Dispenser (AMD) manufactured by SAES Getter S.p.a. [234]. (a) 3D sketch of the AMD. The Flat Terminals (FTs) are 10 mm long and 2.5 mm wide, allowing for an easy handling and mounting on the electrodes. AMDs are fastened the inner body of the evaporator unit, shown in Figure 3.5a, by means of screws through holes drilled in the terminals. We used evaporators with an active length of $A = 12$ mm. (b) Cross-section of the AMD. The reacting powder, a mixture of alkali chromate salt and a reducing agent, is contained in a nichrome boat. The alkali metal vapour is released from the slit within an emission angle of 100°. A nichrome wire in the slit avoids the leaking of powder and increases the mixture compression. Thanks to the well-defined geometry, these evaporators perform in a highly reproducible manner. All the reported measures are in mm.

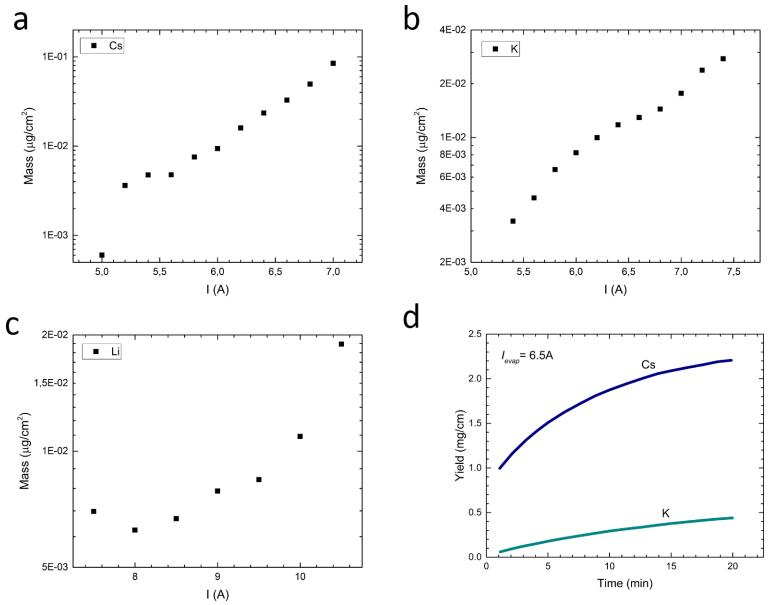

Figure 3.7: (a) Cs evaporator calibration. (b) K evaporator calibration. (c) Li evaporator calibration. (d) Yield for Cs and for K evaporator at the same firing current from the SAES Getters datasheet [234]. The evaporation rate for Li dispensers is not available in the datasheet.

rinsed several times in ultraclean deionised water to remove residues of the APS. Afterwards the flakes are transferred onto the palladium covered substrate and dried in air at 80 °C for 30 minutes.

The PMMA layer is removed by taking advantage of the catalytic properties of platinum-metals [240]. The palladium on the substrate acts as a catalyst, dissociating the hydrogen molecules of the polymer. The PMMA is thus dissociated into lighter molecules and monomers that desorb to the gas phase. The process is activated in air at temperatures in the range $175 - 350$ °C. The membranes are coated with 10 nm of chromium and 25 nm of palladium on each side by using a high-vacuum sputter coater. It has been demonstrated that with this technique nanometre-sized islands are formed on the surface, enhancing the catalytic process [240]. Moreover, the catalytic reaction extends over tens of micrometres wide region along the platinum-metal edge [240], efficiently removing the PMMA from the suspended graphene flake.

After the annealing in air at 300 °C for 90 min, the still hot sample is immediately transferred into the microscope load lock. A fast transferring towards the UHV main chamber is a crucial step for ensuring clean graphene with only a few visible adsorbates

in LEEPS microscopy.

To our knowledge, only few studies related to graphene thermal stability and oxidation after thermal annealing in air are present[5] [241–243]. The temperatures used for the catalytic process ($175 - 350\,^{\circ}\mathrm{C}$ [240]) are below the values of $450 - 550\,^{\circ}\mathrm{C}$ reported in these studies for a complete oxidation of graphene. It should be noted that there are indications of a much reduced oxidation for sample treatments at the temperature of $300\,^{\circ}\mathrm{C}$ [242]. DFT simulations have shown that a charge transfer occurs between graphene carbon atoms and oxygen, with the oxigen gaining a negative charge upon adsorption [244]. Therefore, since our samples exhibit typically just a few black spots in the hologram, we assume that no significant graphene oxidation is present in our sample at measurement time. However, no dedicated measurements of graphene oxidation in relation to this work have been carried out.

3.2.4 Distortion corrections

The LEEPS microscopy, being a lens-less setup, should be free from the aberrations induced by a lens system. Nevertheless, the presence of electric and magnetic fields could give rise to distorted images on the detector. Specifically, the source of distortion has been found in a few stainless steel components with a non negligible residual magnetization. We have had to deal with two types of distortions. The first one is a non uniform distortion, due to the presence of the magnetized elements. The distortion vector field of the images (Figure 3.8) shows vectors with different orientation and intensity distributed on the detector area. A proper correction of such images is a challenging task. The second type is a uniform distortion, observed after having removed the magnetized elements. The effect of this last kind of distortion is similar to astigmatism in TEM images, and therefore the same techniques can be applied to correct it. As calibration sample, a regular holey carbon support film (Quantifoil®) has been used. The fit to an ellipse on each hole provided an estimate on the direction and on the intensity of the distortion.

[5] In the work of Surwade *et al.* [241] oxidised graphene has been obtained by annealing at $550\,^{\circ}\mathrm{C}$ for 20 min under atmospheric oxygen. Liu *et al.* [242] instead heated graphene in an O_2/Ar gas flow for 2 hours finding oxidised graphene at $450\,^{\circ}\mathrm{C}$. Moreover, they found that an annealing at $300\,^{\circ}\mathrm{C}$ causes hole doping in graphene due to the charge transfer between adsorbates like H_2O and O_2 and graphene. Comparable results were found by Nan *et al.* [243], who report defects in graphene at $500\,^{\circ}\mathrm{C}$ and instabilities in graphene edges at $200\,^{\circ}\mathrm{C}$. One of the factors influencing the thermal stability of graphene is the presence of intrinsic defects and domain boundaries, which are non-uniformly distributed in CVD graphene and are the most favourable sites for O_2 adsorption.

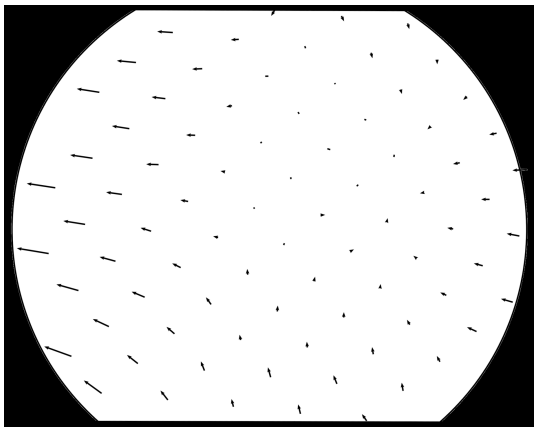

Figure 3.8: Distortion vector field of images affected by non-uniform distortions due to magnetised components in the evaporator unit. The modulus of the longest vector, visible on the left side of the image, corresponds to a ratio between the minor and the major axis of 0.68.

Uniform distortion

The simplest case of distortion in a TEM is due to astigmatism, which is described as a different magnification along the x and the y axis. This means that a circular object appears elongated in the image, and so it can be described by an ellipse. In LEEPS microscopy, a uniform electric field can give rise to the same effect. Therefore, I applied TEM astigmatism correction techniques (described in the works of Zhao *et al.* [245] and Yu *et al.* [246]) to my data.

The first step is to estimate the strength of the anisotropy, and therefore the orientation and the amount of distortion. As a test sample, a TEM carbon grid Quantifoil® R0.6/1 with 600 nm diameter holes has been used. The contour of each hole has been extracted through a Canny filter, and a nonlinear least-square method has been applied to each contour to fit it to an ellipse. The quantities we are interested in are the length of the major axis a, the minor axis b, and their orientation with respect to the coordinates system of the image. In particular, the angle θ between b and the x axis has been considered. Since the values of a and b depend on the magnification used during the acquisition, it is necessary to introduce the parameter α that is given by is the ratio between the minor and the major axis of the fitting ellipse and, thus, is independent on the magnification. The values $\alpha = 0.864$ and $\theta = 1.8°$ have been obtained.

The second step is to correct such a distortion through mathematical transformations.

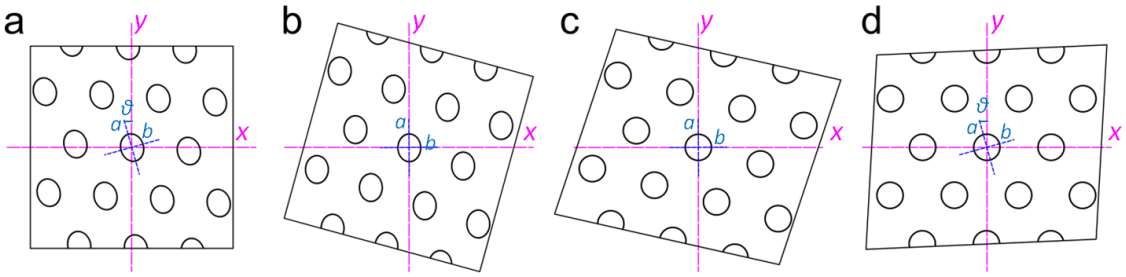

Figure 3.9: The correction for elliptic distortions using a Quantifoil R0.6 as a test sample. (a) The length of the major axis a, the minor axis b, and their orientation θ with respect to the system of axis of the image are estimated. (b) The image is rotated by θ to align the ellipse axis to a reference axis. (c) The image is compressed in such a way that $a = b$. (d) The image is rotated back by θ.

The correction of elliptic distortion, depicted in Figure 3.9, is a three-step process:

1. the image is rotated to align the ellipse major axis to the y axis;
2. the ellipse new y axis is scaled to be equal to the minor axis;
3. the image is rotated back.

From the mathematical point of view this corresponds to the following transform:

$$\begin{bmatrix} x' \\ y' \end{bmatrix} = \begin{bmatrix} \cos\theta & -\sin\theta \\ \sin\theta & \cos\theta \end{bmatrix} \begin{bmatrix} \alpha & 0 \\ 0 & 1 \end{bmatrix} \begin{bmatrix} \cos\theta & \sin\theta \\ -\sin\theta & \cos\theta \end{bmatrix} \begin{bmatrix} x \\ y \end{bmatrix}$$

where θ is the angle between the minor axis and the x axis, and $\alpha = b/a$. In this way, each point $P = [x, y]$ is transformed in $P' = [x', y']$. Since the pixel coordinates of the P' points could not be integer values, it is necessary to interpolate the points of the new image. For this purpose, a bicubic interpolation has been used.

Chapter 4

Metal adsorption and nucleation on free-standing graphene

As detailed in the previous chapter, low-energy electron holography is a compelling technique to investigate single adsorption events of alkali metals on free-standing single layer and bilayer graphene. Indeed, low-energy electrons are extremely sensitive to localised charges (see section 3.1.4), such as the positive ion resulting from the adsorption of an alkali atom on graphene. Moreover, as graphene exhibits a transparency of approximately 70% per layer to electrons with an energy in the range 30-250 eV, it is conceivable that alkali metals adsorbed on bilayer graphene or intercalated between the two graphene layers can be detected.

This chapter presents the experimental results of alkali metals deposited on free-standing graphene. The first section is dedicated to the adsorption of Cs, K and Li. The second section is dedicated to investigating the behaviour of such alkali metals deposited on adjacent domains of single layer and bilayer graphene. For comparison, the deposition of a non-alkali metal, namely Pd, is investigated. The third section is dedicated to investigating the effect of the electron beam on the growth of Pd clusters and comparing the LEEPS microscopy vs. the TEM images of such clusters. The last section reports the use of Pd clusters as anchors for Cs nucleation. All reported data have been acquired at room temperature.

4.1 Adsorption of alkali metal atoms on free-standing single layer graphene

In LEEPS microscopy, the signature of a positively charged ion adsorbed on free-standing graphene is a bright spot on the detector [61]. It is well known that an alkali atom adsorbed on graphene easily donates its outermost electron, giving rise to a polar bonding [34, 45, 72]. The amount of charge transferred and the distance between the alkali ion and the graphene layer have been reported in the literature for coverages above the (6×6) supercell, corresponding to a coverage of 0.11 ML for K and Cs and of about 0.03 ML for Li[1]. As described in section 2.1.1, the values of the charge transferred obtained by DFT simulations are slightly different in different works, depending on the functional implemented; for the (6×6) supercell, typical values calculated for the charge transfer are close to $1\,e$. Thus, at very low coverages, such as those typically used in this thesis, it is reasonable to assume that the charge transfer from the alkali adatom to the graphene layer underneath amounts to one elementary charge. Moreover, the presence of single-atom adsorbates is guaranteed by the dipole-dipole repulsion between the alkali metal atoms on graphene. The formation of clusters is thus unlikely to occur at low coverage on a perfect graphene layer.

The cleanliness of the vacuum chamber is crucial for adsorption experiments and has therefore been checked before each experiment, comparing the images of the selected window acquired soon after the insertion of the sample in the microscope and after 30 min. This interval of time is much larger than the typical deposition times of alkali metals and comparable with that of Pd. This check ensures that a negligible amount of impurities from the residual gas in the chamber will be deposited on the sample.

Figure 4.1 shows typical holograms of Cs deposited on free-standing single layer graphene. Two phenomena are observable during Cs deposition: the adsorption of new atoms and the migration of the already adsorbed ones. This is apparent from the movie of the acquisition, from which a sequence of eight subsequent frames is shown in Figure 4.1a. Because the Cs diffusion on graphene is extremely fast for the 40 ms time resolution of the experimental setup, tracking an individual adsorbate would be a challenging task. In addition to Cs

[1]The coverage here is defined as $\theta = N/N_{\max}$, where N is the number of adsorbates and $N_{\max}$ is the maximum number of adsorbates achievable, that is, the density of adsorbates required to cover the surface with 1 ML of atoms. According to Caragiu et al. [71], 1 ML of K and 1 ML of Cs on a graphite surface corresponds to the (2×2) phase, where 1 alkali atom corresponds to 8 C atoms. In contrast, Li can form 1 ML on graphite with a (1×1) supercell, in which 1 Li adatom corresponds to 2 C atoms.

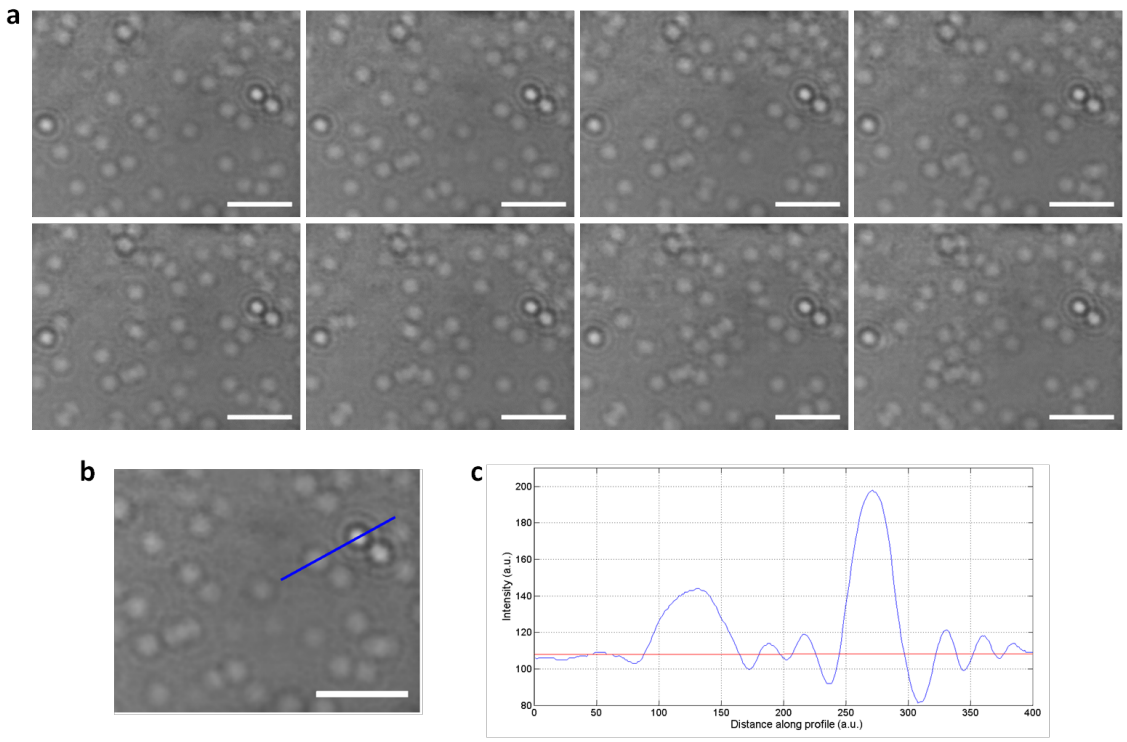

Figure 4.1: Cs on free-standing graphene during the deposition. (a) Subsequent frames acquired at a frame rate of 25 fps and with electron beam energy of 90 eV. The scale bars correspond to 50 nm. These holograms are distortion corrected according to the procedure described in section 3.2.4 and background subtracted. (b) First image of the previous sequence. The blue line across the Cs adsorbate and a charged cluster indicates the position for which the intensity profile (c) has been acquired. The red line in (c) indicates the background level. The selected profile is about 70 nm long.

adatoms, adsorbates exhibiting no dynamic are present in these holograms. These adsorbates are indicated by a much more intense spot and are likely the result of Cs nucleation on pre-existing small clusters. Such clusters can be identified in the hologram recorded before the deposition started and likely originate from the sample preparation process. Figure 4.1b shows one of the clusters and a Cs adatom next to it, and the intensity profile across them has been measured (Figure 4.1c). The intensity of the bright spot of the cluster is 2.6 times higher than the intensity of the Cs atom[2]. In the assumption that the bright spot due to Cs ion is originated by a $+e$ charge and according to the simulations reported in Ref. [61], the charge of the cluster should amount roughly to $+2.6e$.

The Cs deposition evolution is illustrated in Figure 4.2. Under these experimental conditions, the bright spots of the Cs ions overlap above a density of about 0.01 N_{Cs}/nm^2, corresponding to a coverage of 0.05 ML, and individual atoms are challenging to be resolved. However, this density is still low enough not to observe the decrease in the charge transfer with the coverage predicted in the literature [77, 78, 80]. An interesting effect, shown in the frames reported in Figure 4.3, can be observed once deposition stops. The density of adsorbates drastically decreases in less than 60 s until reaching an equilibrium state in about 100 s. As shown in Figure 4.4, a slightly higher concentration of bright spots has been found close to the rim of the suspended graphene window; however, it does not justify the huge amount of Cs adatoms missing from the graphene window. A plausible hypothesis could be that Cs adatoms migrate towards the frame of the free-standing window and reach the graphene areas supported by the Pd-coated substrate, where the binding may be energetically favoured with respect to the free-standing graphene. Undoubtedly, dedicated measurements on the supported graphene areas, e.g. by means of STM, are necessary to shed light on this phenomenon.

The hologram of K deposited on free-standing graphene seen in Figure 4.5a, shows bright spots exhibiting a wide intensity profile. The behaviour during K deposition and after the deposition was stopped is similar to that reported for Cs, with a pronounced reduction of the density of adsorbates within 60 s once the deposition has been stopped. On the contrary to the above-mentioned alkali metals, Li hologram shows bright spots with a smaller size, as shown in Figure 4.5b. Moreover, after the deposition has been stopped, Li adatoms persisted on the adsorption sites. This behaviour is in agreement with DFT

[2]The ratio has been calculated as $(I_{max}(c) - B)/(I_{max}(Cs) - B)$, where $I_{max}(c)$ is the maximum in the intensity profile for the cluster, B is the background level (indicated with the red line in Figure 4.1(c)), and $I_{max}(Cs)$ is the maximum in the intensity profile for the Cs adsorbate.

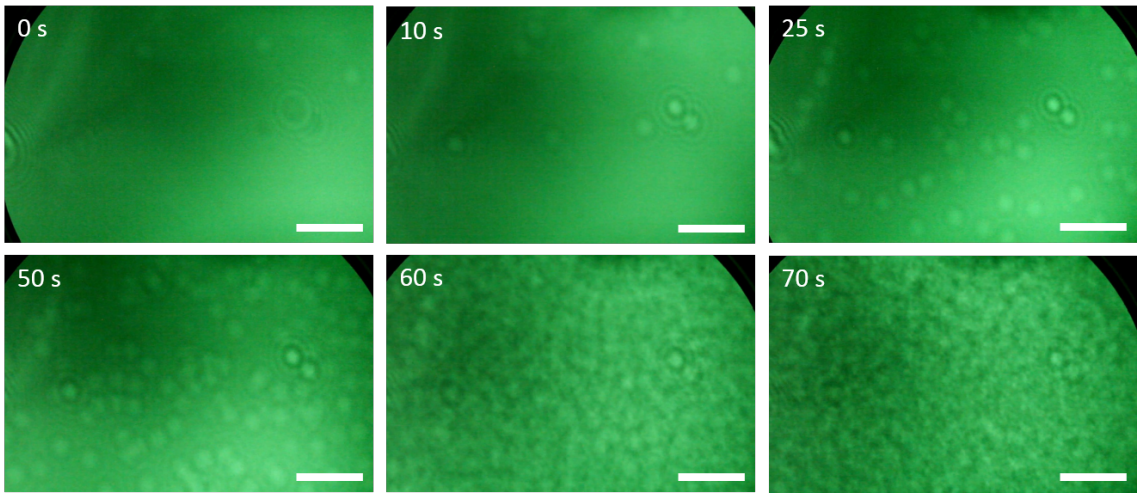

Figure 4.2: Holograms showing the deposition evolution of Cs. The evaporator has been operated at 5.1 A. The energy of the electron beam is 90 eV. The scale bars correspond to 50 nm.

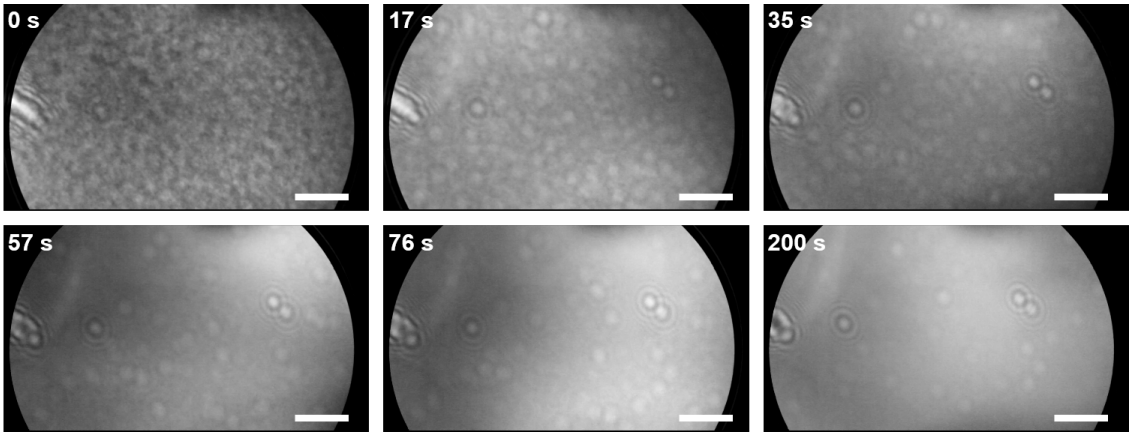

Figure 4.3: Holograms acquired at different times after having stopped Cs deposition. The amount of Cs adatoms in the region of interest drastically decreases within 60 s and reaches an equilibrium distribution in about 100 s. The energy of the electron beam is 90 eV. The scale bars correspond to 50 nm.

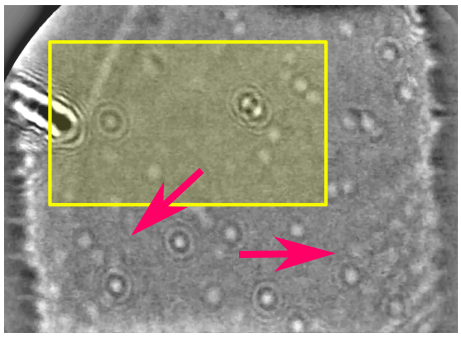

Figure 4.4: Hologram of the graphene window acquired 240 s after having stopped Cs deposition. The yellow area indicates the ROI reported in Figure 4.3, while the magenta arrows indicate the Cs ions accumulated at the rim of the window. The energy of the electron beam is 93 eV. The graphene window is 500 nm wide.

calculations reported in section 2.1.1: the larger diffusion barrier for Li [79], together with the reduction of the nucleation barrier with the coverage [82], favours the aggregation of Li atoms with respect to single-atom adsorption on graphene at high coverages. Moreover, a three-dimensional shape has been predicted for small clusters [82]. A possible picture is thus that some of the Li adatoms diffusing on the graphene surface may be at a close distance to each other; the generated local high density of adsorbates could result in the formation of a stable cluster.

4.2 Alkali metal atoms on adjacent domains of free-standing single layer and bilayer graphene

The contents of the following section belongs to the manuscript:

M. Lorenzo, C. Escher, T. Latychevskaia, H.-W. Fink, *Metal Adsorption and Nucleation on Free-Standing Graphene by Low-Energy Electron Point Source Microscopy*, Nano Letters, 18 (6), pp. 3421–3427, 2018.

For the series of experiments reported in this section, single-layer CVD graphene grown on copper (manufactured by ASC Material, Ltd) exhibiting a few areas of bilayer graphene has been employed. In the CVD process, islands of a second layer can grow on top of the continuous first graphene layer; therefore, monatomic step edges are present on the side

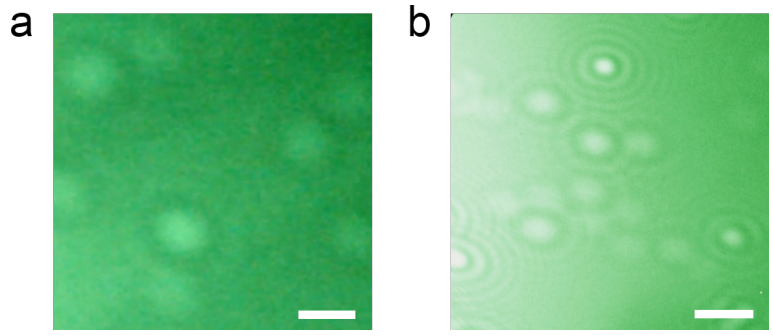

Figure 4.5: K and Li deposited on free-standing graphene. (a) Hologram of K deposition acquired with 52 eV electrons. (b) Hologram of Li deposition acquired with 55 eV electrons. Even though the holograms are affected by distortions, K ions are evident, indicated by a wider bright spot with respect to Li. The scale bars correspond to 20 nm.

covered by the PMMA during the sample preparation. Windows exhibiting adjacent domains of single layer and bilayer graphene have been selected to simultaneously investigate metal deposition on both areas. From the findings reported in chapter 2, it is plausible to expect alkali metal intercalation in the bilayer graphene domain by diffusion through the step edge, as illustrated in Figure 4.6a. In order to access this intercalation mechanism, samples were inserted into the LEEPS microscope with the step edge oriented towards the evaporator, as sketched in Figure 4.6b.

4.2.1 Potassium and Lithium deposition

As already stated, in LEEPS microscopy the signature of an alkali metal atom adsorbed on free-standing graphene is a bright spot in the hologram. The count of such spots has been performed by visual inspection, as the use of automated recognition codes frequently failed in discriminating bright spots originated by positively single charged entities from those originated by two close charged entities or single charged entities overlapping with interference fringes, as those originating from the border of the second graphene layer or from a pre-existing cluster. Nevertheless, for some bright spots a correct identification could not be possible. This is taken into account for the determination of the uncertainty of the counted particles. The number of particles is then given by the mean value between N_{min}, the number of particles unambiguously identified, and $N_{\mathrm{max}} = N_{\mathrm{min}} + \Delta N$, the number of particles identified assuming that all the counted bright spots arise from individual charged particles. The uncertainty ΔN is accounted for, together with the

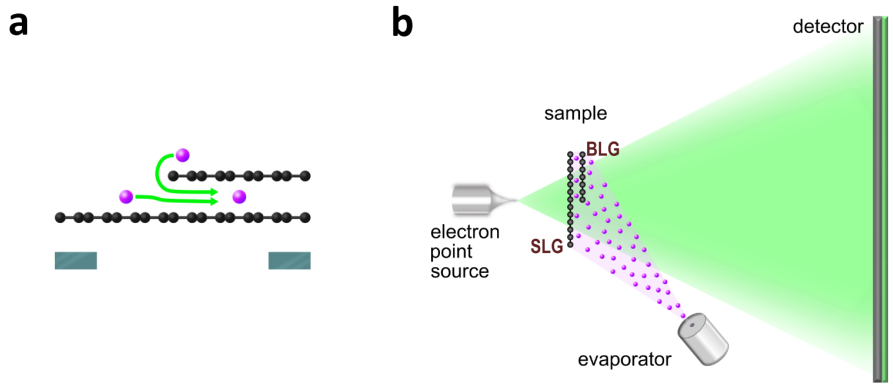

Figure 4.6: Sketches of the measurement method used to study the deposition of alkali metals on graphene. (a) The step edge made by the second graphene layer and the underlying first layer of graphene. (b) A scheme of the experimental setup showing the sample orientation.

statistical error $\sqrt{N_{\min}}$, in the total error of the number of particles. The particle density has been calculated for a quantitative estimate and comparison of the alkali metal amount on single layer and bilayer graphene domains. At low coverages, the dipole-dipole repulsion between alkali metal adatoms on graphene prevents cluster formation, allowing to observe individual atoms. The formation of alkali metal clusters can occur by nucleation on pre-existing contaminants. Such adsorbates have been identified in the hologram acquired before the deposition, and thus their contribution to the density of adsorbates is subtracted.

In our data, atoms adsorbed on the top surface or intercalated in the bilayer graphene domain exhibited the very same signature, and their discrimination has not been considered for the analysis performed in this section. From simple electrostatic simulations reported in appendix A, the trajectories of the probing electrons are deflected more by an adsorbed ion than by an intercalated one. Nonetheless, the intensity profiles of the imaged bright spots in the single layer and bilayer graphene domains do not allow to discriminate adsorbed from intercalated ions. A reason for this discrepancy may be due to the oversimplified model used in our simulations, not reflecting the realistic charge redistribution of an intercalated alkali metal atom. DFT simulations would be helpful to identify experimental conditions that would eventually allow for a different signature of an adsorbed and of an intercalated alkali metal ion. However, an indirect evidence of alkali metal intercalation in

the bilayer graphene domain is provided by the particle density analysis on single layer and bilayer graphene. Also for small alkali metal clusters, that may form at high coverages, each bright spot is simply counted as one entity.

Deposition evolution

The temporal evolution of K on adjacent single layer and bilayer graphene domains has been imaged during the whole deposition by acquiring subsequent holograms with an approximate delay time of 5 s. A sequence of 8 of such images is shown in Figure 4.7. In Figure 4.9a the plot of the particle density per unit area as a function of the deposition time is reported; data are shown until $t = 87$ s while the deposition was lasting for longer time (136 s). For $t > 87$ s, and thus for higher coverages, the identification of single entities is not trivial and leads to large uncertainties on the particles counting, especially on the bilayer graphene domain. As shown in Figure 4.7 and Figure 4.9a, above a particle density of $\rho_K \approx 3 \times 10^{-4}\,N_K/nm^2$ an increase of K in the bilayer graphene with respect to the adjacent single layer graphene domain is evident, resulting about 3 times higher in the bilayer domain than in the single layer domain at $t = 87$ s.

As detailed in section 2.2, experimental studies on related systems report the intercalation through vacancy defects taking place above a critical coverage [75]. The density of adsorbates for this critical coverage is two orders of magnitude higher than in the presented experiment. In addition, the intercalation through vacancy defects on graphite has been observed only at high temperatures, while at room temperature it has been observed only nucleation in correspondence of these defect sites and the intercalation pathway is through step edges on the basal plane [247]. Therefore, it is conceivable to assume the diffusion through the step edge as the principal intercalation mechanism in the above reported data (Figure 4.6).

Lithium deposition has been recorded with a frame rate of 25 fps. In Figure 4.8, a few frames recorded during the deposition are shown. The plot of the Li particle density on single layer and bilayer graphene as a function of time is reported in Figure 4.9b. As in case of K deposition, also for Li the identification of single entities was possible only in the first 160 s out of 220 s of total acquisition. Also, the evolution of Li deposition is similar to what observed for K. Above the threshold density of $\rho_{Li} \approx 8 \times 10^{-4}\,N_{Li}/nm^2$, the density in the bilayer graphene domain increases with respect to the single layer graphene domain, reaching at $t = 160$ s a value about 2.3 times higher than on the single layer

graphene domain. These results are in qualitative agreement with DFT calculations for Li in the bilayer graphene, predicting that the intercalation is energetically more favourable than the adsorption [134]. More details about these simulations are reported in the section 2.2. As for K, also for Li the intercalation most likely occurs by diffusion through the step edge.

The movie on Li deposition shows an increase of the particle density in the bilayer graphene while little diffusion can be observed for Li adatoms. This result can be interpreted in terms of different mobility for adsorbed and intercalated Li atoms, with the mobility on the single layer being much higher than in between the bilayer. The bright spots identified on the single layer graphene domain are most likely localised at or around defects in graphene and can perform limited hopping around these "traps". The Li atoms newly adsorbed form the vapour phase onto the single layer graphene are probably moving very rapidly and are not detectable with 25 fps before they reach the step to the bilayer graphene domain and intercalate in between the two layers where, as a consequence, the density apparently increases. The same picture probably applies also to those atoms that adsorb on the top of the bilayer graphene domain and diffuse reaching the domain boundary at a descending step. Under these considerations, the temporal evolution data reported in Figure 4.9 can be interpreted as follows: the number of detected particles in the single layer graphene domain might be less than the number of adsorbed atoms. Assuming that the diffusion of the adsorbates is similar in both domains, ρ_{SLG} coincides with the density of detected adsorbates in the bilayer graphene domain. Given this, ρ_{SLG} is the adsorbates' contribution to the total particle density ρ_{BLG} in the bilayer graphene. The faster increase of ρ_{BLG} with respect to ρ_{SLG} during the deposition, shown in Figure 4.9, provides evidence that the excess of particles measured in the bilayer graphene domain is due to intercalated ions.

Equilibrium state

While the evolution of K and Li deposition exhibited similar features, the evolution of their particle distribution was significantly different once the evaporator has been stopped. On the left side of Figure 4.10, images acquired a few seconds before interrupting the deposition of K (Figure 4.10a) and Li (Figure 4.10c) are reported, while on the right side holograms acquired more than one minute after the deposition was stopped (Figure 4.10b and Figure 4.10d for K and Li, respectively) are shown. Observing the evolution

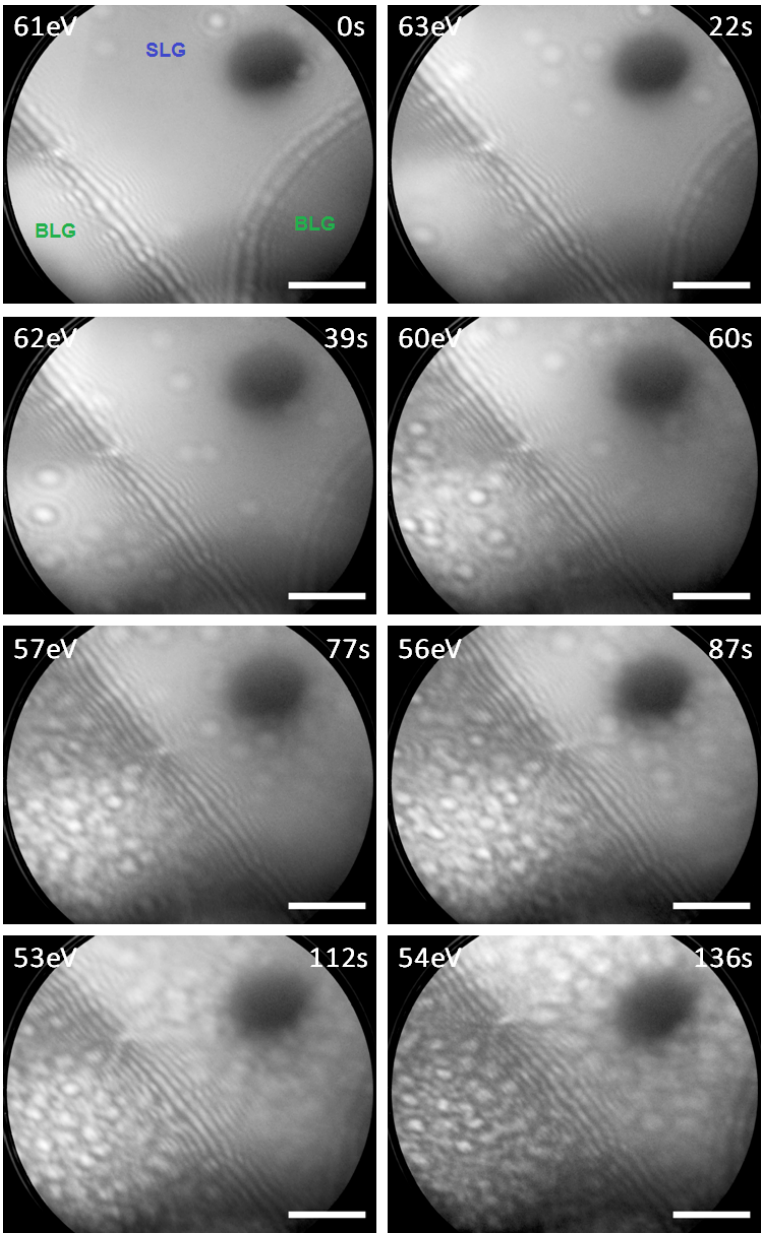

Figure 4.7: Holograms of free-standing single layer (SLG) and bilayer (BLG) graphene acquired at different times during K deposition with an exposure of 0.5 s. The K evaporator has been powered with a current of 6.5 A. The scale bar corresponds to 50 nm.

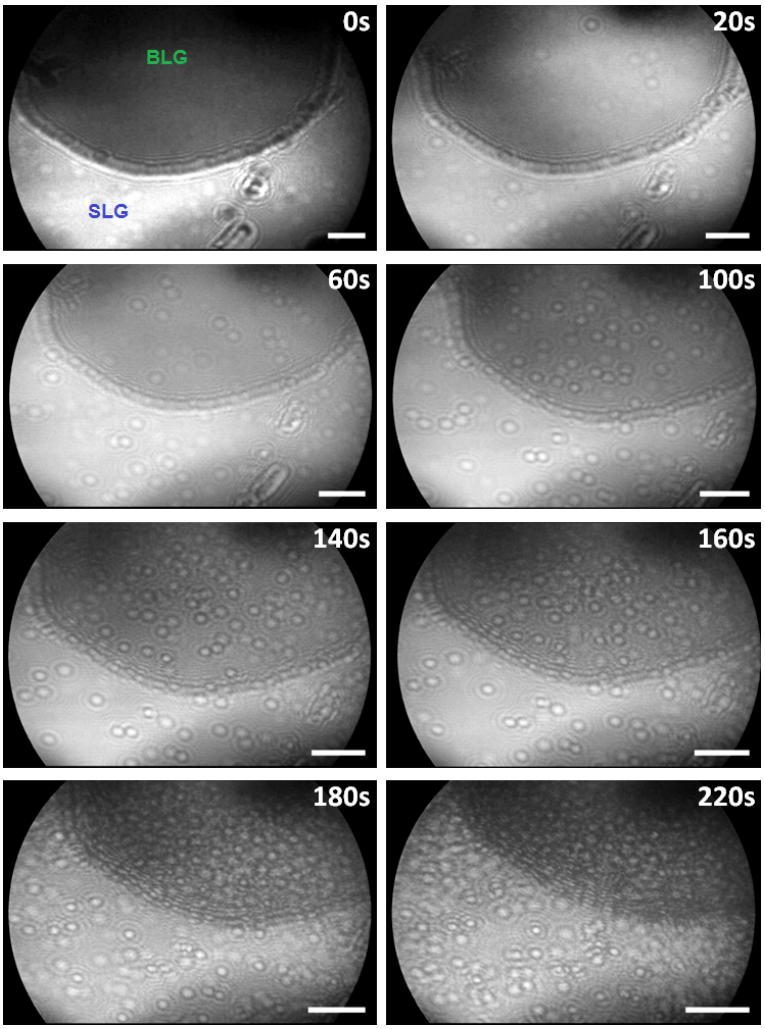

Figure 4.8: Holograms of free-standing single layer (SLG) and bilayer (BLG) graphene acquired at different times during Li deposition. Each image has been acquired with an electron energy of 80 eV and an exposure of 40 ms. Li has been deposited powering the evaporator with a current of 7.6 A. The scale bar corresponds to 50 nm.

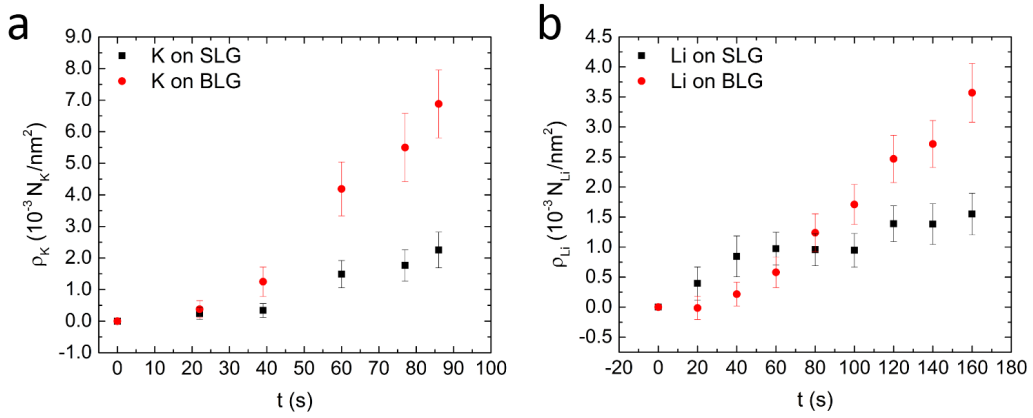

Figure 4.9: Temporal evolution of K and Li density of particles on free-standing graphene. (a) Density of K particles on single layer graphene (SLG) and on bilayer graphene (BLG) as a function of time. (b) Density of Li particles on SLG and on BLG as a function of time.

of the particle densities after interrupting the deposition, samples showed no significant variations in the density of particles on each domain already after 40 s. For this reason, a time interval of 90 s for K and 60 s for Li from the end of the deposition has been supposed to be long enough to consider samples having reached an equilibrium distribution.

In the hologram concerning K acquired soon before the end of the deposition (Figure 4.10a) both single layer and bilayer graphene domains are populated; Figure 4.10b, acquired at the equilibrium distribution, shows instead a pronounced decreasing of coverage on the single layer graphene, with respect to the bilayer domain that remains highly populated. The particle densities obtained from this last image are $\rho_{SLG} = 3.9 \times 10^{-4}\,N_K/nm^2$ on the single layer graphene and $\rho_{BLG} = 9 \times 10^{-3}\,N_K/nm^2$ on the bilayer graphene domain, corresponding to a coverage of $\theta_{SLG} = 0.81 \times 10^{-4}$ ML and $\theta_{BLG} = 1.9 \times 10^{-3}$ ML[3]. For these low coverages, the distance between K particles is large enough to neglect the Coulomb interaction between them. Assuming that the thermodynamic equilibrium has been reached and that transitions between the single layer and the bilayer graphene domain occur without altering the average densities of particles in the two domains, the difference in the free energy of binding ΔE between the binding states on the single layer

[3]The coverage is here calculated as $\theta = \rho/\rho_{max}$, where ρ is the density of adsorbates and ρ_{max} is the maximum density of adsorbates achievable (i.e. the density of 1 ML of atoms). 1 ML of K on the graphite surface corresponds to a density of 4.8 atoms/nm^2 [71]. For the bilayer graphene, this value represents the maximum density of K intercalated achievable.

and bilayer graphene can be related to the ratio between ρ_{SLG} and ρ_{BLG} through the Boltzmann factor:

$$\frac{\rho_{\mathrm{SLG}}}{\rho_{\mathrm{BLG}}} = e^{-\frac{\Delta E}{k_{\mathrm{B}}T}} \tag{4.1}$$

where k_{B} is the Boltzmann constant and T the absolute temperature. From this equation, a value of $\Delta E = 0.08 \pm 0.01$ eV has been obtained, which indicates that the intercalation in the bilayer graphene is energetically more favourable than the adsorption on the single layer graphene. In this analysis the existence of only two binding states has been assumed: K can be adsorbed on the single layer graphene domain or can be intercalated between the two graphene layers in the bilayer graphene. This assumption holds in the case of perfect single layer and bilayer graphene. However, there might be trapping sites, like vacancy defects, that constitute a third binding state. Hence, the calculated free energy difference of binding assuming ideal graphene is an underestimated value and should therefore be considered as a lower limit. A further argument supporting the interpretation of intercalated K in the bilayer graphene domain comes from the calculation of the density of intercalated particles. Under the assumption that the density of adsorbates is the same on both domains, the density of intercalated particles is given by $\rho_{\mathrm{int}} = \rho_{\mathrm{BLG}} - \rho_{\mathrm{SLG}} = (9 \pm 1) \times 10^{-3}\,\mathrm{N_K/nm^2}$. Thus, the contribution of the adsorbed particles to ρ_{BLG} is minimal, and the bright spots observed in the bilayer graphene domain arise mostly from intercalated ions.

In contrast to the observed behaviour of K atoms, deposited Li particles were still present on both the single layer and the bilayer graphene domains 60 s after the evaporator has been turned off (Figure 4.10c-d). The single layer graphene domain showed holograms of clusters featured by different size and shape. Moreover, no dynamics have been observed for such clusters. Therefore, no equilibrium distribution can be assumed, and consequently, no binding energy calculation can be performed. The formation of stable Li clusters on the single layer graphene, however, is consistent with DFT simulations reported in the literature and summarized in section 2.1.1, predicting that the nucleation barrier decreases with Li coverage, overcoming the dipole-dipole repulsion and favouring the aggregation of Li atoms [82, 133, 248]. In the bilayer graphene domain, instead, few features show some mobility, although strongly limited by the surrounding charged stable features. The analysis of the dynamics of 17 features on an area of $6.5 \times 10^3\,\mathrm{nm^2}$ is reported in the

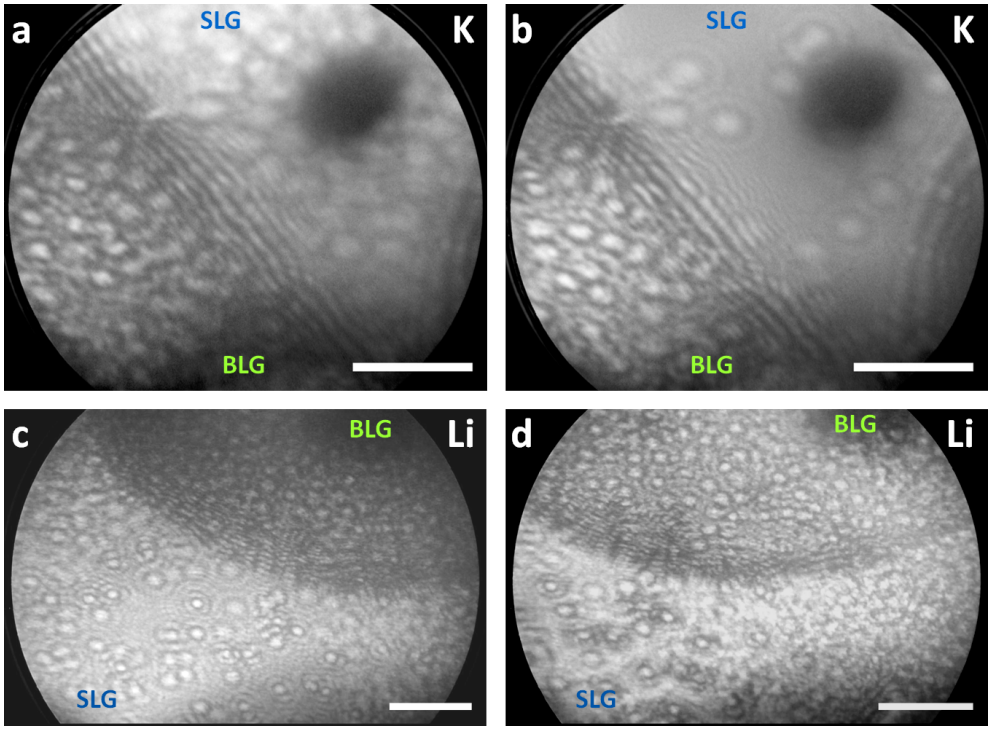

Figure 4.10: Distribution of K and Li deposited on free-standing single layer graphene (SLG) and bilayer graphene (BLG). (a) Hologram acquired after continuous K deposition for 136 s with 54 eV electrons and (b) 90 s after the deposition has been stopped, imaged with 57 eV electrons. (c) Hologram acquired after con- tinuous Li deposition for 220 s and (d) 60 s the deposition has been stopped. Both holograms are acquired at an electron energy of 80 eV. The scale bar corresponds to 50 nm.

Appendix B. A root mean square displacement $\sqrt{\langle r^2 \rangle} \sim 10\,\mathrm{nm/s}$ has been obtained for such features, with a mean jumping rate of about 5 jumps per second. This different behaviour of Li particles on single layer and bilayer graphene domains provides a further indication for intercalated particles in between the bilayer.

4.2.2 Cesium deposition

The deposition of Cs showed results similar to those reported on K. In Figure 4.11a the hologram acquired before Cs deposition is shown. It exhibits several clusters, more concentrated on the single layer graphene likely formed during the sample preparation process. In Figure 4.11b the hologram acquired 90 s after the interruption of the evaporation is reported. As observed with K, the bilayer graphene shows a higher particle density

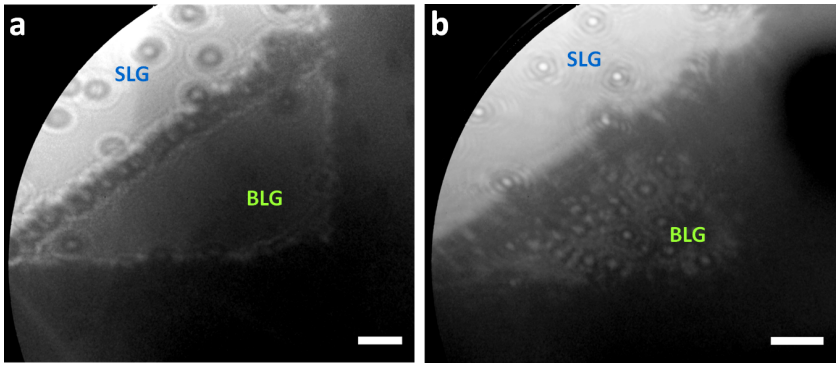

Figure 4.11: Cesium deposition on free-standing single layer graphene (SLG) and bilayer graphene (BLG). (a) Hologram acquired before Cs deposition. It is possible to distinguish pre-existing adsorbates, which are concentrated mainly on the single layer domain. (b) Hologram acquired 90 s after having deposited Cs for 5 min powering the evaporator with $I_{\mathrm{ev}} = 5$ A. The electron beam energy is 100 eV for both holograms. The scale bar corresponds to 50 nm.

with respect to the single layer graphene region. The particle density for Cs amounts to $\rho_{\mathrm{BLG}} = 3.3 \times 10^{-2}\,\mathrm{N_{Cs}/nm^2}$, a value comparable with the corresponding particle density found for K ($\rho_{\mathrm{BLG}} = 9 \times 10^{-3}\,\mathrm{N_K/nm^2}$). On the single layer graphene domain, Cs nucleates around the pre-existing adsorbates forming positively charged clusters, as indicated by the intense bright spot in their holograms. The density of adsorbates on the single layer graphene domain is strongly influenced by these pre-existing clusters, and thus the assumptions of Equation 4.1 are not valid any more. Nevertheless, since on the single layer graphene only Cs adsorbates anchored to the pre-existing contaminations are present, it is reasonable to expect a value ΔE for Cs even larger than in the case of K. This analogous difference in the final distribution on the single layer and bilayer graphene for K and Cs is expected to some extent because of their similar behaviour in other graphene systems, as described in section 2.2; for example, both alkali metals readily intercalate into graphite under similar conditions [64, 71].

4.2.3 Palladium deposition

To complete the picture of alkali metal intercalation, a control experiment depositing Pd as representative of a non-alkali metal has been performed. As in the case of alkali metal experiments, it was selected a suspended graphene window with domains of single

layer and bilayer graphene (see Figure 4.12a). During the deposition, the formation of islands whith roughly the same concentration in both domains has been found. Therefore, no more pronounced concentration on the bilayer graphene as in alkali metal deposition has been observed. In Figure 4.12b the two holograms of Pd on single layer and bilayer graphene are shown, while their amplitude and phase reconstructions are shown in Figure 4.12c. Since Pd adsorbates are neutral objects (they do not exhibit bright spots), their holograms can be reconstructed applying the regular algorithm described in Ref. [196]. Such reconstructions show the formation of islands whose diameter ranges from 22 to 60 nm, characterised by a non-regular shaped border. The experimental setup does not provide information on the thickness of the nucleated clusters, but at the same time data do not contain evidences for Pd intercalation in the bilayer graphene.

This behaviour is consistent with the experimental studies of Pd deposition on HOPG and on supported graphene at room temperature reported in the literature, detailed in section 2.3, where a strong tendency to three-dimensional cluster formation was reported. The intercalation of Pd has been observed only upon thermal annealing at high temperatures. Since the Pd-graphene adsorption energy is smaller than the Pd-Pd cohesive energy, from classical nucleation theory [249] it is conceivable to expect a three-dimensional growth of Pd clusters on graphite as well as on graphene. The deposition conditions for the experiments reported in section 2.3 are not comparable with those used in the present work, in which the Pd cluster growth is influenced by the electron beam illumination (more details about will be provided in section 4.3.1). Despite these differences, even in this case the formation of Pd agglomerates has been observed. No evidence of Pd intercalation in the bilayer graphene domain has been observed. The formation of islands, reported on both domains, could prevent from Pd intercalation at room temperature.

4.3 Palladium deposition on free-standing single layer graphene

The study of metal adsorption and nucleation on free-standing graphene has involved Pd deposition as a representative of the transition metals. This section investigates the effect of the electron beam on the growth (size and density) of Pd clusters. Included is a comparison between the LEEPS and TEM images of the same samples.

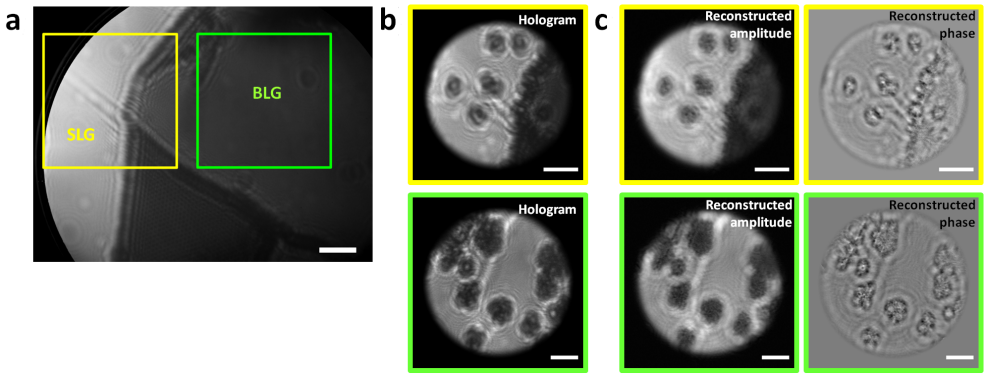

Figure 4.12: Palladium deposition on free-standing single layer graphene (SLG) and bilayer graphene (BLG). (a) The selected window before Pd deposition. The energy of the electron beam is 80 eV. (b) Holograms acquired after Pd deposition. The hologram in the yellow square corresponds to the SLG region indicated in (a), while the one in the green square corresponds to the BLG region. Both holograms are recorded illuminating the sample with 70 eV electrons. (c) Amplitude and phase reconstructions of the holograms shown in (b). In all images, the scale bar corresponds to 50 nm.

4.3.1 The electron beam effect

In a typical metal deposition experiment performed using the LEEPS microscope, a sample is imaged continuously while the metal is deposited. This means that the region of interest (ROI) under investigation is illuminated constantly by the electron beam. In this subsection, the effect of the electron beam on Pd nucleation on free-standing graphene is discussed.

Adjacent graphene windows on the same sample have been selected. One window has been continuously imaged during the Pd deposition with 50 eV electrons and a beam current of 30 nA, while the others have been imaged only before and after the deposition. This ensured the same initial conditions for all the graphene windows and that the same amount of Pd was deposited on them. The evaporator was powered with 4 A, and the deposition lasted 24 min. The area of the formed clusters has been estimated from the amplitude reconstruction of the acquired holograms. A threshold has been applied to the reconstructed image in order to obtain a binary image, in which the background is given by white pixels while the clusters by black pixels. The area of each cluster has been obtained by counting the number of pixels in the corresponding black spot and multiplying this

value by the pixel size[4].

The holograms of two windows acquired after Pd deposition are shown in Figure 4.13. The first row shows a hologram of the window imaged continuously (Figure 4.13a) as well as a hologram of a magnified area of the same window (Figure 4.13b). The amplitude reconstruction of the hologram, seen in Figure 4.14a, shows the formation of 28 clusters the area of which ranges from 73 nm^2 to 1853 nm^2, with a mean value of 604 nm^2. As seen from the area distribution (Figure 4.14b), it is evident that these clusters are not uniform in size or shape, with some of the clusters (especially the ones with a large area) showing an extremely irregular shape. In the second row of Figure 4.13 is a hologram of one of the adjacent windows that was not kept under constant electron beam illumination during Pd deposition (Figure 4.13c) and a magnified area of this window (Figure 4.13d). In this case, the amplitude reconstruction of the first hologram (Figure 4.14c) shows a higher density of smaller clusters with similar shapes. Here, 44 clusters with areas ranging from 15 nm^2 to 435 nm^2 can be identified, the distribution of which is shown in Figure 4.14d. The area mean value is 141 nm^2. For comparison, four other windows were also imaged after the deposition (data not shown); all showed comparable cluster sizes and distribution.

The sum of the areas of all clusters grown on the window kept under electron beam illumination during Pd deposition is 2.7 times higher than the total area of the clusters on the highlighted adjacent window. The emerging picture is that in presence of the electron beam the metal adsorbates prefers to nucleate on the side of a pre-existing cluster rather than on top of it. This behaviour has its origin in the local heating of Pd clusters due to the electron beam irradiation. An additional contribution to the local heating may come from the secondary electrons emitted by Pd clusters upon being hit by the electron beam. The cluster local heating causes an increase of the surface diffusivity of nearby adsorbed molecules and of the capture range of Pd adsorbates. The result is the preferential aggregation of the adsorbates to the Pd island sides contributing to the formation of irregularly shaped borders.

[4]The pixel size Δx is given by the ratio between the size l and the number of pixel N of the reconstructed image, i.e. $\Delta x = l/N = \frac{d_{\mathrm{tip-sample}} L}{d_{\mathrm{tip-detector}} N}$, where $d_{\mathrm{tip-sample}}$ is the distance between the tip and the sample (this value is obtained from the in focus reconstruction), L is the size of the hologram on the detector plane, and $d_{\mathrm{tip-detector}}$ is the distance between the tip and the detector.

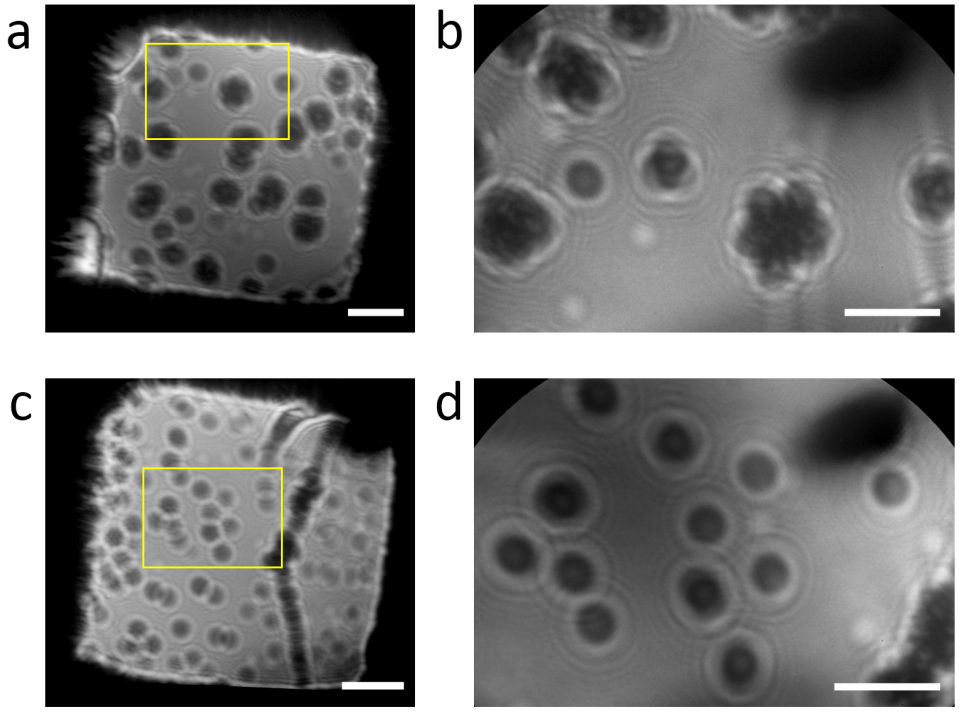

Figure 4.13: Holograms of Pd clusters on graphene. (a) Hologram of the window illuminated by the electron beam during Pd deposition and (b) hologram of a magnified area of the same window, indicated by the yellow rectangle in (a). (c) Hologram of a window imaged before and after the Pd deposition and (d) hologram of a magnified area of the same window, indicated by the yellow rectangle in (c). The energy of the electron beam was 60 eV for (a) and (c) and 50 eV for (b) and (d). The scale bar in (a) and (c) corresponds to 100 nm, while in (b) and (d) the scale bar corresponds to 50 nm. All holograms are distortion-corrected according to the procedure reported in section 3.2.4.

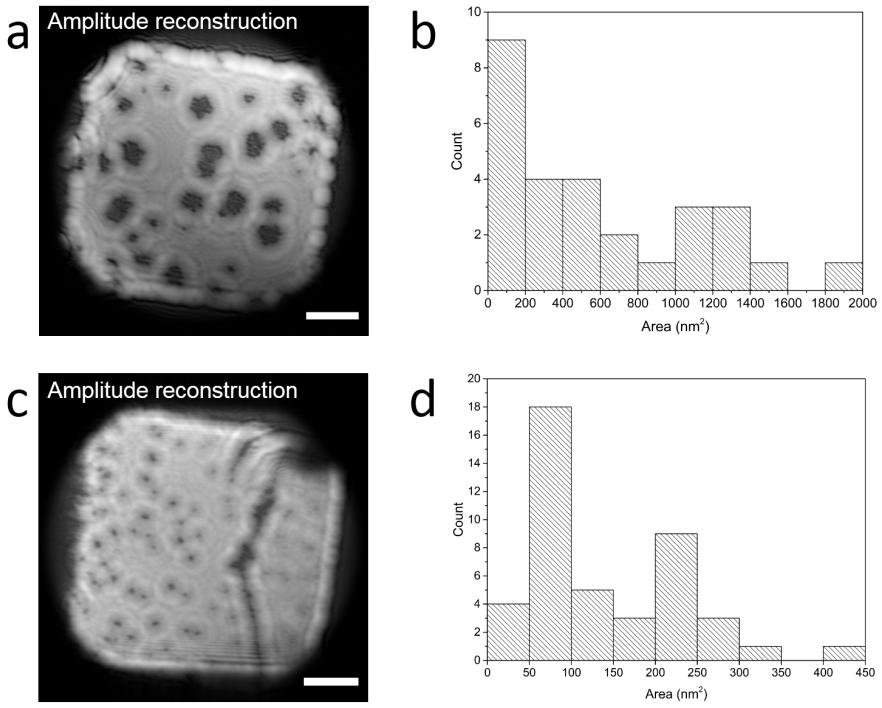

Figure 4.14: Amplitude reconstructions of the holograms shown in Figure 4.13 and their cluster area distributions. (a) Hologram of the amplitude reconstruction of the window illuminated during Pd deposition and (b) histogram of the areas of the clusters grown on the window showing the formation of rather large clusters with different areas. (c) Hologram of the amplitude reconstruction of the window not kept under beam illumination during Pd deposition. (d) histogram of the areas of the clusters formed on the window; in this case, smaller clusters are observed. The scale bar in (a) and (c) corresponds to 100 nm.

4.3.2 Palladium clusters: LEEPS vs TEM

Palladium deposited on free-standing graphene has been shown to give rise to stable clusters. For a comparison with the images obtained by means of LEEPS microscopy, some selected samples have been imaged using TEM, which is commonly used for the study 2D materials. Here, only the acquisitions for the sample discussed in the previous subsection are reported, as they provide a better understanding of Pd cluster growth on free-standing graphene in the presence of a low-energy electron beam.

Samples have been prepared and imaged using LEEPS microscopy. They have been imaged again before TEM investigation one to five days after Pd deposition to check the stability of clusters. Soon after, the samples have been removed from the LEEPS microscope and inserted in the TEM. During this procedure, it has been necessary to expose samples to air. The TEM used is a Philips CM100 equipped with a Gatan Orius 1000 CCD camera[5] operated with an acceleration voltage of 80 kV (located at the Microscopy Center at the University of Zurich). The 80 kV electron beam acceleration voltage has been chosen to reduce knock-on damage to the graphene [56].

In Figure 4.15 the amplitude and phase reconstructions of the holograms shown in Figure 4.13a-b are compared with the TEM images of the same area. The overall shape of the clusters imaged using LEEPS microscopy can be identified in the TEM acquisitions, although their appearance is quite different. In LEEPS amplitude reconstructions, big islands can be identified (Figure 4.15a-c). In the TEM images, these can be recognized as a number of small clusters exhibiting an area of a few nm^2 and arranged over the shape of the islands imaged using LEEPS. For comparison, a nearby window on which Pd has been deposited without the presence of the electron beam has been also imaged. The TEM image in Figure 4.16a shows the presence of small clusters indicated by a higher contrast and an area in the order of tens of nm^2 (Figure 4.16b), that can form agglomerates of a few clusters. In all the TEM images, the graphene membrane exhibits a thin layer of contaminants likely the result of atmospheric contaminations that occurred during the transfer between the two microscopes.

The acquired TEM and LEEPS images are 2D projections of the sample and therefore no information on cluster thickness can be obtained from them. Nevertheless, some indication can be obtained from the comparison of the images acquired with these two

[5]The features of the CCD are: dimensions 4k × 2.6k pixels, 14-bit depth, pixel size of 9 μm, and exposure time between 1 ms and 1000 s.

microscopy techniques. The reconstructions of LEEPS holograms (Figure 4.15a-c) show large compact islands, while the TEM images show agglomerates of small clusters. These agglomerates cover the same area of the islands identified by LEEPS measures (Figure 4.15b-d). The presence of small clusters could be due to thicker Pd areas or to areas on the island with a different reactivity to atmospheric contamination and contamination from the TEM column. This result can be explained by considering the inelastic mean free path $\lambda(E)$ of electrons in Pd, which amounts to $\lambda(80\text{ keV})$=527.3 Å for the electron beam energy of TEM and to just $\lambda(60\text{ eV})$=4.1 Å [250] for the electron energy used in the LEEPS acquisition. As an example, 1-nm thick Pd film would lead to a 92% reduction in impinging electron intensity when imaged using the LEEPS microscope with 60 eV electrons, resulting in an opaque object. The same film in the TEM with 80 keV electrons would lead to a reduction in the primary electron beam of only 2%. Therefore, the LEEPS microscope is capable to detect extremely thin Pd layers that would be transparent to a typical TEM electron beam. The Pd clusters shown in Figure 4.15a-c are thus too thin to be properly imaged using TEM. The same considerations can be extended to the clusters grown on the window not imaged during Pd deposition. In the previous section, the formation of clusters with a mean area of 141 nm^2 has been reported for the windows not exposed to the electron beam. The TEM images for such windows, as the acquisition reported in Figure 4.16a, exhibit clusters with an area of one order of magnitude smaller with respect to the areas estimated from LEEPS acquisitions. Moreover, it should be noted that the clusters shown in Figure 4.16a are larger than the clusters shown in Figure 4.15a-c, that are characterised by an area lower than 6 nm^2. This may be due to thicker Pd clusters, explaining the 2.7 times lower total area of the clusters seen in Figure 4.14c compared to the one measured in Figure 4.14a.

4.4 Cesium nucleation on Palladium clusters

It has been shown in the previous experiments that pre-existing adsorbates act as a favoured nucleation site and as an anchor for alkali metal deposited atoms. In this section, the effect of Pd clusters on Cs deposition is investigated on free-standing single layer graphene under controlled experimental conditions.

A window of extremely clean graphene has been selected, that is a window not exhibiting pre-existing stable clusters originating from the sample preparation procedure. This

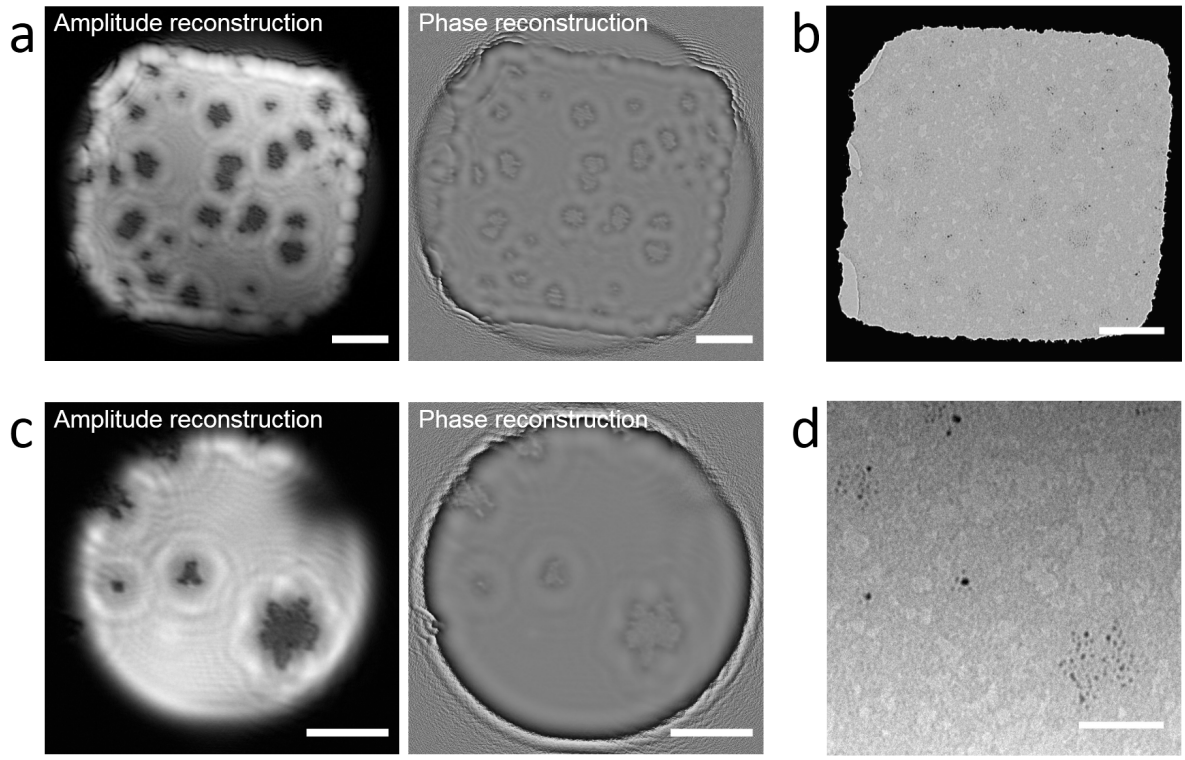

Figure 4.15: Comparison between LEEPS reconstructions and TEM images. (a) Amplitude and phase reconstructions of the hologram shown in Figure 4.13a, and (b) TEM acquisition of the same graphene window. TEM image acquired at 80 kV and with a magnification of 93k. The scale bars correspond to 100 nm. (c) Amplitude and phase reconstructions of the hologram shown in Figure 4.13b, and (d) TEM image of the same region of interest acquired at 80 kV and with a magnification of 180k. The scale bars correspond to 50 nm.

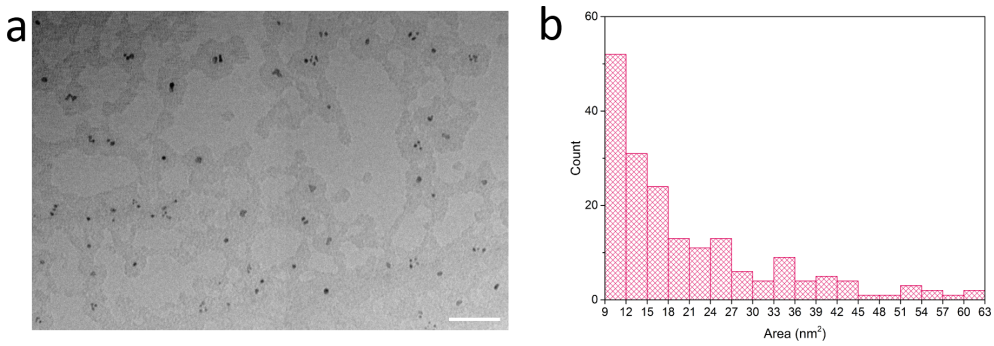

Figure 4.16: Pd clusters deposited without imaging the sample during the deposi- tion. (a) TEM image of a window adjacent to the one reported in Figure 4.15. The scale bar corresponds to 50 nm. (b) Area distribution of the clusters shown in (a).

precaution ensures that only Pd clusters grown in situ are present. The Pd deposition has been performed operating the evaporator at a current of 5 A for 5 min. The cluster growth has been monitored continuously, keeping the sample under the electron beam. In this way, as shown in subsection 4.3.1, clusters exhibiting a wide area distribution can be formed. In this case, 15 clusters with areas ranging from $25\,\mathrm{nm}^2$ to $569\,\mathrm{nm}^2$ over a $500 \times 500\,\mathrm{nm}^2$ graphene window have been obtained, with the mean area being $130\,\mathrm{nm}^2$. Cs has been deposited subsequently, powering the evaporator with a current of 5.2 A. The Cs dispenser has been degassed for a long time and the St 101 alloy regenerated[6] before starting the deposition, in such a way that a degassing time of only a few minutes has been necessary to clean the dispenser before Cs deposition. Cs deposition has been performed monitoring the ROI continuously using an electron beam energy of 47 eV.

Figure 4.17 shows holograms acquired at different times during Cs deposition. The first hologram shows Pd clusters deposited on graphene, with two clusters of interest indicated. Cluster A, indicated by the red arrow, has an area of $440\,\mathrm{nm}^2$ while cluster B, indicated by the yellow arrow, has an area of $30\,\mathrm{nm}^2$. The evolution of Cs deposition shows different features for these two clusters. At $t = 90\,\mathrm{s}$, a small amount of Cs is nucleated on A, that still resembles its hologram at $t = 0$. Cluster B shows a bright spot, the intensity of which increased at $t = 295\,\mathrm{s}$. Cluster A, instead, shows four bright spots. It should be noted that the Cs adatom close to the cluster B exhibits an elliptical-shaped bright spot, indicating that the amount of charge localized on B is enough for this bright spot to be

[6] As detailed in section 3.2.2, this procedure is necessary for a pure alkali metal vapour release from the AMD used.

distorted. Above 414 s of deposition, a significant amount of Cs adatoms can be found between clusters. The last hologram in Figure 4.17 reports the cluster B after 567 s of Cs deposition.

From these experimental observations it can be concluded that the Cs deposition proceeds with the nucleation of Cs on Pd clusters until saturation, after which Cs adatoms can be observed on the clean graphene areas between clusters. However, the distribution of such adsorbates can be influenced by the presence of a nearby charged cluster, as shown in the last hologram of Figure 4.17. In the case of small Pd clusters like the cluster B reported here, Cs adatoms are typically radially arranged with respect to clusters. Moreover, such adatoms exhibit an asymmetric bright spot on the detector, likely due to the influence of the cluster strong localised charge on the trajectories of the probing electrons scattered off by Cs ions.

The presence of pre-existing clusters of well-defined size and position on graphene could be used as a route for the controlled adsorption of alkali metals that would stick to these clusters in a stable way, thus circumventing eventual issues in practical applications that could arise from the high mobility of alkali metals on graphene.

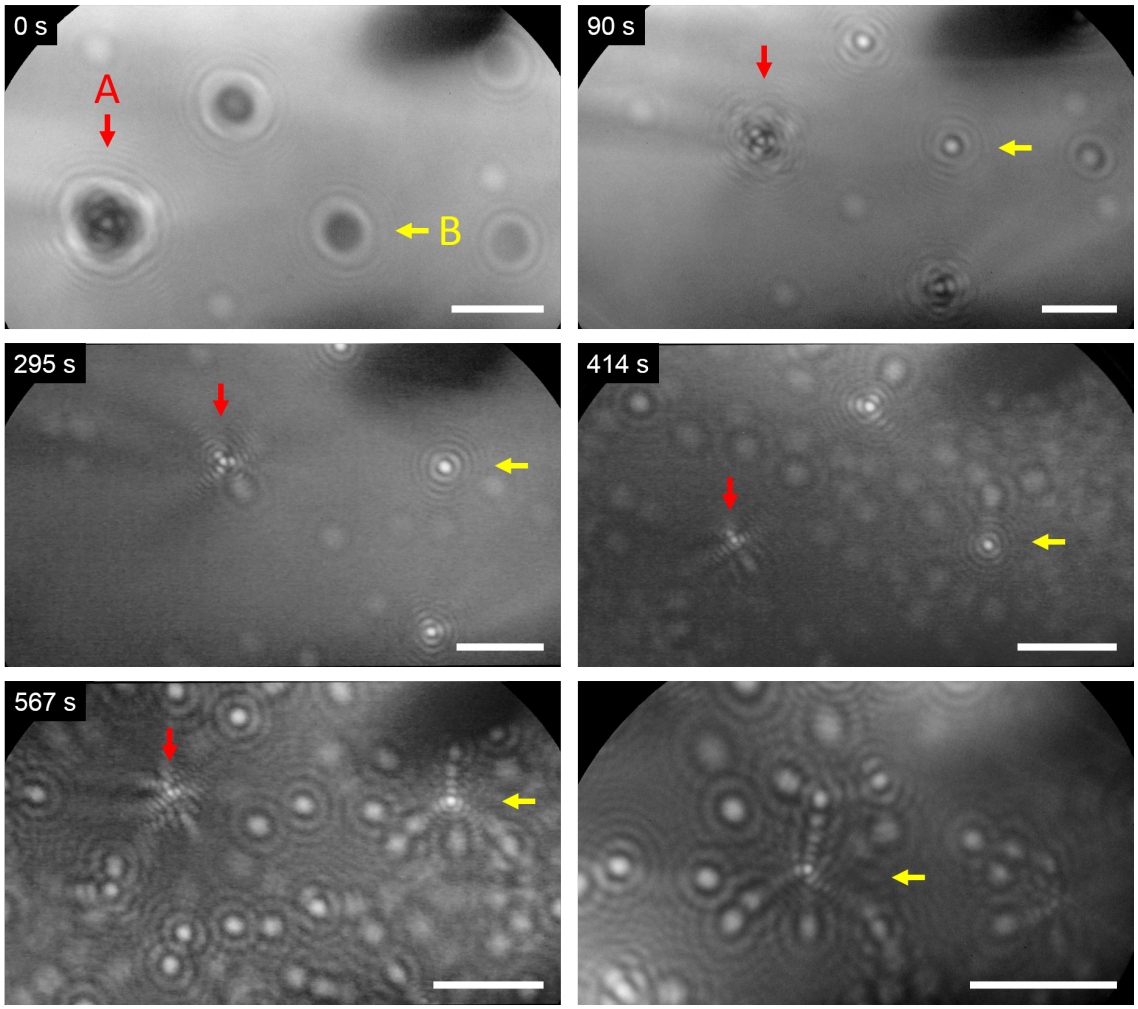

Figure 4.17: Evolution of Cs deposition on graphene supported Pd clusters. The first hologram shows Pd clusters. The red and the yellow arrows track two such clusters (A and B, respectively) during Cs deposition. The last hologram is a magnified image of the cluster identified by the yellow arrow at the end of the deposition. All holograms have been acquired with an electron beam energy of 47 eV, except for the last one that has been acquired with electron beam energy of 34 eV. All holograms are distortion-corrected, and the scale bar corresponds to 50 nm.

Chapter 5

Conclusions and Outlook

This thesis reports the first in situ direct observation of individual alkali metal adsorption events on single-layer and intercalation into bilayer graphene by mean of a dedicated LEEPS microscope.

The adsorption of Cs, K and Li on free-standing single-layer graphene has been reported in section 4.1. The resulting positively charged alkali ion is identified by a bright spot in the image. An interesting effect has been observed after the deposition has been interrupted: the amount of Cs and K rapidly decreases, while a Li adatom tends to persist on the adsorption site. However, whether Cs and K migrate towards the graphene window frame, where there is an interface with the Pd covered substrate, sticking on the Pd supported graphene and eventually intercalating, or desorb is still an open question that could not be addressed with the setup and investigation techniques employed in this work.

The intercalation of alkali metals into bilayer graphene has been investigated by selecting sample areas exhibiting both single-layer and bilayer domains. It is conceivable that the intercalation at the step edge between the two domains proceeds much like in the case of graphite. The evolution of Li and K deposition has shown that the density of alkali ions on the bilayer domain increases more rapidly than on the single layer graphene during the deposition, indicating that the atoms of the two species intercalate into the bilayer domain. Once the deposition of K respectively Cs has been stopped an equilibrium distribution with a higher particle density in the bilayer domain evolved. The calculated value for the difference of the free energy of binding between these two binding states for K amounts to $\Delta E = (0.08 \pm 0.01)\,\mathrm{eV}$, indicating the adsorption on single-layer graphene as the energetically less favourable state. In the case of Li, the formation of stable adsor-

bates has been observed. A control experiment with Pd has shown no intercalation in the bilayer domain.

The effect of the electron beam during Pd deposition has also been investigated and its consequence for the nucleation process of Pd clusters. The comparison between the ROI imaged during the deposition and an adjacent window imaged only before and after the deposition has led to significant differences. The clusters grown on the graphene window illuminated by the electron beam are characterised by a wider area, a broader size distribution, and a lower cluster density compared to those grown on the window which has not been continuously illuminated by the electron beam. The explanation for the formation of larger clusters relies in the emission of secondary electrons from the adsorbed Pd upon electron beam exposure. Such inelastic processes cause local heating promoting the nucleation on the side of the already formed islands by locally enhanced diffusion. These samples have also been imaged in a TEM for a comparison with the LEEPS results. A big cluster imaged by LEEPS can be recognised in TEM acquisitions as a group of much smaller features distributed on the same area. This difference is related to the different inelastic mean free path of the probing electrons of these two techniques, being two orders of magnitude larger for the 80 keV electrons of the TEM with respect to the 60 eV electrons of the LEEPS microscope. Therefore, LEEPS microscopy allows to image thin samples that would be transparent in TEM imaging.

The last investigation, presented in section 4.4 of this work, concerns the deposition of Cs on Pd clusters of different size. The evolution of Cs deposition has shown that Pd clusters are preferred adsorption sites for Cs atoms. The nucleation around Pd clusters proceeded until a saturation point has been reached, after which Cs got adsorbed between these charged clusters. It has been observed that the intensity of the charged clusters, and thus the amount of adsorbed Cs, did not decrease once the deposition has been stopped. This result suggests that pre-existing clusters on free-standing graphene can thus be successfully used as anchors for stable adsorption of alkali metal atoms. These findings could represent a route for practical applications in the field of nanoelectronics where the use of doped graphene might represent a viable solution. However, for such applications a systematic study of the electronic properties of graphene doped by alkali metal deposition on uniformly sized clusters as a function of cluster size and cluster density would be necessary.

Despite the results reported in this work on alkali metal intercalation into bilayer free-

standing graphene through the interface with the single layer domain, a study of intercalation through the graphene surface is still an open question. In particular, alkali metal deposition performed on a sample with the step edge exposed towards the tip would be necessary to investigate whether and under which conditions intercalation occurs through the first graphene layer and, thus, to compare the outcome with the results reported in the literature on supported bilayer graphene. Moreover, the study on alkali metals deposited on free-standing graphene needs to be completed with the deposition of Na that, differently from the investigated Cs, K and Li, is expected not to intercalate through the step edge.

The findings reported in this thesis demonstrate that LEEPS microscopy can open new opportunities for investigating adsorption and intercalation phenomena on free-standing graphene. A future development of LEEPS microscopy might be in merging the capabilities of this technique with the information obtained by a four-point transport measurements of the sample revealing the conductivity during alkali metal deposition; it would thus be possible to compare the transport properties with the adsorbed or intercalated phase identified in the corresponding images. In addition, the possibility to change the temperature of the sample can provide further insight on the energetics involved. The improvement of the temporal resolution would be desirable to access the dynamics of alkali metal adsorbates on free-standing graphene.

Appendix A

Simulations of the probing electron trajectories deflected by an ion on graphene

The following section reports simple electrostatic simulations showing some difference in the deflection of the probing electron trajectories from an adsorbed ion and an intercalated one. Unfortunately, from the experimental data, we are not able to distinguish adsorbed from intercalated atoms. This discrepancy between simulations and experimental data may be due to our oversimplified model that does not consider a realistic charge redistribution. DFT simulations would be helpful in this sense.

The electron trajectory path has been calculated solving the equation of motion:

$$m\ddot{\vec{r}} = -e\vec{E}(\vec{r})$$

where m is the mass of the electron, e is the elementary charge, and $\vec{E}(\vec{r})$ is the electric field distribution. The electric field distribution is related to the potential distribution $V(\vec{r})$ generated by the charged particle through:

$$\vec{E}(\vec{r}) = -\nabla V(\vec{r}) \tag{A.1}$$

The calculation of $\vec{E}(\vec{r})$ can be performed describing $V(\vec{r})$ generated by an ion adsorbed on graphene or intercalated in the bilayer graphene domain with the charges images method.

A.1 Adsorbed ion

The ion on single layer graphene has been modelled as a point-like positive charge $q = +e$ at a distance h from an infinite conductive plane. The values for h are 1.7 Å for Li and 2.7 Å for K [139]. The potential from the charge images method is:

$$V(\vec{r}) = \frac{q}{4\pi\varepsilon_0}\left(\frac{1}{\sqrt{x^2+y^2+(z-h)^2}} - \frac{1}{\sqrt{x^2+y^2+(z+h)^2}}\right) \quad \text{for } z > 0$$

$$V(\vec{r}) = 0 \quad \text{for } z \leq 0$$

The electric field is given by equation A.1. For the rotational symmetry of the problem, only the x and z direction are considered:

$$E_x(x,z) = \frac{q\ x}{4\pi\varepsilon_0}\left(\frac{1}{\left(x^2+(z-h)^2\right)^{\frac{3}{2}}} - \frac{1}{\left(x^2+(z+h)^2\right)^{\frac{3}{2}}}\right) \quad \text{for } z > 0$$

$$E_z(x,z) = -\frac{q}{4\pi\varepsilon_0}\left(\frac{z+h}{\left(x^2+(z+h)^2\right)^{3/2}} - \frac{z-h}{\left(x^2+(z-h)^2\right)^{3/2}}\right) \quad \text{for } z > 0$$

The simulated trajectories for K and Li ions are shown in Figure A.1a and Figure A.2b, respectively. An ion adsorbed on the surface of the bilayer graphene can be modelled by a point-like positive charge at a distance h above two infinite conductive planes both at ground potential. The solution to this electrostatic problem is identical to the one for the single layer derived above since the image charge would be at the very same position. According to this simple electrostatic model, a charge on single layer and on bilayer graphene would give rise to the same deflection imposed on the probing electrons.

A.2 Intercalated ion

The intercalated ion has been modelled as a point-like positive charge $q = +e$ placed midway (at $z = 0$) between two infinite grounded conductive planes at $z = -d_{\text{int}}/2$ and $z = +d_{\text{int}}/2$, where d_{int} is the interlayer distance between the intercalated graphene layers. According to Kaneko *et al.* [139], $d_{\text{int}} = 3.6$ Å) for Li and $d_{\text{int}} = 5.4$ Å) for K. The potential

calculated by the method of image charges is given by the sum of an infinite number of mirror charges between the planes [251]:

$$V(\vec{r}) = \frac{q}{4\pi\varepsilon_0} \sum_{n=-\infty}^{\infty} \frac{(-1)^n}{\sqrt{x^2 + y^2 + (z - n\ d_{\text{int}})^2}} \quad \text{for } -d_{\text{int}} < z < d_{\text{int}}$$

$$V(\vec{r}) = 0 \quad \text{for } z \leq -d_{\text{int}} \text{ and } z \geq d_{\text{int}}$$

Considering again for symmetry reasons only the x and z directions, the electric field is given by:

$$E_x(x,z) = \frac{q}{4\pi\varepsilon_0} \sum_{n=-\infty}^{\infty} \frac{(-1)^n\ x}{(x^2 + (z - n\ d_{\text{int}})^2)^{3/2}} \quad \text{for } -d_{\text{int}} < z < d_{\text{int}}$$

$$E_z(x,z) = \frac{q}{4\pi\varepsilon_0} \sum_{n=-\infty}^{\infty} \frac{(-1)^n (z - n\ d_{\text{int}})}{(x^2 + (z - n\ d_{\text{int}})^2)^{3/2}} \quad \text{for } -d_{\text{int}} < z < d_{\text{int}}$$

In the simulations shown in Figure A.1b for K and Figure A.2b for Li, the sum runs from $n = -1000$ to $n = 1000$.

The comparison between the probing electron trajectories deflected by an adsorbed ion and an intercalated ion are reported in Figure A.1c and Figure A.2c for K and Li, respectively. It is evident that for both metals an adsorbed ion deflects an electron trajectory more than an intercalated one.

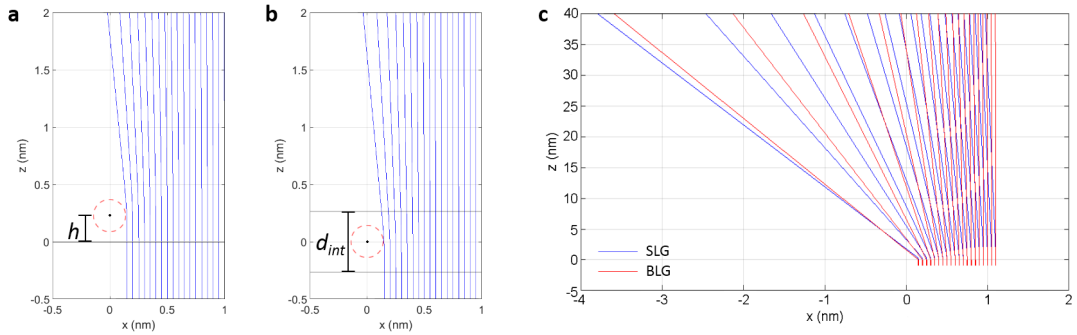

Figure A.1: Simulations of electron trajectories in the presence of a charged K ion on single layer graphene and intercalated in bilayer graphene using the potential calculated with the method of image charges. In accordance with typical experimental conditions, 80 eV electrons were used for the simulations. (a) The K ion adsorbed on single layer graphene has been modelled as a point-like charge +e placed at a distance h=2.7 Å from a conductive infinite plane, represented by the black line in the picture. (b) The K ion intercalated in bilayer graphene has been modelled as a point-charge placed midway between two infinite parallel conducive planes at a distance $d_{\text{int}} = 5.4$ Å from each other (depicted as two black lines). The red dashed circle in (a) and (b) indicates the size of the K ion, which has an ionic radius of 152 pm. (c) Comparison between the trajectory deflection for an adsorbed (blue line) and an intercalated (red line) ion. The values of h and d_{int} used here have been calculated by Kaneko *et al.* [139].

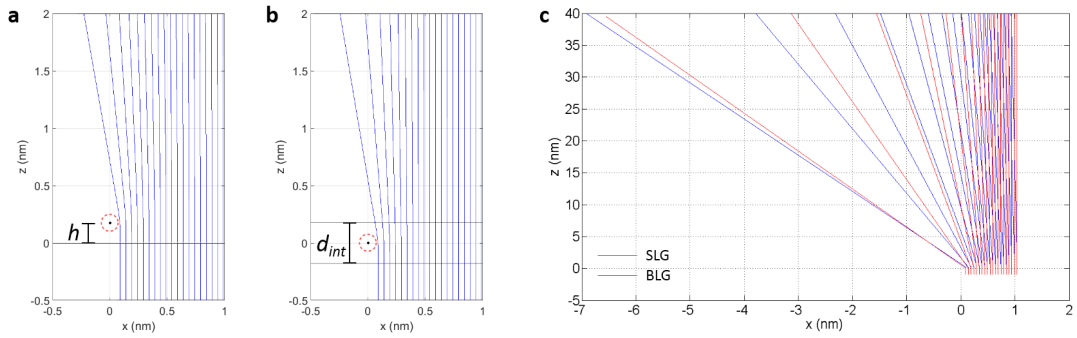

Figure A.2: Simulations of electron trajectories in the presence of a charged Li ion on single layer graphene and intercalated in bilayer graphene using the potential calculated with the method of image charges. In accordance with typical experimental conditions, 80 eV electrons were used for the simulations. (a) The Li ion adsorbed on single layer graphene has been modelled as a point-like charge +e placed at a distance h=1.7 Å from a conductive infinite plane, represented by the black line in the picture. (b) The Li ion intercalated in bilayer graphene has been modelled as a point-charge placed midway between two infinite parallel conducive planes at a distance $d_{\mathrm{int}} = 3.6$ Å from each other (depicted as two black lines). The red dashed circle in (a) and (b) indicates the size of the Li ion, which has an ionic radius of 90 pm. (c) Comparison between the trajectory deflection for an adsorbed (blue line) and an intercalated (red line) ion. The values of h and d_{int} used here have been calculated by Kaneko *et al.* [139].

Appendix B

Li cluster dynamics in the bilayer graphene domain

After having deposited Li on two adjacent domains of bilayer and single layer graphene, a movie of the ROI has been acquired after more than 1 minute from the end of the deposition. While the clusters formed on the single layer domain do not exhibit any motion, some features on the bilayer domain exhibit some mobility. The dynamics of 17 features, indicated by arrows in Figure B.1a, on a bilayer graphene domain area of $6.5 \times 10^3\,\mathrm{nm}^2$ has been analysed at the frame rate resolution of 40 ms over a time of 3 s. The motion of such features can be described as a hopping between 2 to 5 sites (Figure B.1b). The square root of their mean square displacement, $\sqrt{\langle r^2 \rangle}$, on subsequent frames has been found to be about 10 nm per second with a mean jumping rate of about 5 jumps per second. The plot of the hopping rate versus $\sqrt{\langle r^2 \rangle}$, reported in Figure B.1d, shows no correlation between these two quantities, indicating that no random walk can be assumed for these features. Their motion is strongly influenced and confined by surrounding charged stable features. The observation of some dynamics for features in the bilayer graphene domain could be likely due to the position of such particles in between the bilayer, supporting the hypothesis of intercalation.

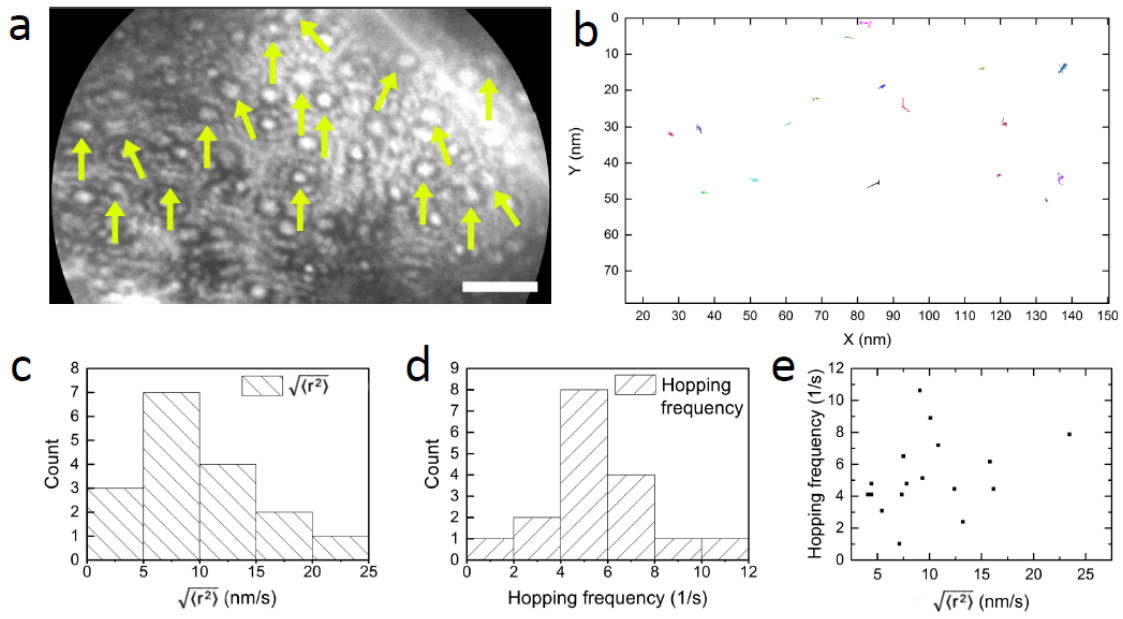

Figure B.1: Li particles dynamics in the bilayer graphene domain. (a) Hologram of particles in the bilayer graphene domain acquired with 80 eV electrons. The motion of the particles indicated by yellow arrows has been investigated. The scale bar corresponds to 20 nm. (b) Trajectories of the particles investigated. (c) Distribution of the square root of their mean square displacement $\sqrt{\langle r^2 \rangle}$ per second. (d) Distribution of the hopping rate. (e) Plot of the hopping rate versus the square root of $\langle r^2 \rangle$ per second. The points are randomly distributed, and therefore no correlation between the two quantities can be identified.

Bibliography

[1] K. S. Novoselov, A. K. Geim, S. V. Morozov, D. Jiang, Y. Zhang, S. V. Dubonos, I. V. Grigorieva, and A. A. Firsov, "Electric Field Effect in Atomically Thin Carbon Films," *Science*, vol. 306, no. 5696, pp. 666–669, 2004.

[2] R. E. Peierls, "Quelques Proprietes Typiques des Corps Solides," *Ann. I. H. Poincare*, vol. 5, no. 3, pp. 177–222, 1935.

[3] L. D. Landau and E. M. Lifshitz, *Statistical Physics, Part I.* Pergamon Press: Oxford, 1980.

[4] N. D. Mermin and H. Wagner, "Absence of Ferromagnetism or Antiferromagnetism in One- or Two-Dimensional Isotropic Heisenberg Models," *Physical Review Letters*, vol. 17, no. 22, pp. 1133–1136, 1966.

[5] N. D. Mermin, "Crystalline Order in Two Dimensions," *Physical Review*, vol. 176, no. 1, pp. 250–254, 1968.

[6] A. O'Hare, F. V. Kusmartsev, and K. I. Kugel, "A Stable "Flat" Form of Two-Dimensional Crystals: Could Graphene, Silicene, Germanene Be Minigap Semiconductors?," *Nano Letters*, vol. 12, no. 2, pp. 1045–1052, 2012.

[7] A. Fasolino, J. H. Los, and M. I. Katsnelson, "Intrinsic Ripples in Graphene," *Nature Materials*, vol. 6, no. 11, pp. 858–861, 2007.

[8] J. C. Meyer, A. K. Geim, M. I. Katsnelson, K. S. Novoselov, T. J. Booth, and S. Roth, "The Structure of Suspended Graphene Sheets," *Nature*, vol. 446, no. 7131, pp. 60–63, 2007.

[9] A. E. Morgan and G. A. Somorjai, "Low Energy Electron Diffraction Studies of Gas Adsorption on the Platinum (100) Single Crystal Surface," *Surface Science*, vol. 12, no. 3, pp. 405–425, 1968.

[10] J. W. May, "Platinum Surface LEED Rings," *Surface Science*, vol. 17, no. 1, pp. 267–270, 1969.

[11] J. Coraux, A. T. N'Diaye, C. Busse, and T. Michely, "Structural Coherency of Graphene on Ir(111)," *Nano Letters*, vol. 8, no. 2, pp. 565–570, 2008.

[12] P. W. Sutter, J.-I. Flege, and E. A. Sutter, "Epitaxial Graphene on Ruthenium," *Nature Materials*, vol. 7, no. 5, pp. 406–411, 2008.

[13] K. S. Kim, Y. Zhao, H. Jang, S. Y. Lee, J. M. Kim, K. S. Kim, J.-H. Ahn, P. Kim, J.-Y. Choi, and B. H. Hong, "Large-Scale Pattern Growth of Graphene Films for Stretchable Transparent Electrodes," *Nature*, vol. 457, no. 7230, pp. 706–710, 2009.

[14] A. Reina, X. Jia, J. Ho, D. Nezich, H. Son, V. Bulovic, M. S. Dresselhaus, and J. Kong, "Large Area, Few-Layer Graphene Films on Arbitrary Substrates by Chemical Vapor Deposition," *Nano Letters*, vol. 9, no. 1, pp. 30–35, 2009.

[15] X. Li, W. Cai, J. An, S. Kim, J. Nah, D. Yang, R. Piner, A. Velamakanni, I. Jung, E. Tutuc, S. K. Banerjee, L. Colombo, and R. S. Ruoff, "Large-Area Synthesis of High-Quality and Uniform Graphene Films on Copper Foils," *Science*, vol. 324, no. 5932, pp. 1312–1314, 2009.

[16] C. Mattevi, H. Kim, and M. Chhowalla, "A Review of Chemical Vapour Deposition of Graphene on Copper," *J. Mater. Chem.*, vol. 21, no. 10, pp. 3324–3334, 2011.

[17] M. Batzill, "The Surface Science of Graphene: Metal Interfaces, CVD Synthesis, Nanoribbons, Chemical Modifications, and Defects," *Surface Science Reports*, vol. 67, no. 3-4, pp. 83–115, 2012.

[18] A. K. Geim and K. S. Novoselov, "The Rise of Graphene," *Nature Materials*, vol. 6, no. 3, pp. 183–191, 2007.

[19] J.-H. Chen, C. Jang, S. Xiao, M. Ishigami, and M. S. Fuhrer, "Intrinsic and Extrinsic Performance Limits of Graphene Devices on SiO_2," *Nature Nanotechnology*, vol. 3, no. 4, pp. 206–209, 2008.

[20] A. Akturk and N. Goldsman, "Electron Transport and Full-Band Electron-Phonon Interactions in Graphene," *Journal of Applied Physics*, vol. 103, no. 5, p. 053702, 2008.

[21] K. I. Bolotin, K. J. Sikes, Z. Jiang, M. Klima, G. Fudenberg, J. Hone, P. Kim, and H. L. Stormer, "Ultrahigh Electron Mobility in Suspended Graphene," *Solid State Communications*, vol. 146, no. 9-10, pp. 351–355, 2008.

[22] A. H. Castro Neto, N. M. R. Peres, K. S. Novoselov, A. K. Geim, and F. Guinea, "The Electronic Properties of Graphene," *Reviews of Modern Physics*, vol. 81, no. 1, pp. 109–162, 2009.

[23] K. S. Novoselov, A. K. Geim, S. V. Morozov, D. Jiang, M. I. Katsnelson, I. V. Grigorieva, S. V. Dubonos, and A. A. Firsov, "Two-Dimensional Gas of Massless Dirac Fermions in Graphene," *Nature*, vol. 438, no. 7065, pp. 197–200, 2005.

[24] A. K. Geim, "Graphene: Status and Prospects," *Science*, vol. 324, no. 5934, pp. 1530–1534, 2009.

[25] Z. Luo, T. Yu, K.-J. Kim, Z. Ni, Y. You, S. Lim, Z. Shen, S. Wang, and J. Lin, "Thickness-Dependent Reversible Hydrogenation of Graphene Layers," *ACS Nano*, vol. 3, no. 7, pp. 1781–1788, 2009.

[26] F. Schedin, A. K. Geim, S. V. Morozov, E. W. Hill, P. Blake, M. I. Katsnelson, and K. S. Novoselov, "Detection of Individual Gas Molecules Adsorbed on Graphene," *Nature Materials*, vol. 6, no. 9, pp. 652–655, 2007.

[27] Y. Liu, B. Xie, Z. Zhang, Q. Zheng, and Z. Xu, "Mechanical Properties of Graphene Papers," *Journal of the Mechanics and Physics of Solids*, vol. 60, no. 4, pp. 591–605, 2012.

[28] E. Pop, V. Varshney, and A. K. Roy, "Thermal Properties of Graphene: Fundamentals and Applications," *MRS Bulletin*, vol. 37, no. 12, pp. 1273–1281, 2012.

[29] R. R. Nair, P. Blake, J. R. Blake, R. Zan, S. Anissimova, U. Bangert, A. P. Golovanov, S. V. Morozov, A. K. Geim, K. S. Novoselov, and T. Latychevskaia, "Graphene as a Transparent Conductive Support for Studying Biological Molecules by Transmission Electron Microscopy," *Applied Physics Letters*, vol. 97, no. 15, p. 153102, 2010.

[30] R. Zan, U. Bangert, Q. Ramasse, and K. S. Novoselov, "Interaction of Metals with Suspended Graphene Observed by Transmission Electron Microscopy," *The Journal of Physical Chemistry Letters*, vol. 3, no. 7, pp. 953–958, 2012.

[31] J.-N. Longchamp, C. Escher, T. Latychevskaia, and H.-W. Fink, "Low-Energy Electron Holographic Imaging of Gold Nanorods Supported by Ultraclean Graphene," *Ultramicroscopy*, vol. 145, pp. 80–84, 2014.

[32] J.-N. Longchamp, T. Latychevskaia, C. Escher, and H.-W. Fink, "Low-Energy Electron Holographic Imaging of Individual Tobacco Mosaic Virions," *Applied Physics Letters*, vol. 107, no. 13, p. 133101, 2015.

[33] J.-N. Longchamp, S. Rauschenbach, S. Abb, C. Escher, T. Latychevskaia, K. Kern, and H.-W. Fink, "Imaging Proteins at the Single-Molecule Level," *Proceedings of the National Academy of Sciences*, vol. 114, no. 7, pp. 1474–1479, 2017.

[34] X. Liu, C.-Z. Wang, M. Hupalo, H.-Q. Lin, K.-M. Ho, and M. Tringides, "Metals on Graphene: Interactions, Growth Morphology, and Thermal Stability," *Crystals*, vol. 3, no. 1, pp. 79–111, 2013.

[35] D. C. Elias, R. R. Nair, T. M. G. Mohiuddin, S. V. Morozov, P. Blake, M. P. Halsall, A. C. Ferrari, D. W. Boukhvalov, M. I. Katsnelson, A. K. Geim, and K. S. Novoselov, "Control of Graphene's Properties by Reversible Hydrogenation: Evidence for Graphane," *Science*, vol. 323, no. 5914, pp. 610–613, 2009.

[36] J. T. Robinson, J. S. Burgess, C. E. Junkermeier, S. C. Badescu, T. L. Reinecke, F. K. Perkins, M. K. Zalalutdniov, J. W. Baldwin, J. C. Culbertson, P. E. Sheehan, and E. S. Snow, "Properties of Fluorinated Graphene Films," *Nano Letters*, vol. 10, no. 8, pp. 3001–3005, 2010.

[37] S.-H. Cheng, K. Zou, F. Okino, H. R. Gutierrez, A. Gupta, N. Shen, P. C. Eklund, J. O. Sofo, and J. Zhu, "Reversible Fluorination of Graphene: Evidence of a Two-Dimensional Wide Bandgap Semiconductor," *Physical Review B*, vol. 81, no. 20, p. 205435, 2010.

[38] T. Eelbo, M. Waśniowska, P. Thakur, M. Gyamfi, B. Sachs, T. O. Wehling, S. Forti, U. Starke, C. Tieg, A. I. Lichtenstein, and R. Wiesendanger, "Adatoms and Clusters of 3*d* Transition Metals on Graphene: Electronic and Magnetic Configurations," *Physical Review Letters*, vol. 110, no. 13, p. 136804, 2013.

[39] X. Hong, K. Zou, B. Wang, S.-H. Cheng, and J. Zhu, "Evidence for Spin-Flip Scattering and Local Moments in Dilute Fluorinated Graphene," *Physical Review Letters*, vol. 108, no. 22, p. 226602, 2012.

[40] B. Uchoa and A. H. Castro Neto, "Superconducting States of Pure and Doped Graphene," *Physical Review Letters*, vol. 98, no. 14, 2007.

[41] G. Profeta, M. Calandra, and F. Mauri, "Phonon-Mediated Superconductivity in Graphene by Lithium Deposition," *Nature Physics*, vol. 8, no. 2, pp. 131–134, 2012.

[42] R. Nandkishore, L. S. Levitov, and A. V. Chubukov, "Chiral Superconductivity from Repulsive Interactions in Doped Graphene," *Nature Physics*, vol. 8, no. 2, pp. 158–163, 2012.

[43] J. A. Flores-Livas and A. Sanna, "Superconductivity in Intercalated Group-IV Honeycomb Structures," *Physical Review B*, vol. 91, no. 5, p. 054508, 2015.

[44] P. A. Khomyakov, G. Giovannetti, P. C. Rusu, G. Brocks, J. van den Brink, and P. J. Kelly, "First-Principles Study of the Interaction and Charge Transfer between Graphene and Metals," *Physical Review B*, vol. 79, no. 19, p. 195425, 2009.

[45] K. T. Chan, J. B. Neaton, and M. L. Cohen, "First-Principles Study of Metal Adatom Adsorption on Graphene," *Physical Review B*, vol. 77, no. 23, pp. 1–12, 2008.

[46] B. Uchoa, C.-Y. Lin, and A. H. Castro Neto, "Tailoring Graphene with Metals on Top," *Physical Review B*, vol. 77, no. 3, p. 035420, 2008.

[47] T. Ohta, A. Bostwick, J. L. McChesney, T. Seyller, K. Horn, and E. Rotenberg, "Interlayer Interaction and Electronic Screening in Multilayer Graphene Investigated with Angle-Resolved Photoemission Spectroscopy," *Physical Review Letters*, vol. 98, no. 20, 2007.

[48] S. Y. Zhou, G.-H. Gweon, A. V. Fedorov, P. N. First, W. A. de Heer, D.-H. Lee, F. Guinea, A. H. Castro Neto, and A. Lanzara, "Substrate-Induced Bandgap Opening in Epitaxial Graphene," *Nature Materials*, vol. 6, no. 10, pp. 770–775, 2007.

[49] J. Wintterlin and M.-L. Bocquet, "Graphene on Metal Surfaces," *Surface Science*, vol. 603, no. 10-12, pp. 1841–1852, 2009.

[50] E. Rotenberg and A. Bostwick, "Superlattice Effects in Graphene on SiC(0001) and Ir(111) Probed by ARPES," *Synthetic Metals*, vol. 210, pp. 85–94, 2015.

[51] E. McCann and V. I. Fal'ko, "Landau-Level Degeneracy and Quantum Hall Effect in a Graphite Bilayer," *Physical Review Letters*, vol. 96, no. 8, p. 086805, 2006.

[52] T. Ohta, A. Bostwick, T. Seyller, K. Horn, and E. Rotenberg, "Controlling the Electronic Structure of Bilayer Graphene," *Science*, vol. 313, no. 5789, pp. 951–954, 2006.

[53] L. Malard, M. Pimenta, G. Dresselhaus, and M. Dresselhaus, "Raman Spectroscopy in Graphene," *Physics Reports*, vol. 473, no. 5-6, pp. 51–87, 2009.

[54] A. C. Ferrari, J. C. Meyer, V. Scardaci, C. Casiraghi, M. Lazzeri, F. Mauri, S. Piscanec, D. Jiang, K. S. Novoselov, S. Roth, and A. K. Geim, "Raman Spectrum of Graphene and Graphene Layers," *Physical Review Letters*, vol. 97, p. 187401, oct 2006.

[55] D. N. Basov, M. M. Fogler, A. Lanzara, F. Wang, and Y. Zhang, "Colloquium : Graphene spectroscopy," *Reviews of Modern Physics*, vol. 86, pp. 959–994, jul 2014.

[56] J. C. Meyer, F. Eder, S. Kurasch, V. Skakalova, J. Kotakoski, H. J. Park, S. Roth, A. Chuvilin, S. Eyhusen, G. Benner, A. V. Krasheninnikov, and U. Kaiser, "Accurate Measurement of Electron Beam Induced Displacement Cross Sections for Single-Layer Graphene," *Phys. Rev. Lett.*, vol. 108, p. 196102, May 2012.

[57] G. Wang, J. Yang, J. Park, X. Gou, B. Wang, H. Liu, and J. Yao, "Facile Synthesis and Characterization of Graphene Nanosheets," *The Journal of Physical Chemistry C*, vol. 112, pp. 8192–8195, jun 2008.

[58] Z. Lee, K.-J. Jeon, A. Dato, R. Erni, T. J. Richardson, M. Frenklach, and V. Radmilovic, "Direct Imaging of SoftHard Interfaces Enabled by Graphene," *Nano Letters*, vol. 9, pp. 3365–3369, sep 2009.

[59] G. Li, A. Luican, and E. Y. Andrei, "Scanning Tunneling Spectroscopy of Graphene on Graphite," *Physical Review Letters*, vol. 102, p. 176804, apr 2009.

[60] H.-W. Fink, W. Stocker, and H. Schmid, "Holography with Low-Energy Electrons," *Physical Review Letters*, vol. 65, no. 10, pp. 1204–1206, 1990.

[61] T. Latychevskaia, F. Wicki, J.-N. Longchamp, C. Escher, and H.-W. Fink, "Direct Observation of Individual Charges and Their Dynamics on Graphene by Low-Energy Electron Holography," *Nano Letters*, vol. 16, no. 9, pp. 5469–5474, 2016.

[62] J. Y. Mutus, L. Livadaru, J. T. Robinson, R. Urban, M. H. Salomons, M. Cloutier, and R. A. Wolkow, "Low-Energy Electron Point Projection Microscopy of Suspended Graphene, the Ultimate 'Microscope Slide'," *New Journal of Physics*, vol. 13, no. 6, p. 063011, 2011.

[63] J.-N. Longchamp, T. Latychevskaia, C. Escher, and H.-W. Fink, "Low-Energy Electron Transmission Imaging of Clusters on Free-Standing Graphene," *Applied Physics Letters*, vol. 101, no. 11, p. 113117, 2012.

[64] M. S. Dresselhaus and G. Dresselhaus, "Intercalation Compounds of Graphite," *Advances in Physics*, vol. 30, no. 2, pp. 139–326, 1981 (reissued: 51, 1, 2002).

[65] X. Liu, C. Z. Wang, M. Hupalo, W. C. Lu, M. C. Tringides, Y. X. Yao, and K. M. Ho, "Metals on Graphene: Correlation between Adatom Adsorption Behavior and Growth Morphology," *Physical Chemistry Chemical Physics*, vol. 14, no. 25, p. 9157, 2012.

[66] A. Varykhalov, J. Sánchez-Barriga, A. M. Shikin, C. Biswas, E. Vescovo, A. Rybkin, D. Marchenko, and O. Rader, "Electronic and Magnetic Properties of Quasifree-standing Graphene on Ni," *Physical Review Letters*, vol. 101, no. 15, p. 157601, 2008.

[67] C. Riedl, C. Coletti, T. Iwasaki, A. A. Zakharov, and U. Starke, "Quasi-Free-Standing Epitaxial Graphene on SiC Obtained by Hydrogen Intercalation," *Physical Review Letters*, vol. 103, no. 24, p. 246804, 2009.

[68] C. Virojanadara, S. Watcharinyanon, A. A. Zakharov, and L. I. Johansson, "Epitaxial Graphene on 6H-SiC and Li Intercalation," *Physical Review B*, vol. 82, no. 20, p. 205402, 2010.

[69] A. Sandin, T. Jayasekera, J. E. Rowe, K. W. Kim, M. Buongiorno Nardelli, and D. B. Dougherty, "Multiple Coexisting Intercalation Structures of Sodium in Epitaxial Graphene-SiC Interfaces," *Physical Review B*, vol. 85, no. 12, p. 125410, 2012.

[70] C. L. Song, B. Sun, Y. L. Wang, Y. P. Jiang, L. Wang, K. He, X. Chen, P. Zhang, X. C. Ma, and Q. K. Xue, "Charge-Transfer-Tnduced Cesium Superlattices on Graphene," *Physical Review Letters*, vol. 108, no. April, pp. 1–5, 2012.

[71] M. Caragiu and S. Finberg, "Alkali Metal Adsorption on Graphite: a Review," *Journal of Physics: Condensed Matter*, vol. 17, pp. R995–R1024, 2005.

[72] S. Watcharinyanon, C. Virojanadara, and L. I. Johansson, "Rb and Cs Deposition on Epitaxial Graphene Grown on 6H-SiC(0001)," *Surface Science*, vol. 605, no. 21-22, pp. 1918–1922, 2011.

[73] A. Bostwick, F. Speck, T. Seyller, K. Horn, M. Polini, R. Asgari, A. H. MacDonald, and E. Rotenberg, "Observation of Plasmarons in Quasi-Freestanding Doped Graphene," *Science*, vol. 328, no. 5981, pp. 999–1002, 2010.

[74] P. Matyba, A. Carr, C. Chen, D. L. Miller, G. Peng, S. Mathias, M. Mavrikakis, D. S. Dessau, M. W. Keller, H. C. Kapteyn, and M. Murnane, "Controlling the Electronic Structure of Graphene Using Surface-Adsorbate Interactions," *Physical Review B*, vol. 92, p. 041407, 2015.

[75] M. Petrović, I. Šrut Rakić, S. Runte, C. Busse, J. T. Sadowski, P. Lazić, I. Pletikosić, Z.-H. Z.-H. Pan, M. Milun, P. Pervan, N. Atodiresei, R. Brako, D. Šokčević, T. Valla, T. Michely, and M. Kralj, "The Mechanism of Caesium Intercalation of Graphene.," *Nature Communications*, vol. 4, p. 2772, 2013.

[76] M. Bianchi, E. D. L. Rienks, S. Lizzit, A. Baraldi, R. Balog, L. Hornekær, and P. Hofmann, "Electron-Phonon Coupling in Potassium-Doped Graphene: Angle-Resolved Photoemission Spectroscopy," *Physical Review B*, vol. 81, no. 4, p. 041403, 2010.

[77] A. Lugo-Solis and I. Vasiliev, "Ab Initio Study of K Adsorption on Graphene and Carbon Nanotubes: Role of Long-Range Ionic Forces," *Physical Review B*, vol. 76, no. 23, p. 235431, 2007.

[78] K.-H. Jin, S.-M. Choi, and S.-H. Jhi, "Crossover in the Adsorption Properties of Alkali Metals on Graphene," *Physical Review B*, vol. 82, pp. 4–7, 2010.

[79] X. Liu, C. Z. Wang, Y. X. Yao, W. C. Lu, M. Hupalo, M. C. Tringides, and K. M. Ho, "Bonding and Charge Transfer by Metal Adatom Adsorption on Graphene," *Physical Review B*, vol. 83, no. 23, pp. 1–12, 2011.

[80] Z. Ji, F. F. Contreras-Torres, A. F. Jalbout, and A. Ramírez-Treviño, "Surface Diffusion and Coverage Effect of Li Atom on Graphene as Studied by Several Density Functional Theory Methods," *Applied Surface Science*, vol. 285, pp. 846–852, 2013.

[81] N. Dimakis, D. Valdez, F. A. Flor, A. Salgado, K. Adjibi, S. Vargas, and J. Saenz, "Density Functional Theory Calculations on Alkali and the Alkaline Ca Atoms Adsorbed on Graphene Monolayers," *Applied Surface Science*, vol. 413, pp. 197–208, 2017.

[82] M. Liu, A. Kutana, Y. Liu, and B. I. Yakobson, "First-Principles Studies of Li Nucleation on Graphene," *The Journal of Physical Chemistry Letters*, vol. 5, no. 7, pp. 1225–1229, 2014.

[83] J. Renard, M. B. Lundeberg, J. A. Folk, and Y. Pennec, "Real-Time Imaging of K Atoms on Graphite: Interactions and Diffusion," *Physical Review Letters*, vol. 106, no. 15, p. 156101, 2011.

[84] X. Liu, C.-Z. Wang, H.-Q. Lin, K. Chang, J. Chen, and K.-M. Ho, "Charge Oscillations and Interaction between Potassium Adatoms on Graphene Studied by First-Principles Calculations," *Physical Review B*, vol. 91, no. 3, p. 035415, 2015.

[85] X. Fan, W. T. Zheng, and J.-L. Kuo, "Adsorption and Diffusion of Li on Pristine and Defective Graphene," *ACS Applied Materials & Interfaces*, vol. 4, no. 5, pp. 2432–2438, 2012.

[86] X. Liu, Y. Han, J. W. Evans, A. K. Engstfeld, R. J. Behm, M. C. Tringides, M. Hupalo, H.-Q. Lin, L. Huang, K.-M. Ho, D. Appy, P. A. Thiel, and C.-Z. Wang, "Growth Morphology and Properties of Metals on Graphene," *Progress in Surface Science*, vol. 90, no. 4, pp. 397–443, 2015.

[87] I. Forbeaux, J. Themlin, and J. Debever, "Heteroepitaxial Graphite on Interface Formation through Conduction-Band Electronic Structure," *Physical Review B*, vol. 58, no. 24, pp. 16396–16406, 1998.

[88] B. Wang, M. Caffio, C. Bromley, H. Fruchtl, and R. Schaub, "Coupling Epitaxy, Chemical Bonding, and Work Function at the Local Scale in Transition Metal-Supported Graphene," *ACS Nano*, vol. 4, no. 10, pp. 5773–5782, 2010.

[89] D. Martoccia, P. R. Willmott, T. Brugger, M. Björck, S. Günther, C. M. Schlepütz, A. Cervellino, S. A. Pauli, B. D. Patterson, S. Marchini, J. Wintterlin, W. Moritz, and T. Greber, "Graphene on Ru(0001): A 25×25 Supercell," *Physical Review Letters*, vol. 101, p. 126102, 2008.

[90] S. Grandthyll, S. Gsell, M. Weinl, M. Schreck, S. Hüfner, and F. Müller, "Epitaxial Growth of Graphene on Transition Metal Surfaces: Chemical Vapor Deposition versus Liquid Phase Deposition," *Journal of Physics: Condensed Matter*, vol. 24, no. 31, p. 314204, 2012.

[91] A. Varykhalov, D. Marchenko, J. Sánchez-Barriga, M. R. Scholz, B. Verberck, B. Trauzettel, T. O. Wehling, C. Carbone, and O. Rader, "Intact Dirac Cones at Broken Sublattice Symmetry: Photoemission Study of Graphene on Ni and Co," *Physical Review X*, vol. 2, p. 041017, 2012.

[92] A. T. N'Diaye, S. Bleikamp, P. J. Feibelman, and T. Michely, "Two-Dimensional Ir Cluster Lattice on a Graphene Moiré on Ir(111)," *Physical Review Letters*, vol. 97, p. 215501, 2006.

[93] P. J. Feibelman, "Pinning of Graphene to Ir(111) by Flat Ir Dots," *Physical Review B*, vol. 77, p. 165419, 2008.

[94] I. Pletikosić, M. Kralj, P. Pervan, R. Brako, J. Coraux, A. T. N'Diaye, C. Busse, and T. Michely, "Dirac Cones and Minigaps for Graphene on Ir(111)," *Physical Review Letters*, vol. 102, p. 056808, 2009.

[95] M. T. Johnson, H. I. Starnberg, and H. P. Hughes, "Electronic Structure of Alkali Metal Overlayers on Graphite," *Surface Science*, vol. 178, no. 1-3, pp. 290–299, 1986.

[96] J. D. White, J. Cui, M. Strauss, R. D. Diehl, F. Ancilotto, and F. Toigo, "He-Scattering Studies of Alkali Metal Overlayers on Graphite," *Surface Science*, vol. 307-309, pp. 1134–1140, 1994.

[97] J. Algdal, M. Breitholtz, T. Kihlgren, S. Å. Lindgren, and L. Walldén, "Electronic Structure and Growth of K, Rb, and Cs Monolayers on Graphite Studied by Photoemission," *Physical Review B*, vol. 73, pp. 1–10, 2006.

[98] Z. P. Hu and A. Ignatiev, "Lithium Adsorption on the Graphite (0001) Surface," *Physical Review B*, vol. 30, no. 8, pp. 4856–4859, 1984.

[99] M. Gleeson, B. Kasemo, and D. Chakarov, "Thermal and Adsorbate Induced Plasmon Energy Shifts in Graphite," *Surface Science*, vol. 524, no. 1-3, pp. L77–L83, 2003.

[100] F. Valencia, A. H. Romero, F. Ancilotto, and P. L. Silvestrelli, "Lithium Adsorption on Graphite from Density Functional Theory Calculations," *The Journal of Physical Chemistry B*, vol. 110, no. 30, pp. 14832–14841, 2006. PMID: 16869593.

[101] J. S. Bunch, S. S. Verbridge, J. S. Alden, A. M. van der Zande, J. M. Parpia, H. G. Craighead, and P. L. McEuen, "Impermeable Atomic Membranes from Graphene Sheets," *Nano Letters*, vol. 8, no. 8, pp. 2458–2462, 2008.

[102] V. Berry, "Impermeability of Graphene and Its Applications," *Carbon*, vol. 62, pp. 1–10, 2013.

[103] L. Tsetseris and S. T. Pantelides, "Graphene: an Impermeable or Selectively Permeable Membrane for Atomic Species?," *Carbon*, vol. 67, pp. 58–63, 2014.

[104] A. Nagashima, N. Tejima, and C. Oshima, "Electronic States of the Pristine and Alkali-Metal-Intercalated Monolayer Graphite/Ni(111) Systems," *Physical Review B*, vol. 50, no. 23, pp. 17487–17495, 1994.

[105] C. Struzzi, C. S. Praveen, M. Scardamaglia, N. I. Verbitskiy, A. V. Fedorov, M. Weinl, M. Schreck, A. Grüneis, S. Piccinin, S. Fabris, and L. Petaccia, "Controlled Thermodynamics for Tunable Electron Doping of Graphene on Ir(111)," *Physical Review B*, vol. 94, no. 8, p. 085427, 2016.

[106] C. Virojanadara, A. A. Zakharov, S. Watcharinyanon, R. Yakimova, and L. I. Johansson, "A Low-Energy Electron Microscopy and X-Ray Photo-Emission Electron Microscopy Study of Li Intercalated into Graphene on SiC(0001)," *New Journal of Physics*, vol. 12, no. 12, p. 125015, 2010.

[107] F. Bisti, G. Profeta, H. Vita, M. Donarelli, F. Perrozzi, P. M. Sheverdyaeva, P. Moras, K. Horn, and L. Ottaviano, "Electronic and Geometric Structure of Graphene/SiC(0001) Decoupled by Lithium Intercalation," *Physical Review B*, vol. 91, no. 24, p. 245411, 2015.

[108] N. M. Caffrey, L. I. Johansson, C. Xia, R. Armiento, I. A. Abrikosov, and C. Jacobi, "Structural and Electronic Properties of Li-Intercalated Graphene on SiC(0001)," *Physical Review B*, vol. 93, no. 19, p. 195421, 2016.

[109] S. Fiori, Y. Murata, S. Veronesi, A. Rossi, C. Coletti, and S. Heun, "Li-Intercalated Graphene on SiC(0001): An STM Study," *Physical Review B*, vol. 96, no. 12, p. 125429, 2017.

[110] M. Lagues, D. Marchand, C. Fretigny, and A. Legrand, "Valence Band of Graphite Intercalation Compounds from Auger Spectroscopy," *Solid State Communications*, vol. 49, no. 8, pp. 739–742, 1984.

[111] N. J. Wu and A. Ignatiev, "Potassium Absorption into the Graphite (0001) Surface: Intercalation," *Physical Review B*, vol. 28, no. 12, pp. 7288–7293, 1983.

[112] J. R. Rumble, ed., *CRC Handbook of Chemistry and Physics*. Boca Raton, FL: CRC Press/Taylor & Francis, 98 ed., 2017.

[113] N. Bartlett and B. W. McQuillan, "Graphite Chemistry," in *Intercalation Chemistry*, Academic Press, 1982.

[114] F. J. Salzano and S. Aronson, "On the Bonding Energy in Cesium-Graphite Compounds," *The Journal of Chemical Physics*, vol. 44, no. 11, pp. 4320–4326, 1966.

[115] F. J. Salzano and S. Aronson, "Thermodynamic Properties of Rubidium-Graphite Lamellar Compounds," *The Journal of Chemical Physics*, vol. 45, no. 12, pp. 4551–4555, 1966.

[116] L. Mandeltort and J. T. Yates, "Rapid Atomic Li Surface Diffusion and Intercalation on Graphite: A Surface Science Study," *The Journal of Physical Chemistry C*, vol. 116, no. 47, pp. 24962–24967, 2012.

[117] Y. Liu, B. V. Merinov, and W. A. Goddard, "Origin of Low Sodium Capacity in Graphite and Generally Weak Substrate Binding of Na and Mg Among Alkali and

Alkaline Earth Metals," *Proceedings of the National Academy of Sciences*, vol. 113, no. 14, pp. 3735–3739, 2016.

[118] Y. Wen, K. He, Y. Zhu, F. Han, Y. Xu, I. Matsuda, Y. Ishii, J. Cumings, and C. Wang, "Expanded Graphite as Superior Anode for Sodium-Ion Batteries," *Nature Communications*, vol. 5, 2014.

[119] C. Busse, P. Lazić, R. Djemour, J. Coraux, T. Gerber, N. Atodiresei, V. Caciuc, R. Brako, A. T. N'Diaye, S. Blügel, J. Zegenhagen, and T. Michely, "Graphene on Ir(111): Physisorption with Chemical Modulation," *Physical Review Letters*, vol. 107, no. 3, p. 036101, 2011.

[120] P. Pervan and P. Lazić, "Adsorbed or Intercalated: Na on Graphene/Ir(111)," *Physical Review Materials*, vol. 1, no. 4, p. 044202, 2017.

[121] N. R. Gall, E. V. Rut'kov, and A. Y. Tontegode, "Two Dimensional Graphite Films on Metals and Their Intercalation," *International Journal of Modern Physics B*, vol. 11, no. 16, pp. 1865–1911, 1997.

[122] T. Langer, D. F. Förster, C. Busse, T. Michely, H. Pfnür, and C. Tegenkamp, "Sheet Plasmons in Modulated Graphene on Ir(111)," *New Journal of Physics*, vol. 13, no. 5, p. 053006, 2011.

[123] M. Papagno, S. Rusponi, P. M. Sheverdyaeva, S. Vlaic, M. Etzkorn, D. Pacilé, P. Moras, C. Carbone, and H. Brune, "Large Band Gap Opening between Graphene Dirac Cones Induced by Na Adsorption onto an Ir Superlattice," *ACS Nano*, vol. 6, no. 1, pp. 199–204, 2012.

[124] Y. S. Park, J. H. Park, H. N. Hwang, T. S. Laishram, K. S. Kim, M. H. Kang, and C. C. Hwang, "Quasi-Free-Standing Graphene Monolayer on a Ni Crystal through Spontaneous Na Intercalation," *Physical Review X*, vol. 4, no. 3, p. 031016, 2014.

[125] M. Kühne, F. Paolucci, J. Popovic, P. M. Ostrovsky, J. Maier, and J. H. Smet, "Ultrafast Lithium Diffusion in Bilayer Graphene," *Nature Nanotechnology*, vol. 12, no. 9, pp. 895–900, 2017.

[126] J. Algdal, T. Balasubramanian, M. Breitholtz, T. Kihlgren, and L. Walldén, "Thin Graphite Overlayers: Graphene and Alkali Metal Intercalation," *Surface Science*, vol. 601, pp. 1167–1175, 2007.

[127] J. Kleeman, K. Sugawara, T. Sato, and T. Takahashi, "Enhancement of Electron–Phonon Coupling in Cs-Overlayered Intercalated Bilayer Graphene," *Journal of Physics: Condensed Matter*, vol. 28, no. 20, p. 204001, 2016.

[128] C. M. Osburn and S. I. Raider, "The Effect of Mobile Sodium Ions on Field Enhancement Dielectric Breakdown in SiO_2 Films on Silicon," *Journal of The Electrochemical Society*, vol. 120, no. 10, p. 1369, 1973.

[129] G. Greeuw and J. F. Verwey, "The mobility of Na + , Li + , and K + ions in thermally grown SiO_2 films," *Journal of Applied Physics*, vol. 56, no. 8, pp. 2218–2224, 1984.

[130] K. Sugawara, K. Kanetani, T. Sato, and T. Takahashi, "Fabrication of Li-Intercalated Bilayer Graphene," *AIP Advances*, vol. 1, no. 2, 2011.

[131] D. M. Guzman, H. M. Alyahyaei, and R. A. Jishi, "Superconductivity in graphene-lithium," *2D Materials*, vol. 1, no. 2, p. 021005, 2014.

[132] T. P. Kaloni, Y. Cheng, M. Upadhyay Kahaly, and U. Schwingenschlögl, "Charge Carrier Density in Li-Intercalated Graphene," *Chemical Physics Letters*, vol. 534, pp. 29–33, 2012.

[133] E. Lee and K. A. Persson, "Li Absorption and Intercalation in Single Layer Graphene and Few Layer Graphene by First Principles," *Nano Letters*, vol. 12, no. 9, pp. 4624–4628, 2012.

[134] A. O'Hara, R. E. Kahn, Y. Y. Zhang, and S. T. Pantelides, "Defect-Mediated Leakage in Lithium Intercalated Bilayer Graphene," *AIP Advances*, vol. 7, no. 4, p. 045205, 2017.

[135] C. Xia, S. Watcharinyanon, A. Zakharov, L. Johansson, R. Yakimova, and C. Virojanadara, "Detailed Studies of Na Intercalation on Furnace-Grown Graphene on 6H-SiC(0001)," *Surface Science*, vol. 613, pp. 88–94, 2013.

[136] S. Yang, S. Li, S. Tang, W. Dong, W. Sun, D. Shen, and M. Wang, "Sodium Adsorption and Intercalation in Bilayer Graphene from Density Functional Theory Calculations," *Theoretical Chemistry Accounts*, vol. 135, no. 7, p. 164, 2016.

[137] S. Yang, S. Li, S. Tang, D. Shen, W. Dong, and W. Sun, "Adsorption, Intercalation and Diffusion of Na on Defective Bilayer Graphene: a Computational Study," *Surface Science*, vol. 658, pp. 31–37, 2017.

[138] T. P. Kaloni, M. Upadhyay Kahaly, Y. C. Cheng, and U. Schwingenschlögl, "K-Intercalated Carbon Systems: Effects of Dimensionality and Substrate," *Europhysics Letters*, vol. 98, no. 6, p. 67003, 2012.

[139] T. Kaneko and R. Saito, "First-Principles Study on Interlayer State in Alkali and Alkaline Earth Metal Atoms Intercalated Bilayer Graphene," *Surface Science*, vol. 665, pp. 1–9, 2017.

[140] G. Srinivas and X. G. Zheng, "Graphene-Based Materials: Synthesis and Gas Sorption, Storage and Separation," *Progress in Materials Science*, vol. 69, no. Supplement C, pp. 1 – 60, 2015.

[141] A. A. S. Nair, R. Sundara, and N. Anitha, "Hydrogen Storage Performance of Palladium Nanoparticles Decorated Graphitic Carbon Nitride," *International Journal of Hydrogen Energy*, vol. 40, no. 8, pp. 3259 – 3267, 2015.

[142] H. G. Shiraz and R. Seyfollahi, "Hybrid System for Potential Room Temperature Hydrogen Storage," *Vacuum*, vol. 131, no. Supplement C, pp. 115 – 119, 2016.

[143] E. Yoo, T. Okata, T. Akita, M. Kohyama, J. Nakamura, and I. Honma, "Enhanced Electrocatalytic Activity of Pt Subnanoclusters on Graphene Nanosheet Surface," *Nano Letters*, vol. 9, no. 6, pp. 2255–2259, 2009.

[144] Y. Li, X. Fan, J. Qi, J. Ji, S. Wang, G. Zhang, and F. Zhang, "Palladium Nanoparticle-Graphene Hybrids as Active Catalysts for the Suzuki Reaction," *Nano Research*, vol. 3, no. 6, pp. 429–437, 2010.

[145] M. H. Seo, S. M. Choi, H. J. Kim, and W. B. Kim, "The Graphene-Supported Pd and Pt Catalysts for Highly Active Oxygen Reduction Reaction in an Alkaline Condition," *Electrochemistry Communications*, vol. 13, no. 2, pp. 182 – 185, 2011.

[146] S. Navalon, A. Dhakshinamoorthy, M. Alvaro, and H. Garcia, "Metal Nanoparticles Supported on Two-Dimensional Graphenes as Heterogeneous Catalysts," *Coordination Chemistry Reviews*, vol. 312, no. Supplement C, pp. 99–148, 2016.

[147] M. G. Chung, D.-H. Kim, D. K. Seo, T. Kim, H. U. Im, H. M. Lee, J.-B. Yoo, S.-H. Hong, T. J. Kang, and Y. H. Kim, "Flexible Hydrogen Sensors Using Graphene with Palladium Nanoparticle Decoration," *Sensors and Actuators B: Chemical*, vol. 169, pp. 387–392, 2012.

[148] B. Cho, J. Yoon, M. G. Hahm, D.-H. Kim, A. R. Kim, Y. H. Kahng, S.-W. Park, Y.-J. Lee, S.-G. Park, J.-D. Kwon, C. S. Kim, M. Song, Y. Jeong, K.-S. Nam, and H. C. Ko, "Graphene-Based Gas Sensor: Metal Decoration Effect and Application to a Flexible Device," *J. Mater. Chem. C*, vol. 2, no. 27, pp. 5280–5285, 2014.

[149] D.-T. Phan and G.-S. Chung, "Characteristics of Resistivity-Type Hydrogen Sensing Based on Palladium-Graphene Nanocomposites," *International Journal of Hydrogen Energy*, vol. 39, no. 1, pp. 620–629, 2014.

[150] J. Hong, S. Lee, J. Seo, S. Pyo, J. Kim, and T. Lee, "A Highly Sensitive Hydrogen Sensor with Gas Selectivity Using a PMMA Membrane-Coated Pd Nanoparticle/Single-Layer Graphene Hybrid," *ACS Applied Materials & Interfaces*, vol. 7, no. 6, pp. 3554–3561, 2015.

[151] D. Appy, H. Lei, C.-Z. Wang, M. C. Tringides, D.-J. Liu, J. W. Evans, and P. A. Thiel, "Transition Metals on the (0001) Surface of Graphite: Fundamental Aspects of Adsorption, Diffusion, and Morphology," *Progress in Surface Science*, vol. 89, no. 3, pp. 219 – 238, 2014.

[152] P. Brault and G. Moebs, "Molecular Dynamics Simulations of Palladium Cluster Growth on Flat and Rough Graphite Surfaces," *European Physical Journal Applied Physics*, vol. 28, no. 1, pp. 43–50, 2004.

[153] L. Z. Zhang, S. X. Du, J. T. Sun, L. Huang, L. Meng, W. Y. Xu, L. D. Pan, Y. Pan, Y. L. Wang, W. A. Hofer, and H.-J. Gao, "Growth Mechanism of Metal Clusters on a Graphene/Ru(0001) Template," *Advanced Materials Interfaces*, vol. 1, no. 3, p. 1300104, 2014.

[154] R. Zan, U. Bangert, Q. Ramasse, and K. S. Novoselov, "Evolution of Gold Nanostructures on Graphene," *Small*, vol. 7, no. 20, pp. 2868–2872, 2011.

[155] D. W. Boukhvalov and M. I. Katsnelson, "Destruction of Graphene by Metal Adatoms," *Applied Physics Letters*, vol. 95, no. 2, p. 023109, 2009.

[156] S. M. Binz, M. Hupalo, X. Liu, C. Z. Wang, W.-C. Lu, P. A. Thiel, K. M. Ho, E. H. Conrad, and M. C. Tringides, "High Island Densities and Long Range Repulsive Interactions: Fe on Epitaxial Graphene," *Physical Review Letters*, vol. 109, no. 2, p. 026103, 2012.

[157] S. W. Poon, A. T. S. Wee, and E. S. Tok, "Anomalous Scaling Behaviour of Cobalt Cluster Size Distributions on Graphite, Epitaxial Graphene and Carbon-Rich ($6\sqrt{3}\times 6\sqrt{3}$)R30°," *Surface Science*, vol. 606, no. 21-22, pp. 1586–1593, 2012.

[158] A. T. N'Diaye, T. Gerber, C. Busse, J. Mysliveček, J. Coraux, and T. Michely, "A Versatile Fabrication Method for Cluster Superlattices," *New Journal of Physics*, vol. 11, no. 10, p. 103045, 2009.

[159] D. Franz, S. Runte, C. Busse, S. Schumacher, T. Gerber, T. Michely, M. Mantilla, V. Kilic, J. Zegenhagen, and A. Stierle, "Atomic Structure and Crystalline Order of Graphene-Supported Ir Nanoparticle Lattices," *Physical Review Letters*, vol. 110, p. 065503, 2013.

[160] M. Sicot, S. Bouvron, O. Zander, U. Rüdiger, Y. S. Dedkov, and M. Fonin, "Nucleation and Growth of Nickel Nanoclusters on Graphene Moiré on Rh(111)," *Applied Physics Letters*, vol. 96, no. 9, p. 093115, 2010.

[161] K. Gotterbarm, C. Steiner, C. Bronnbauer, U. Bauer, H.-P. Steinrück, S. Maier, and C. Papp, "Graphene-Templated Growth of Pd Nanoclusters," *The Journal of Physical Chemistry C*, vol. 118, no. 29, pp. 15934–15939, 2014.

[162] Z. Zhou, F. Gao, and D. W. Goodman, "Deposition of Metal Clusters on Single-Layer Graphene/Ru(0001): Factors that Govern Cluster Growth," *Surface Science*, vol. 604, no. 13-14, pp. L31–L38, 2010.

[163] Y. Pan, M. Gao, L. Huang, F. Liu, and H.-J. Gao, "Directed Self-Assembly of Monodispersed Platinum Nanoclusters on Graphene Moiré Template," *Applied Physics Letters*, vol. 95, no. 9, p. 093106, 2009.

[164] Q. Liao, H. J. Zhang, K. Wu, H. Y. Li, S. N. Bao, and P. He, "Nucleation and Growth of Monodispersed Cobalt Nanoclusters on Graphene Moiré on Ru(0001)," *Nanotechnology*, vol. 22, no. 12, p. 125303, 2011.

[165] F. Ruffino and F. Giannazzo, "A Review on Metal Nanoparticles Nucleation and Growth on/in Graphene," *Crystals*, vol. 7, no. 7, p. 219, 2017.

[166] M. Sicot, P. Leicht, A. Zusan, S. Bouvron, O. Zander, M. Weser, Y. S. Dedkov, K. Horn, and M. Fonin, "Size-Selected Epitaxial Nanoislands Underneath Graphene Moiré on Rh(111)," *ACS Nano*, vol. 6, no. 1, pp. 151–158, 2012.

[167] E. Soy, N. P. Guisinger, and M. Trenary, "Growth of Pd Nanoclusters on Single-Layer Graphene on Cu(111)," *The Journal of Physical Chemistry B*, p. acs.jpcb.7b05064, 2017.

[168] H. Zhou, F. Yu, H. Yang, C. Qiu, M. Chen, L. Hu, Y. Guo, H. Yang, C. Gu, and L. Sun, "Layer-Dependent Morphologies and Charge Transfer of Pd on n-Layer Graphenes," *Chem. Commun.*, vol. 47, pp. 9408–9410, 2011.

[169] H. Zhou, C. Qiu, Z. Liu, H. Yang, L. Hu, J. Liu, H. Yang, C. Gu, and L. Sun, "Thickness-Dependent Morphologies of Gold on N-Layer Graphenes," *Journal of the American Chemical Society*, vol. 132, no. 3, pp. 944–946, 2010.

[170] H.-Q. Zhou, F. Yu, H.-C. Yang, M.-J. Chen, G. Wang, and L.-F. Sun, "High-Throughput Thickness Determination of n-Layer Graphenes via Gold Deposition," *Chemical Physics Letters*, vol. 518, no. Supplement C, pp. 76 – 80, 2011.

[171] H. Zhou, C. Qiu, F. Yu, H. Yang, M. Chen, L. Hu, and L. Sun, "Thickness-Dependent Morphologies and Surface-Enhanced Raman Scattering of Ag Deposited on n-Layer Graphenes," *The Journal of Physical Chemistry C*, vol. 115, no. 23, pp. 11348–11354, 2011.

[172] C. Qiu, H. Zhou, B. Cao, L. Sun, and T. Yu, "Raman Spectroscopy of Morphology-Controlled Deposition of Au on Graphene," *Carbon*, vol. 59, no. Supplement C, pp. 487 – 494, 2013.

[173] T. P. Hardcastle, C. R. Seabourne, R. Zan, R. M. D. Brydson, U. Bangert, Q. M. Ramasse, K. S. Novoselov, and A. J. Scott, "Mobile Metal Adatoms on Single Layer, Bilayer, and Trilayer Graphene: An ab initio DFT Study with van der Waals Corrections Correlated with Electron Microscopy Data," *Physical Review B*, vol. 87, p. 195430, 2013.

[174] I. Kojima, A. K. Srivastava, and M. Kurahashi, "Scanning Tunneling Microscopic Study of Structures of Deposited Palladium on Graphite," *Japanese Journal of Applied Physics*, vol. 30, no. 8R, p. 1852, 1991.

[175] Y. Murakami, K. Naoi, K. Yahikozawa, and Y. Takasu, "High-Resolution Images of Pd Particles Supported on Highly Oriented Pyrolytic Graphite and Glassy Carbon," *Journal of The Electrochemical Society*, vol. 141, no. 9, p. 2511, 1994.

[176] C. M. Whelan and C. J. Barnes, "An STM Study of Structural Transitions During the Nucleation and Growth of Pd and Cu Cluster Catalysts on HOPG," *Applied Surface Science*, vol. 119, no. 3, pp. 288 – 300, 1997.

[177] M. Bovet, E. Boschung, J. Hayoz, T. Pillo, G. Dietler, and P. Aebi, "Geometrical and Electronic Structure of Pd Clusters on Graphite," *Surface Science*, vol. 473, pp. 17–24, 2001.

[178] I. Lopez-Salido, D. C. Lim, and Y. D. Kim, "Ag Nanoparticles on Highly Ordered Pyrolytic Graphite (HOPG) Surfaces Studied Using STM and XPS," *Surface Science*, vol. 588, no. 1, pp. 6 – 18, 2005.

[179] L. Bardotti, F. Tournus, P. Mélinon, M. Pellarin, and M. Broyer, "Mass-Selected Clusters Deposited on Graphite: Spontaneous Organization Controlled by Cluster Surface Reaction," *Physical Review B*, vol. 83, p. 035425, 2011.

[180] J. R. Arthur and A. Y. Cho, "Adsorption and Desorption Kinetics of Cu and Au on (0001) Graphite," *Surface Science*, vol. 36, no. 2, pp. 641 – 660, 1973.

[181] R. Anton and I. Schneidereit, "In Situ TEM Investigations of Dendritic Growth of Au Particles on HOPG," *Physical Review B*, vol. 58, no. 20, pp. 13874–13881, 1998.

[182] A. R. Howells, L. Hung, G. S. Chottiner, and D. A. Scherson, "Effects of substrate defect density and annealing temperature on the nature of pt clusters vapor deposited on the basal plane of highly oriented pyrolytic graphite," *Solid State Ionics*, vol. 150, no. 1, pp. 53 – 62, 2002. Ringberg Workshop 2000 Special Issue.

[183] W. F. Egelhoff and G. G. Tibbetts, "Growth of Copper, Nickel, and Palladium Films on Graphite and Amorphous Carbon," *Physical Review B*, vol. 19, pp. 5028–5035, 1979.

[184] I. N. Kholmanov, L. Gavioli, M. Fanetti, M. Casella, C. Cepek, C. Mattevi, and M. Sancrotti, "Effect of Substrate Surface Defects on the Morphology of Fe Film Deposited on Graphite," *Surface Science*, vol. 601, no. 1, pp. 188 – 192, 2007.

[185] Z. Yuan, M. Hanf, R. Stephan, F. Dulot, E. Denys, A. Florentin, W. Harbich, and P. Wetzel, "Growth of Palladium Nanoparticles on Nanostructured Highly Ordered Pyrolytic Graphite," *Surface and Interface Analysis*, vol. 47, no. 1, pp. 82–86, 2015.

[186] G. M. Francis, I. M. Goldby, L. Kuipers, B. von Issendorff, and R. E. Palmer, "Deposition and Growth of Noble Metal Clusters on Graphite," *J. Chem. Soc., Dalton Trans.*, pp. 665–671, 1996.

[187] A. Piednoir, E. Perrot, S. Granjeaud, A. Humbert, C. Chapon, and C. Henry, "Atomic Resolution on Small Three-Dimensional Metal Clusters by STM," *Surface Science*, vol. 391, no. 1-3, pp. 19–26, 1997.

[188] L. Huang, Y. Pan, L. Pan, M. Gao, W. Xu, Y. Que, H. Zhou, Y. Wang, S. Du, and H.-J. Gao, "Intercalation of Metal Islands and Films at the Interface of Epitaxially Grown Graphene and Ru(0001) Surfaces," *Applied Physics Letters*, vol. 99, no. 16, p. 163107, 2011.

[189] K. Yagyu, K. Takahashi, H. Tochihara, H. Tomokage, and T. Suzuki, "Neutralization of an Epitaxial Graphene Grown on a SiC(0001) by Means of Palladium Intercalation," *Applied Physics Letters*, vol. 110, no. 13, p. 131602, 2017.

[190] W. P. Griffith, S. D. Robinson, and K. Swars, *Pd Palladium: Palladium Compounds*. Gmelin Handbook of Inorganic and Organometallic Chemistry - 8th edition, Springer Berlin Heidelberg, 2013.

[191] J. Walter and H. Shioyama, "Quasi Two-Dimensional Palladium Nanoparticles Encapsulated Into Graphite," *Physics Letters A*, vol. 254, no. 1, pp. 65 – 71, 1999.

[192] M. Knoll and E. Ruska, "Beitrag zur geometrischen Elektronenoptik. II," *Annalen der Physik*, vol. 404, no. 6, pp. 641–661, 1932.

[193] D. Gabor, "A New Microscopic Principle," *Nature*, vol. 161, pp. 777–778, 1948.

[194] D. Gabor, "Microscopy by Reconstructed Wave-Fronts," *Proceedings of the Royal Society A*, vol. 197, no. 1051, pp. 454–487, 1949.

[195] H. J. Kreuzer, K. Nakamura, and A. Wierzbicki, "Theory of the Point Source Electron Microscope," *Ultramicroscopy*, vol. 45, pp. 381–403, 1992.

[196] T. Latychevskaia and H.-W. Fink, "Practical Algorithms for Simulation and Reconstruction of Digital In-Line Holograms," *Applied Optics*, vol. 54, no. 9, pp. 2424–2434, 2015.

[197] H.-W. Fink, H. Schmid, E. Ermantraut, and T. Schulz, "Electron Holography of Individual DNA Molecules," *Journal of the Optical Society of America A*, vol. 14, no. 9, pp. 2168–2172, 1997.

[198] A. Eisele, B. Völkel, M. Grunze, and A. Gölzhäuser, "Nanometer Resolution Holography with the Low-Energy Electron Point Source Microscope," in *Zeitschrift fur Physikalische Chemie*, vol. 222, pp. 779–787, 2008.

[199] M. Germann, T. Latychevskaia, C. Escher, and H.-W. Fink, "Pulsed Electron Holography," *Applied Physics Letters*, vol. 102, no. 20, p. 203115, 2013.

[200] H.-W. Fink, "Mono-Atomic Tips for Scanning Tunneling Microscopy," *IBM Journal of Research and Development*, vol. 30, no. 5, pp. 460–465, 1986.

[201] H.-W. Fink, "Point Source for Ions and Electrons," *Physica Scripta*, vol. 38, no. 2, p. 260, 1988.

[202] H.-W. Fink, W. Stocker, and H. Schmid, "Coherent Point-Source Electron-Beams," *Journal of Vacuum Science & Technology B*, vol. 8, no. 6, pp. 1323–1324, 1990.

[203] R. Strayer, W. Mackie, and L. Swanson, "Work Function Measurements by the Field Emission Retarding Potential Method," *Surface Science*, vol. 34, no. 2, pp. 225–248, 1973.

[204] R. Gomer, *Field Emissions and Field Ionization.* AVS Classics in Vacuum Science and Technology, American Inst. of Physics, 1992.

[205] R. H. Fowler and L. Nordheim, "Electron Emission in Intense Electric Fields," *Proceedings of the Royal Society A*, vol. 119, pp. 173–181, may 1928.

[206] C. J. Edgcombe and U. Valdre, "Microscopy and Computational Modelling to Elucidate the Enhancement Factor for Field Electron Emitters," *Journal of Microscopy*, vol. 203, pp. 188–194, aug 2001.

[207] H. U. Müller, B. Völkel, M. Hofmann, C. Wöll, and M. Grunze, "Emission Properties of Electron Point Sources," *Ultramicroscopy*, vol. 50, no. 1, pp. 57–64, 1993.

[208] R. Gomer, "Field emission, field ionization, and field desorption," *Surface Science*, vol. 299-300, pp. 129–152, jan 1994.

[209] V. T. Binh, V. Semet, and N. Garcia, "Nanometric Observations at Low Energy by Fresnel Projection Microscopy: Carbon and Polymer Fibres," *Ultramicroscopy*, vol. 58, no. 3-4, pp. 307–317, 1995.

[210] C.-C. Chang, H.-S. Kuo, I.-S. Hwang, and T. T. Tsong, "A Fully Coherent Electron Beam from a Noble-Metal Covered W(111) Single-Atom Emitter," *Nanotechnology*, vol. 20, no. 11, p. 115401, 2009.

[211] A. Beyer and A. Gölzhäuser, "Low Energy Electron Point Source Microscopy: Beyond Imaging," *Journal of Physics: Condensed Matter*, vol. 22, no. 34, p. 343001, 2010.

[212] L. W. Swanson and L. C. Crouser, "Total-Energy Distribution of Field-Emitted Electrons and Single-Plane Work Functions for Tungsten," *Physical Review*, vol. 163, no. 3, pp. 622–641, 1967.

[213] M. R. Scheinfein, W. Qian, and J. C. H. Spence, "Aberrations of Emission Cathodes: Nanometer Diameter Field-Emission Electron Sources," *Journal of Applied Physics*, vol. 73, no. 5, pp. 2057–2068, 1993.

[214] R. Morin, "Point Source Physics: Application to Electron Projection Microscopy and Holography," *Microscopy Microanalysis Microstructures*, vol. 5, no. 4-6, pp. 501–508, 1994.

[215] R. Morin and A. Degiovanni, "Interferometry with Low-Energy Electrons," in *IVMC 94 - 7th International Vacuum Microelectronics Conference*, pp. 11–12, Société Française du Vide, 19 rue du Renard, 75004 Paris, France, 1994.

[216] J. C. H. Spence, W. Qian, and M. P. Silverman, "Electron Source Brightness and Degeneracy from Fresnel Fringes in Field Emission Point Projection Microscopy," *Journal of Vacuum Science & Technology A*, vol. 12, no. 2, pp. 542–547, 1994.

[217] W. Qian, M. R. Scheinfein, and J. C. H. Spence, "Brightness Measurements of Nanometer-Sized Field-Emission-Electron Sources," *Journal of Applied Physics*, vol. 73, no. 11, pp. 7041–7045, 1993.

[218] T. Latychevskaia, F. Wicki, C. Escher, and H.-W. Fink, "Imaging the Potential Distribution of Individual Charged Impurities on Graphene by Low-Energy Electron Holography," *Ultramicroscopy*, vol. 182, pp. 276–282, 2017.

[219] T. Latychevskaia, J.-N. Longchamp, and H.-W. Fink, "When Holography Meets Coherent Diffraction Imaging," *Optics Express*, vol. 20, no. 27, p. 28871, 2012.

[220] I.-S. Hwang, C.-C. Chang, C.-H. Lu, S.-C. Liu, Y.-C. Chang, T.-K. Lee, H.-T. Jeng, H.-S. Kuo, C.-Y. Lin, C.-S. Chang, and T. T. Tsong, "Investigation of single-walled carbon nanotubes with a low-energy electron point projection microscope," *New Journal of Physics*, vol. 15, no. 4, p. 043015, 2013.

[221] M. Prigent and P. Morin, "Charge Effect in Point Projection Images of Carbon Fibres," *Journal of Microscopy*, vol. 199, no. 3, pp. 197–207, 2000.

[222] G. Möllenstedt and H. Düker, "Beobachtungen und messungen an biprisma-interferenzen mit elektronenwellen," *Zeitschrift für Physik*, vol. 145, no. 3, pp. 377–397, 1956.

[223] T. Latychevskaia, J.-N. Longchamp, C. Escher, and H.-W. Fink, "On Artefact-Free Reconstruction of Low-Energy (30–250eV) Electron Holograms," *Ultramicroscopy*, vol. 145, pp. 22 – 27, 2014.

[224] G. Hassink, R. Wanke, I. Rastegar, W. Braun, C. Stephanos, P. Herlinger, J. H. Smet, and J. Mannhart, "Transparency of Graphene for Low-Energy Electrons Measured in a Vacuum-Triode Setup," *APL Materials*, vol. 3, no. 7, p. 076106, 2015.

[225] C. J. Powell and A. Jablonski, *NIST Electron Effective-Attenuation-Length Database, Version 1.3*. National Institute of Standards and Technology, Gaithersburg, MD, 2011.

[226] J.-A. Yan, J. A. Driscoll, B. K. Wyatt, K. Varga, and S. T. Pantelides, "Time-Domain Simulation of Electron Diffraction in Crystals," *Physical Review B*, vol. 84, p. 224117, 2011.

[227] J. Kraus, R. Reichelt, S. Gunther, L. Gregoratti, M. Amati, M. Kiskinova, A. Yulaev, I. Vlassiouk, and A. Kolmakov, "Photoelectron Spectroscopy of Wet and Gaseous Samples Through Graphene Membranes," *Nanoscale*, vol. 6, pp. 14394–14403, 2014.

[228] L. Frank, E. Mikmeková, I. Müllerová, and M. Lejeune, "Counting Graphene Layers with Very Slow Electrons," *Applied Physics Letters*, vol. 106, no. 1, p. 013117, 2015.

[229] H. Miyauchi, Y. Ueda, Y. Suzuki, and K. Watanabe, "Electron Transmission Through Bilayer Graphene: A Time-Dependent First-Principles Study," *Physical Review B*, vol. 95, p. 125425, 2017.

[230] Y. Kuk and P. J. Silverman, "Scanning Tunneling Microscope Instrumentation," *Review of Scientific Instruments*, vol. 60, no. 2, pp. 165–180, 1989.

[231] A. P. Janssen and J. P. Jones, "The Sharpening of Field Emitter Tips by Ion Sputtering," *Journal of Physics D*, vol. 4, no. 1, p. 118, 1971.

[232] F. Wicki, *Four Novel Electron Point Source Applications*. PhD thesis, University of Zurich, September 2016.

[233] D. Coffin, "dcraw(version 9.11)," 2013.

[234] SAES Getters S.p.a., "https://www.saesgetters.com/."

[235] P. Della Porta, C. Emil, and S. J. Hellier, "Alkali Metal Generation and Gas Evolution from Alkali Metal Dispensers," in *IEEE Conference on Tube Techniques, NY*, 1968.

[236] D. R. Scherer, D. B. Fenner, and J. M. Hensley, "Characterization of Alkali Metal Dispensers and Non-Evaporable Getter Pumps in Ultrahigh Vacuum Systems for Cold Atomic Sensors," *Journal of Vacuum Science & Technology A*, vol. 30, no. 6, p. 061602, 2012.

[237] R. Banerjee, *Absolute Coverage Measurements of Ultrathin Alkali–Metal Films on Reconstructed Silicon*. PhD thesis, Drexel University, Philadelphia, 2001.

[238] P. A. Pianetta, "In situ processing by gas or alkali metal dosing and by cleavage," in *Specimen Handling, Preparation, and Treatments in Surface Characterization*, pp. 173–208, Springer, 2002.

[239] M. Succi, R. Canino, and B. Ferrario, "Atomic Absorption Evaporation Flow Rate Measurements of Alkali Metal Dispensers," *Vacuum*, vol. 35, no. 12, pp. 579 – 582, 1985.

[240] J.-N. Longchamp, C. Escher, and H.-W. Fink, "Ultraclean Freestanding Graphene by Platinum-Metal Catalysis," *Journal of Vacuum Science & Technology B*, vol. 31, no. 2, p. 020605, 2013.

[241] S. P. Surwade, Z. Li, and H. Liu, "Thermal Oxidation and Unwrinkling of Chemical Vapor Deposition-Grown Graphene," *The Journal of Physical Chemistry C*, vol. 116, no. 38, pp. 20600–20606, 2012.

[242] L. Liu, S. Ryu, M. R. Tomasik, E. Stolyarova, N. Jung, M. S. Hybertsen, M. L. Steigerwald, L. E. Brus, and G. W. Flynn, "Graphene Oxidation: Thickness-Dependent Etching and Strong Chemical Doping," *Nano Letters*, vol. 8, no. 7, pp. 1965–1970, 2008.

[243] H. Y. Nan, Z. H. Ni, J. Wang, Z. Zafar, Z. X. Shi, and Y. Y. Wang, "The Thermal Stability of Graphene in Air Investigated by Raman Spectroscopy," *Journal of Raman Spectroscopy*, vol. 44, no. 7, pp. 1018–1021, 2013.

[244] H. J. Yan, B. Xu, S. Q. Shi, and C. Y. Ouyang, "First-Principles Study of the Oxygen Adsorption and Dissociation on Graphene and Nitrogen Doped Graphene for Li-Air Batteries," *Journal of Applied Physics*, vol. 112, no. 10, p. 104316, 2012.

[245] J. Zhao, M. A. Brubaker, S. Benlekbir, and J. L. Rubinstein, "Description and Comparison of Algorithms for Correcting Anisotropic Magnification in Cryo-EM Images," *Journal of Structural Biology*, vol. 192, no. 2, pp. 209–215, 2015.

[246] G. Yu, K. Li, Y. Liu, Z. Chen, Z. Wang, R. Yan, T. Klose, L. Tang, and W. Jiang, "An Algorithm for Estimation and Correction of Anisotropic Magnification Distortion of Cryo-EM Images Without Need of Pre-Calibration," *Journal of Structural Biology*, vol. 195, no. 2, pp. 207–215, 2016.

[247] M. Büttner, P. Choudhury, J. Karl Johnson, and J. T. Yates, "Vacancy Clusters as Entry Ports for Cesium Intercalation in Graphite," *Carbon*, vol. 49, pp. 3937–3952, 2011.

[248] Y. Liu, V. I. Artyukhov, M. Liu, A. R. Harutyunyan, and B. I. Yakobson, "Feasibility of Lithium Storage on Graphene and Its Derivatives," *The Journal of Physical Chemistry Letters*, vol. 4, no. 10, pp. 1737–1742, 2013.

[249] J. A. Venables, G. D. T. Spiller, and M. Hanbucken, "Nucleation and Growth of Thin Films," *Reports on Progress in Physics*, vol. 47, pp. 399–459, apr 1984.

[250] S. Tanuma, C. J. Powell, and D. R. Penn, "Calculations of Electron Inelastic Mean Free Paths (IMFPS). IV. Evaluation of calculated IMFPs and of the predictive IMFP formula TPP-2 for electron energies between 50 and 2000 eV," *Surface and Interface Analysis*, vol. 20, no. 1, pp. 77–89, 1993.

[251] V. C. Aguilera-Navarro, G. A. Estevez, and W. Solano Torres, "Pade Approximants And The Potential Of A Point Charge Between Charged Infinite Capacitor Plates," *Revista Colombiana de Fisica*, no. 20, pp. 89–98, 1988.